

Some pages of this thesis may have been removed for copyright restrictions.

If you have discovered material in Aston Research Explorer which is unlawful e.g. breaches copyright, (either yours or that of a third party) or any other law, including but not limited to those relating to patent, trademark, confidentiality, data protection, obscenity, defamation, libel, then please read our [Takedown policy](#) and contact the service immediately (openaccess@aston.ac.uk)

**SYNTHESIS AND CHARACTERISATION OF
POLYACRYLONITRILE AND ITS DERIVED
CARBON MATERIALS**

JIANGLING LI

Doctor of Philosophy

Aston University

January 2015

This copy of the thesis has been supplied on condition that anyone who consults it is understood to recognise that its copyright rests with its author and that no quotation from the thesis and no information derived from it may be published without proper acknowledgement.

Summary

Carbon is a versatile material which is composed of different allotropes, and also come in with different structures. Carbon nanofibres (CNFs) is one dimensional carbon nanomaterials, which have exhibited superior mechanical properties, great specific area, good electrical conductivity, good biocompatibility, and ease of modification. In addition to the lower cost associated to compare with carbon nanotubes (CNTs), CNFs have been attracted in numerous applications, such as reinforcement materials, filtrations, Li-ion battery, supercapacitor as well as tissue engineering, just to list a few. Therefore, it is a great deal to understand the relationship between the fabrication conditions and the characteristics of the resulted CNFs.

In this project, electrospun PAN NFs were used as precursor material to fabricate carbon nanofibres. In order to produce CNFs with good morphology, the processing parameters of PAN nanofibres by electrospinning was optimized toward to the morphology at solution concentration of 12 wt%. The optimized processing parameters at given concentration were 16 kV, 14 cm and 1.5 mL/h, which led to the formation of PAN NFs with average fibre diameter of approximately 260 nm. Along with the effect of processing parameter study, the effect of concentration on the morphology was also carried out at optimized processing parameters. It was found that by increasing concentration of PAN solution from 2 to 16%, the resulted PAN transformed from beads only, to beaded fibres and finally to smooth fibres. With further increasing concentration the morphology of smooth fibres remain with increase in the fibre diameter.

Electrospun PAN NFs with average fibre of 306 nm was selected to be converted into CNFs by using standard heating procedures, stabilisation in air at 280 °C and carbonization in N₂. The effect of carbonization temperature ranging from 500 to 1000 °C was investigated, by using SEM, FTIR, Raman, and Impedance spectroscopy. With increasing carbonization temperature from 500 to 1000 °C, the diameter of NFs was decreased from 260 to 187, associated with loss of almost all functional groups of NFs. It was indicated by Raman results, that the graphitic crystallite size was increased from 2.62 to 5.24 nm, and the activation energy obtained for this growth was 7570 J/mol. Furthermore, impedance results (i.e. Cole-Cole plot) revealed that the electrical characteristic of CNFs transitioned from being insulating to electrically conducting in nature, suggested by the different electrical circuits extracted from Cole-Cole plots with carbonization temperature from 500 to 800 °C.

The carbonization on PAN NFs with diameter of ~431nm was carried out by using novel route, microwave plasma enhance chemical vapour deposition (MPECVD) process. To compare with carbonized PAN NFs by using conventional route, MPECVD was not only able to facilitate carbonization process, but more interestingly can form carbon nanowalls (CNWs) grown on the surfaces of carbonized PAN NFs. Suggested by the unique morphology, the potential applications for the resulted carbon fibrous hybrid materials are supercapacitor electrode material, filtrations, and etc., The method developed in this project required one step less, compared with other literature. Therefore, using MPECVD on stabilised PAN NFs is proposed as economical, and straightforward approach towards mass production of carbon fibrous hybrid materials containing CNWs.

Acknowledgment

I would like to thank my supervisor, Dr. Haitao Ye, who accepted me as a PhD student and created opportunity for me to go abroad.

Sincere thanks are given my secondary supervisor, Prof. John Sullivan, who has been so kind and supportive.

Special thanks are given to the group members, Dr. Shi Su, Mr. Vojtěch Kunderát and Mr. Jamie Coathup for creating such a lovely environment to study, to care and to support during my PhD.

Sincere thanks are given to the dedicated support team, Mr. Andrew Abbot, who is knowledgeable, kind, patient and constantly providing technical assistance; Mrs. Sandra Mosely and Mrs. Helen Yard, who have been brilliant postgraduate research officers.

Special thanks to Dr. Shi Su, Dr. Graham Lee, Dr. Jianlin Li, Dr. Meiyong Liao, Dr. Mykhaylo Dubov, Dr. Baogui Shi, Dr. Chengbo Mou, and Dr. Raz Arif, who I have worked with on many interesting projects.

Sincere thanks are given to Dr. Yiquan Wu, Ms. Yan Yang, Mr. David Tseng, Mr. Yin Liu, Mr. Yiyu Li, Ms. Mui Chothirawat, Mr. Wirat Lerdprom, and Mr. Dew Yotangchai, who have been really kind and helpful to make my 3-month stay in Alfred University of US an amazing experience.

Special thanks are given to Dr. Gang Yang, Ms. Lin Chen and Mr. Bo Yan, who greatly assisted cyclic voltammetry tests and kindly shared the knowledge on the subject. Thank you also goes to Dr Jianlin Li for the kind assistance of TEM characterizations.

Big thank you is given to the future doctors from office N301, Mr. Vojtěch Kunderát, Mr. Hassan Taghizadeh, Mr. Zhongyuan Sun, Mr. Hsyn Krkz, and Mr. Mohammed Alaraimi, who have been lovely people to work with and doing a great job to create pleasant office environment.

Too many thanks want to give while there is too little space to type. Acknowledgements are given to all the people that I have known and who have ever been kind and helped me during my stay as a PhD of Aston University, for bringing me a great of cares, supports and encouragements.

Last, I would like to thank my boyfriend, Mr. Lei Zhou, who has given me so much support and understanding throughout the whole time of my PhD while he is also working to get his own PhD degree.

List of publications

1. J. Li, S. Su, L. Zhou, A. Abbot, H. Ye, Dielectric transition of polyacrylonitrile derived carbon nanofibers, *Mater. Res. Express.*, 1, 035604, 2014.
2. J. Li, S. Su, L. Zhou, V. Kundrař, A. Abbot, F. Mushtaq, D. Ouyang, D. James, D. Roberts, H. Ye, Carbon nanowalls grown by microwave plasma enhanced chemical vapor deposition during the carbonization of polyacrylonitrile fibers, *J. Appl. Phys.*, 113, 024313, 2013.
3. S. Su, J. Li, V. Kundrař, A. Abbot, H. Ye, Hydrogen-passivated detonation nanodiamond: An impedance spectroscopy study, *Diam. Relat. Mater.*, 24, 49-53, 2012.
4. S. Su, J. Li, V. Kundrař, A. Abbot, H. Ye, Hydrogen-terminated Detonation Nanodiamond: Impedance Spectroscopy and Thermal Stability Studies, *J. Appl. Phys.*, 113, 023707, 2013.
5. G. Lee, S. Su, J. Li, K. Sugden, H. Ye, Analysis of femtosecond laser surface patterning on bulk single-crystalline diamond, *J. Exp. NanoSci.*, 7, 662-672, 2012.
6. S. Su, J. Li, G. Lee, K. Sugden, D. Webb, H. Ye, Femtosecond laser-induced microstructures on diamond for microfluidic sensing device applications, *Appl. Phys. Lett.*, 102, 231913, 2013.
7. J. Li, S. Su, J. Li, H. Ye, Nanodiamond converted hollow graphene spheres as electrodes for supercapacitors, 2013 MRS proceedings, 1658, 2014.

Table of Contents

Summary.....	1
Acknowledgment.....	2
List of publications.....	3
Table of Contents	4
List of figures	7
List of tables.....	16
1 Introduction.....	18
2 Literature review.....	20
2.1 Fundamentals of Electrospinning.....	20
2.2 Effect of Parameters	24
2.2.1 Processing Parameters.....	25
2.2.2 Solution Parameters	26
2.2.3 Ambient Parameters	31
2.2.4 Needle Type	32
2.2.5 Collector.....	33
2.3 Background of Carbon Fibres	37
2.3.1 PAN Derived Carbon Fibres	38
2.3.2 Vapour-Phase-Grown Carbon Fibres	44
2.3.3 Characterisations of Carbon Nanofibres	46
2.4 Fabrication and Characterisation of carbon Nanofibre Composites	55
2.5 Aim and Objectives.....	63

3	Experimental Procedures and Characterization Techniques	65
3.1	Experimental Procedures	65
3.1.1	Electrospinning of PAN NFs	65
3.1.2	Synthesis of CNFs.....	72
3.1.3	Synthesis of CNWs-CNFs Hybrid Materials	73
3.2	Characterisation Techniques	76
3.2.1	Scanning Electron Microscopy	76
3.2.2	Transmission Electron Microscopy.....	78
3.2.3	Fourier Transform Infrared Spectroscopy.....	78
3.2.4	Raman Spectroscopy	79
3.2.5	Impedance Spectroscopy.....	80
3.2.6	Electrochemical Characterisations	82
4	Electrospinning of PAN NFs	84
4.1	Optimization of Processing Parameters at PAN Solution Concentration of 12%	84
4.1.1	Voltage	84
4.1.2	Tip-to-Collector Distance.....	93
4.1.3	Flow Rate	100
4.1.4	Long Stability and High Reproducibility	107
4.2	Solution Parameter	109
4.2.1	Solution Concentration.....	109
4.3	Summary	115
5	Fabrication and Characterisations of CNFs.....	117
5.1	SEM	117

5.2	FTIR.....	124
5.3	Raman	127
5.4	TEM.....	133
5.5	Impedance spectroscopy	135
5.6	Summary	142
6	Fabrication and Characterisations of CNWs-CNFs Hybrid Material.....	143
6.1	Morphology.....	143
6.2	Functional Groups.....	150
6.3	Chemical Structure.....	153
6.4	Electrochemical Characterisations	160
6.5	Summary	162
7	Conclusions and Future Work.....	164
7.1	Conclusions.....	164
7.2	Future Work	166
8	Reference.....	167

List of figures

Figure 2.1 SEM image of a human hair and electrospun PVA fibres [5].	20
Figure 2.2 Overview of research aspects on electrospun polymeric NFs. The pie chart is redrawn from reference [7].	21
Figure 2.3 Schematic diagram of electrospinning setup with zoom-in image of a semi-vertical angle (α) of Taylor cone.....	22
Figure 2.4 Photographs of fibre ejection trajectory of polyethylene oxide solution during electrospinning, captured with two different scales: (a) 1/250 s, and (b) 18 ns [16].	23
Figure 2.5 Schematic diagram of bending instabilities developed during the fibre ejection of electrospinning [14, 17].	24
Figure 2.6 Morphology transformation of PEO electrospun fibres induced by increasing viscosity of PEO solution [18].	28
Figure 2.7 Electrospun PAN NFs with SWNTs well aligned within the fibre matrix [33].	29
Figure 2.8 (a) SEM image of PAN nanofibres fabricated from 8 wt% PAN solution with addition of 10 wt% NDs; (b) TEM image of single NDs loaded PAN nanofibres with highlight of NDs location [32].	30
Figure 2.9 Electrospun PLLA fibres electrospun from dichloromethane solvent with a high vapour pressure [36].	31
Figure 2.10 (a) schematic diagram of coaxial electrospinning setup at needle part [40], (b) the electrospun fibres with core-shell structure produced from coaxial electrospinning [41].	33
Figure 2.11 (a) Electrospun fibres deposited on glass substrate showing NUS pattern; and (b) the NUS metal wires placed below the glass surface [43].	34

Figure 2.12 (a) Electrospinning setup used in the fabrication of aligned NFs; (b) an illustration of electric field strength between needle tip and Si collectors; and (c) optical image of aligned PVP NFs formed between a pair of Si collectors [46].	35
Figure 2.13 (a) Electrospinning setup used in the fabrication of core-shell structure; and (b) SEM image of aligned titania hollow fibres with inset of magnified single fibre [47].	36
Figure 2.14 Photograph of Edison’s early light bulb [51].	37
Figure 2.15 Manufacturing process of carbon yarns and fibres from PAN [57].	39
Figure 2.16 Proposed chemistry change of PAN during the oxidative stabilisation process [60].	41
Figure 2.17 Schematic diagram of dehydrogenation reactions during the stabilisation of PAN fibres with two different structures: (a) PAN fibres, and (b) cyclized PAN fibres [55].	41
Figure 2.18 Chemistry changes induced by the carbonization process at different carbonization temperatures [60].	42
Figure 2.19 Schematic diagram of graphite like ribbon structure formed due to dehydrogenation during the carbonization process at low carbonization temperature [67].	43
Figure 2.20 Heat treatment profile programmed for the fabrication of VGCFs at temperature of 1100 °C [68].	44
Figure 2.21 Growth mechanism proposed for the formation of VGCFs [69].	45
Figure 2.22 TEM image of CNFs fabricated by two different methods: (a)-(c) heat treatment of PAN NFs by electrospinning [71], and (d)-(f) vapour phase growth [72].	46
Figure 2.23 Evolution of various gases as function of carbonization temperature [77].	49
Figure 2.24 Simplified turbostratic microstructure for PAN derived carbon fibre [80].	50
Figure 2.25 Raman spectra of PAN derived CNFs produced from various carbonization temperatures, ranging from 700 to 2800 °C [69].	51

Figure 2.26 $d_{(002)}$ spacing comparison among the ideal graphite crystal, pitch derived carbon fibre and PAN derived carbon fibre [88].	53
Figure 2.27 Proposed skin-core structure for PAN derived carbon fibre [80].	54
Figure 2.28 TEM image of the iron-catalysed growth of MWCNTs on PAN derived CNFs. The closer view of single CNF with grown MWCNTs [89].	55
Figure 2.29 (a) SEM image of PAN derived CNFs, and (b) CNTs grown on CNFs. TEM image of the grown CNT is shown in inset [90].	56
Figure 2.30 (a) Low magnification SEM image of CNWs grown on carbon fibres by HT-CVD; (b) higher magnification SEM image of CNWs grown on carbon fibres. The broken CNWs grown on carbon fibre is inserted as inset [91].	57
Figure 2.31 (a) Schematic diagram of the distributing condition for CNT and GNWs on the CF; and (b) TEM image of CNW grown on CNT [92].	58
Figure 2.32 SEM image of a thick layer of diamond coating on the vapour grown carbon fibre deposited for 12h by using MPECVD [93].	59
Figure 2.33 TEM image of the growth of HA crystals on PAN derived CNFs by using SBF technique [94].	60
Figure 2.34 (a) Un-treated ND powders, (b) the ND powders after the hydrogen plasma treatment [95].	61
Figure 3.1 Schematic diagram of showing the preparation of PAN solution.	66
Figure 3.2 Photograph of a series of PAN solutions with various concentrations, ranging from 2% to 16%.	66
Figure 3.3 Schematic diagram of electrospinning setup used in Aston University.	67
Figure 3.4 Comparison between the electrospun PAN NFs (a) before oxidative stabilisation, and (b) after oxidative stabilisation in air.	72

Figure 3.5 Photograph of ASTeX5010 MPECVD system: (a) assembly of main components; and (b) plasma ball glows in the reactor chamber during the deposition process [99].	74
Figure 3.6 Sample preparations for carbonized PAN NFs with CNWs coating after MPECVD process.	75
Figure 3.7 Schematic diagram of SEM with basic components.	76
Figure 3.8 FTIR machine with model name of Nicolet iS5 used in Aston University.	79
Figure 3.9 Renishaw Raman spectroscopy in University of Birmingham: (a) the overview of the technique; (b) the sample stage for optical focusing with different magnifications.	79
Figure 3.10 Electrochemical system in Nanoscience group of Aston University.	80
Figure 3.11 Schematic diagram of testing cell for CNFs during the impedance measurement.	81
Figure 3.12 Schematic diagram of a standard 3 electrode configuration applied during the electrochemical measurements of CNFs and CNWs-CNFs.	82
Figure 4.1 Optical images of solution drop formed at the needle tip as a function of voltage: (a) 0-5 kV, (b) 10 kV, (c) 15 kV, (d) 20 kV, (e) 25 kV, and (f) 30 kV.	85
Figure 4.2 Quantitative plot of d_a of electrospun PAN fibre mat as a function of voltage from 10 to 30 kV. The photos of electrospun PAN fibre mats are inserted.	86
Figure 4.3 SEM images of electrospun PAN NFs deposited on Al collector at various voltages: (a) 5 kV, (b) 10 kV, (c) 15 kV, (d) 20 kV, (e) 25 kV, and (f) 30 kV.	87
Figure 4.4 Optical images of solution drop formed at the needle tip as a function of voltage: (a) 16kV, (b) 17 kV, (c) 18 kV, and (d) 19 kV.	88
Figure 4.5 Quantitative plot of d_a of electrospun fibre mat as a function of voltage of 16-19 kV. The photos of electrospun PAN fibre mats are inserted.	89
Figure 4.6 SEM images of electrospun PAN NFs deposited on Al collector at various voltages: (a) 16 kV, (b) 17 kV, (c) 18 kV, and (d) 19 kV.	90
Figure 4.7 d_a of PAN NFs and F_A per SEM image as a function of voltage from 10 to 30 kV.	92

Figure 4.8 Optical images of solution drop formed at the needle tip as a function of TCD: (a) 5 cm, (b) 10 cm, (c) 15 cm, (d) 20 cm, (e) 25 cm, and (f) 30 cm.....	93
Figure 4.9 Quantitative plot of d_a of electrospun PAN fibre mat as a function of TCD of 5-20 cm. The photos of electrospun PAN fibre mats including with TCD at 25 and 30 cm are inserted. .	94
Figure 4.10 SEM images of electrospun PAN NFs deposited on Al collector at various TCD: (a) 5 cm, (b) 10 cm, (c) 15 cm, (d) 20 cm, (e) 25 cm, and (f) 30 cm.....	95
Figure 4.11 Optical images of solution drop formed at the needle tip as a function of TCD: (a) 11 cm, (b) 12 cm, (c) 13 cm, and (d) 14 cm.....	96
Figure 4.12 Quantitative plot of d_a of electrospun PAN fibre mat as a function of TCD of 11-14 cm.....	97
Figure 4.13 SEM images of electrospun PAN NFs deposited on Al collector at various TCD: (a) 11 cm, (b) 12 cm, (c) 13 cm, and (d) 14 cm.....	98
Figure 4.14 d_a of PAN NFs and F_A per SEM image as a function of TCD from 5 to 30 cm.	99
Figure 4.15 Optical images of solution drop formed at the needle tip as a function of Q with TCD of 10cm: (a) 0.5 mL/h, (b) 1 mL/h, (c) 1.5 mL/h, (d) 2 mL/h, (e) 2.5 mL/h, and (f) 3 mL/h. ..	100
Figure 4.16 Optical images of solution drop formed at the needle tip as a function of Q with TCD of 14cm: (a) 0.5 mL/h, (b) 1 mL/h, (c) 1.5 mL/h, (d) 2 mL/h, (e) 2.5 mL/h, and (f) 3 mL/h. ..	100
Figure 4.17 Quantitative plot of d_a of electrospun PAN fibre mat as a function of Q of 0.5-3 mL/h with TCD of 10cm and 14 cm, respectively. The photos of electrospun PAN fibre mats are inserted.....	101
Figure 4.18 SEM images of electrospun PAN NFs deposited on Al collector with various Q at TCD of 10 cm: (a) 0.5 mL/h, (b) 1 mL/h, (c) 1.5 mL/h, (d) 2 mL/h, (e) 2.5 mL/h, and (f) 3 mL/h.	103
Figure 4.19 SEM images of electrospun PAN NFs deposited on Al collector with various Q at TCD of 14 cm: (a) 0.5 mL/h, (b) 1 mL/h, (c) 1.5 mL/h, (d) 2 mL/h, (e) 2.5 mL/h, and (f) 3 mL/h.	104

Figure 4.20 d_a of PAN NFs as a function of Q from 0.5 to 3 mL/h with two different TCD, 10 cm and 14 cm.....	107
Figure 4.21 SEM images of electrospun PAN NFs deposited on Al collector with voltage of 16 kV and TCD of 14 cm at various Q : (a) 1 mL/h for 70 min, and (b) 1.5 mL/h for 120 min.....	108
Figure 4.22 Summary of the d_a of PAN NFs electrospun with the optimized processing parameters collected from different samples.....	108
Figure 4.23 Quantitative plot of d_a of PAN mat as a function of C from 2 to 16% at deposition time of 2 and 10 min, respectively. The photos of PAN mats on Al foil collectors are inserted.	109
Figure 4.24 SEM images of electrospun PAN products deposited on Al collector for 2min at various concentrations: (a) 2%, (b) 4%, (c) 6%, (d) 8%, (e) 10%, (f) 12%, (g) 14%, and (h) 16%.	111
Figure 4.25 SEM images of electrospun PAN products deposited on Al collector for 10min at various concentrations: (a) 2%, (b) 4%, (c) 6%, (d) 8%, (e) 10%, (f) 12%, (g) 14%, and (h) 16%. With an exception for 16% with 8min30s deposition time.	112
Figure 4.26 Plot of average diameter of the fibres versus concentration from 2 to 16 wt% at two different deposition time of 2 and 10 min.....	114
Figure 5.1 SEM image of PAN NFs electrospun from 14% PAN solution with optimized processing parameters of 16 kV, 14 cm and 1.5 ml/h. The average fibre diameter distribution plot counted from 100 fibres is inserted as an inset.	117
Figure 5.2 SEM image of electrospun PAN NFs after oxidative stabilisation process. The average fibre diameter distribution plot counted from 100 fibres is inserted as an inset.	118
Figure 5.3 SEM image of stabilized PAN NFs after carbonization process at carbonization temperature of 500 °C. The average fibre diameter distribution plot counted from 100 fibres is inserted as an inset.	119

Figure 5.4 SEM image of stabilized PAN NFs after carbonization process at carbonization temperature of 600 °C. The average fibre diameter distribution plot counted from 100 fibres is inserted as an inset.	119
Figure 5.5 SEM image of stabilized PAN NFs after carbonization process at carbonization temperature of 700 °C. The average fibre diameter distribution plot counted from 100 fibres is inserted as an inset.	120
Figure 5.6 SEM image of stabilized PAN NFs after carbonization process at carbonization temperature of 800 °C. The average fibre diameter distribution plot counted from 100 fibres is inserted as an inset.	120
Figure 5.7 SEM image of stabilized PAN NFs after carbonization process at carbonization temperature of 900 °C. The average fibre diameter distribution plot counted from 100 fibres is inserted as an inset.	121
Figure 5.8 SEM image of stabilized PAN NFs after carbonization process at carbonization temperature of 1000 °C. The average fibre diameter distribution plot counted from 100 fibres is inserted as an inset.	121
Figure 5.9 Quantitative relationship between the average fibre diameter of CNFs and carbonization temperatures.	123
Figure 5.10 FTIR spectra of PAN NFs with various heat treatments: (a) PAN, (b) SPAN, (c) CNF-500, (d) CNF-600, (e) CNF-700, (f) CNF-800, (g) CNF-900 and (h) CNF-1000.	124
Figure 5.11 Raman spectrum of sample CNF-500.....	127
Figure 5.12 Raman spectrum of sample CNF-600.....	128
Figure 5.13 Raman spectrum of sample CNF-700.....	128
Figure 5.14 Raman spectrum of sample CNF-800.....	129
Figure 5.15 Raman spectrum of sample CNF-900.....	129
Figure 5.16 Raman spectrum of sample CNF-1000.....	130

Figure 5.17 R -value and L_a of CNFs as function of carbonization temperature.	131
Figure 5.18 The relationship between X_G and $1000/T$	132
Figure 5.19 The relationship between $\ln X_G$ and $1000/T$	132
Figure 5.20 Low magnification TEM images of CNFs with various carbonization temperatures from 500 to 1000 °C: (a)-(b) CNF-500, (c)-(d) CNF-600, (e)-(f) CNF-700, (g)-(h) CNF-800, (i)-(j) CNF-900 and (k)-(l) CNF-1000. The SAED patterns of CNFs are inserted at top right corner.	133
Figure 5.21 HRTEM images of CNFs with various carbonization temperatures from 500 to 1000 °C: (a) CNF-500, (b) CNF-600, (c) CNF-700, (d) CNF-800, (e) CNF-900 and (f) CNF-1000.	134
Figure 5.22 Cole-Cole plot of sample CNF-500. The electrical circuit of $R_s(R_p//C)$ generated from the fitting curve is inserted as inset.	135
Figure 5.23 Cole-Cole plot of sample CNF-600. The electrical circuit of $R_s(R_p//CPE)$ generated from the fitting curve is inserted as inset.	136
Figure 5.24 Cole-Cole plot of sample CNF-700. The electrical circuit of $R_s(((CPE)(L))/R_p)$ generated from the fitting curve is inserted as inset.....	137
Figure 5.25 Cole-Cole plot of sample CNF-800. The electrical circuit of $R_s(R_p//L)$ generated from the fitting curve is inserted as inset.	138
Figure 5.26 Qualitative illustration of showing the microstructural evolution during the carbonization process as a function of carbonization temperature.....	141
Figure 6.1 SEM image of electrospun PAN NFs.....	143
Figure 6.2 SEM image of stabilised PAN NFs.	144
Figure 6.3 SEM image of carbonized PAN NFs by using conventional furnace.....	145
Figure 6.4 SEM image of bottom side of carbonized PAN NFs by using MPECVD.....	146

Figure 6.5 SEM image of top side of carbonized PAN NFs with CNWs grown by MPECVD. The closer view of CNWs grown on the top side captured at higher magnification is inserted as an inset.	147
Figure 6.6 SEM image of bottom side of carbonized PAN NFs with CNWs grown by MPECVD. The closer view of CNWs grown on the bottom side captured at higher magnification is inserted as an inset.	148
Figure 6.7 Schematic diagram of morphological change of grown CNWs by MPECVD with depth change from the sample surface to the bottom.	149
Figure 6.8 FTIR spectra of PAN NFs treated with various treatments: (a) electrospun PAN NFs, (b) stabilised PAN NFs, (c) furnace carbonized PAN NFs, (d) MPECVD carbonized PAN NFs, and (e) MPECVD grown CNWs on CNFs.	150
Figure 6.9 Raman spectrum of electrospun PAN NFs (sample S-1).....	153
Figure 6.10 Raman spectrum of stabilised PAN NFs (sample S-2).....	154
Figure 6.11 Raman spectrum of furnace carbonized PAN NFs (sample S-3).	155
Figure 6.12 Raman spectrum of MPECVD carbonized PAN NFs (sample S-4).....	156
Figure 6.13 Raman spectrum of CNWs grown on surface layers of CNFs by using MPECVD (sample S-5).	157
Figure 6.14 Raman spectrum of CNWs grown on deeper layers of CNFs by using MPECVD (sample S-6).	157
Figure 6.15 C-V curve of furnace fabricated CNFs in 0.5 M H ₂ SO ₄ at different scan rates of 5, 10, 20, 50, and 100 mV at a voltage range from 0 to 0.9 V.	160
Figure 6.16 C-V curve of MPECVD fabricated CNFs in 0.5 M H ₂ SO ₄ at different scan rates of 5, 10, 20, 50, and 100 mV at a voltage range from 0 to 0.9 V.	161
Figure 6.17 Cycle life of CNFs and CNWs-CNFs in the voltage range from 0 to 0.9V.	162

List of tables

Table 2.1 Summary of mechanical properties of three different type of PAN derived carbon fibres [49].....	40
Table 2.2 Impedance of various electrical circuit elements.	62
Table 3.1 Matrix of processing parameters with various voltages.....	68
Table 3.2 Matrix of processing parameters with various TCD.	69
Table 3.3 Matrix of processing parameters with various Q	70
Table 3.4 Matrix of optimized processing parameters with various PAN solution concentrations from 2 to 16%.	71
Table 3.5 Experimental conditions of PAN NFs with various treatments.	73
Table 3.6 Experimental conditions for PAN NFs with different treatments.....	75
Table 4.1 Quantitative data extracted from SEM images of PAN NFs in the voltage range from 10 to 30 kV.....	88
Table 4.2 Quantitative data extracted from SEM images of PAN NFs in the voltage range from 16 to 19 kV.....	91
Table 4.3 Quantitative data extracted from SEM images of PAN NFs in the TCD range from 10 to 30 kV.....	96
Table 4.4 Quantitative data extracted from SEM images of PAN NFs in the TCD range from 11 to 14 cm.....	98
Table 4.5 Quantitative data extracted from SEM images of PAN NFs with various Q ranging from 0.5 to 3 mL/h at TCD of 10 and 14 cm.	105
Table 4.6 Quantitative data for d_a of PAN NFs with various PAN solution C from 6 to 16% at deposition time of 2min, and 10min, respectively.	113

Table 5.1 Summary of change of d_a with various heat treatments.	122
Table 5.2 Assignment of main FTIR peaks of PAN NFs treated with various heat treatments.	126
Table 5.3 Summary of details extracted from Raman spectra of CNFs carbonized with various carbonization temperatures, ranging from 500 to 1000 °C.	130
Table 5.4 Numerical values of electrical circuit elements extracted from the fitting of Cole-Cole plots by using Matlab.	139
Table 6.1 Summary of average diameter of PAN NFs heat treated at various conditions.	144
Table 6.2 Assignment of main FTIR peaks of PAN NFs treated with various heat treatments.	151
Table 6.3 Assignment of main Raman peaks of PAN NFs treated with various treatments. ν_D , ν_G , $\nu_{G'}$ are the Raman peak position of D peak, G peak, and G' peak, respectively. I_D/I_G represents R -value, is the intensity ratio of D peak to G peak. L_a , graphitic crystallite size, is the ratio of 5.8 nm and the R -value.	159

1 Introduction

The work presented in this thesis is regarding to a preliminary study of synthesis and characterisation of various carbon materials, derived from a high molecular weight polymer, polyacrylonitrile (PAN). The aim of the project was to investigate the characteristics of the carbon materials synthesized from different fabrication methods as well as with various parameters.

PAN was selected as the precursor material throughout the whole project, by taking its privilege as the principal precursor for the production of carbon fibres (CFs) around the world. To obtain one-dimensional carbon material, carbon fibres, and to further fabricate CFs hybrid material based on it; the synthesis of PAN nanofibres (NFs) was prior carried out by using electrospinning technique. The detailed information of all the experiments involved in this project was documented in Chapter 3.

The main stream of this project was divided into three sections, electrospinning of PAN NFs, fabrication of carbon nanofibres (CNFs), and fabrication of CNFs-carbon nanowalls (CNWs) hybrid materials. These results were presented and discussed in Chapter 4, 5, and 6. Electrospinning is rather versatile technique with great sensitivity to produce material with different sizes varied from μm to nm , as well as various shapes, including beads, fibres or the combination of both; which all can be controlled by the selection of parameters. In the current project, three different types of parameters, processing parameters, solution parameter, and collector parameter were investigated. The effect of these three parameters on the morphology was discussed in the first section of Chapter 4. To explore the characteristics of PAN derived CNFs, electrospun PAN NFs with optimized processing parameters at concentration of 14% was later heated treated by oxidative stabilisation in air and followed with subsequent carbonization in N_2 . The effect of carbonization temperature from 500 to 1000 $^\circ\text{C}$ on morphology, functional groups, chemical structure, crystallinity and electrical characteristics was elucidated in Chapter 5.

The discussion on the fabrication of CNFs-CNWs hybrid materials from oxidative stabilized PAN NFs by using microwave plasma enhanced chemical vapour deposition (MPECVD), which was presented at Chapter 6. In this section, the morphology and possible growth mechanism of CNWs on the CNFs were discussed.

Finally, the conclusions of all the findings from these three set of experiments were summarized in Chapter 7. In the same chapter, the recommendations on the future work of this project were also given.

2 Literature review

2.1 Fundamentals of Electrospinning

Inspired by Formaldas, who published the first patent with the description of utilizing electrostatic repulsion to produce polymer filaments in 1934 [1], there has been a growth of interests over the years in using this electrostatic force driven process to fabricate thin fibres. Until early 1990s, this process was named as electrospinning [2]. Up to date, there are more than 50 types of organic polymer that have been electrospun into continuous fibres with diameter ranging from 40 to 2000 nm [2-4]. To demonstrate the finesse of the fibre produced by electrospinning technique, a SEM image of electrospun polyvinyl alcohol (PVA) fibres next to a human hair is presented in **Figure 2.1** [5].



Figure 2.1 SEM image of a human hair and electrospun PVA fibres [5].

Besides its capability of producing polymer fibres with extremely small diameter at nanoscale, a large variety of morphologies and flexible selection of materials have made electrospinning a widely used technique in many university research labs as well as in industries [5, 6]. **Figure 2.2** gives an overview of research aspects on electrospun polymeric NFs [7].



Figure 2.2 Overview of research aspects on electrospun polymeric NFs. The pie chart is redrawn from reference [7].

The basic setup of electrospinning is relatively simple, and is shown in **Figure 2.3**. The prepared polymer melt or solution is loaded into a syringe, in which the solution is delivered at a fixed rate, which is normally controlled by the syringe pump. To enable the fibre ejection travelled from the needle tip to the collector, the electrical field is introduced at given desired distance between the needle tip and the collector, which are respectively connected to a high voltage supply, and ground electrode. Once the charge with the same polarity is introduced to the solution drop at needle tip, the like charges are accumulated on the surface of the electrified solution drop, and causing a competition between the surface tension of the solution drop and electrical forces. As soon as the induced electrical forces surpass the surface tension, the solution drop is changed from hemispherical into conical, known as Taylor cone. This name was originated from the early research in 1969 conducted by Sir Taylor, who determined the semi-vertical angle (α) of Taylor cone to be 49.3° from the jet produced from the droplet of polymer solution [8]. In more recent publications, Taylor cone α equal to 33.5° and 50° were reported [9-12]. The fibre ejection is

initiated at the tip of Taylor cone, and is finally collected on the collector after undergone stretching and whipping process [13].

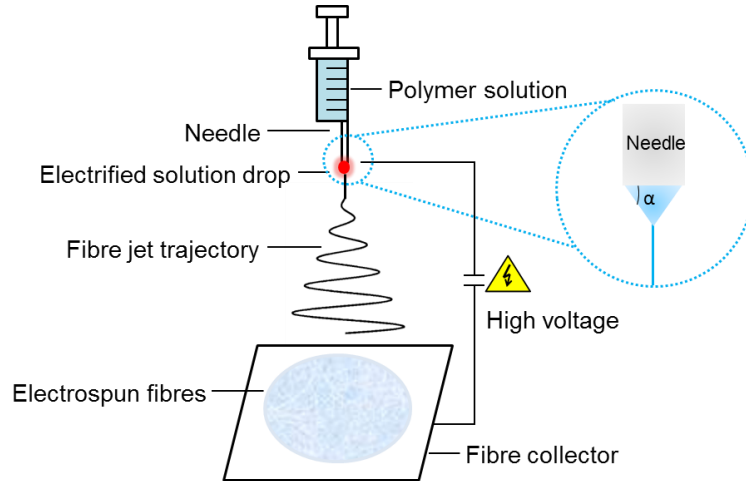


Figure 2.3 Schematic diagram of electrospinning setup with zoom-in image of a semi-vertical angle (α) of Taylor cone.

The initiation of electrospinning setup appears to be simple and straightforward, as described briefly as above. However, understanding the fundamentals can be rather difficult and still is remained as a great challenging. As indicated in **Figure 2.2**, the major efforts are being focused on the tailoring of desirable morphology and structure with exceptional properties, and gaining the understanding on the jet formation and setup of electrospinning. The former effort is essential in the advancement of application performance, whereas the latter contributes to the scientific understanding which reinforces the former one.

From a viewpoint of scientific understanding, electrospinning mechanism involves an extremely complex interaction among of a few physical topics, such as surfaces, shapes, rheology and electrical charges [14]. As described by Reneker and Chun, a stable electrospinning has four distinct regions, base, jet, envelope and collector [2]. The base is the region where the initiation of fibre ejection occurs. This only happens when the induced electrical forces given by the high

voltage supply reach or be greater than the threshold value, V_c , with respect to the surface tension, which can be approximated by using **Equation 2.1** [15].

$$V_c^2 = 4 \left(\frac{H^2}{L^2} \right) \left(\ln \frac{2L}{R} - 1.5 \right) (0.117\pi R\gamma) \quad \text{Equation 2.1}$$

Where V_c represents the threshold value with unit of kV, H is the tip-to-collector distance (TCD) in cm, L and R represent the length and outer radius of the needle with unit of cm, and γ is the surface tension of polymeric solution with unit of dyn/cm.

The jet region and envelope region are the regions define the trajectory path of the fibre ejection, and in turns to decide the morphology of the electrospun fibre. The main role of these two regions is for fibre jet thinning. In 1996, the conical envelope region in **Figure 2.4(a)** within the needle TCD was thought to be the result of splitting of a single jet into many thinner jets, called splaying. Five years later, using high-speed camera has revealed that the envelope region is in fact being a single jet with high frequency of whipping and bending, and is shown in **Figure 2.4(b)** [16]. Although splitting into thinner jets still occurs in some cases, getting the true image of conical envelope region has ruled out the splaying of being the dominant process during the electrospinning [16].



Figure 2.4 Photographs of fibre ejection trajectory of polyethylene oxide solution during electrospinning, captured with two different scales: (a) 1/250 s, and (b) 18 ns [16].

Figure 2.5 demonstrates the fibre ejection trajectory under the influence of the bending instability [14, 17].



Figure 2.5 Schematic diagram of bending instabilities developed during the fibre ejection of electrospinning [14, 17].

2.2 Effect of Parameters

A large diversity of the morphology offered by electrospinning made it a very exciting technique to work with [18]. However, such great flexibility in generating various morphologies is in fact gifted from its high sensitivity, which sometimes lead to the undesired morphology towards to its designated applications. In order to fully utilise benefits of electrospinning while avoiding the associated potential shortcomings, a tremendous amount of work regarding to the investigation of effect of many parameters of electrospinning on the resulted morphology were carried out. In

the following subsections, a few major parameters of electrospinning were reviewed. To pursue more comprehensive reviews, the relevant information can be found in the following references [5, 6, 19-22].

2.2.1 Processing Parameters

In many literature, processing parameters is a collective name for three individual parameters: voltage, TCD and flow rate (Q), respectively [23-28]. Among all parameters that affect the morphology of resulted electrospun fibres, the processing parameters are probably the most significant ones based on the working mechanism of electrospinning. It is well known that the fibre ejection occurs when the surface tension of the solution is overcome by the induced electrical forces [13]. Deitzel *et al.* reported that the critical voltage for the jet initiation from 7 wt% PEO solution was 5.5 kV [29]. At this condition, the electric current associated with the electrospinning was measured to be approximately 10 nA and the resulted fibres were bead-free [29]. As the voltage increased to 7 or 9 kV, the bead density was increased significantly and this observation was more pronounced at higher voltage values [29]. The electric current measured at voltage 7 and 9 kV were ~60 and ~180 nA, respectively [29]. In their experiment, they demonstrated the strong electric current dependence on voltage [29]. In addition, they noticed that once the voltage applied on system was above the critical voltage the bead density was increased significantly by increasing voltage from 5.5 to 9 kV [29]. Furthermore, they suggested that the increase of bead density was a result of increasing instability of the electrospinning system, which can be reduced by tuning other two processing parameters, TCD and Q [29]. Similar observation was reported by Jalili *et al.* by electrospinning of 15 wt% PAN solution [23]. By increasing voltage from 9 to 12 kV while maintaining TCD of 15 cm and Q of 2 mL/h constant, it was found that the smooth fibres changed into beaded ones [23]. In addition, they noticed that the solution drop suspended on the needle tip was changed along with changing voltage [23]. In the case of smooth fibres, the jet was ejected from the stable Taylor cone originated from the needle tip in the voltage range of 9-10 kV [23]. Whereas for these beaded fibres formed at high voltages from 11 to 12 kV, the

volume of the solution drop suspended on the needle tip was greatly reduced, and causing the jet ejected from the liquid surface within the needle tip [23]. For the observation described as above, it was explained as the mass imbalance caused by the increased voltage, in terms of the rate of the solution on the needle tip consumed quicker than that of was delivery to the needle tip [23, 29]. Fang *et al.* electrospun 7 wt% PAN solution into an ethanol bath for rapid solidifying the resulted fibres [30]. By increasing TCD from 2 to 10 cm while voltage and Q were fixed at 18 kV and 1 mL/h, the resulted polyacrylonitrile (PAN) nanofibres (NFs) were changed from beaded into bead-free ones [30]. In addition, the resulted fibre diameter was generally decreased with increasing TCD [30]. Wang *et al.* attempted to study the effect of Q on fibre diameter of PAN NFs, electrospun from various PAN solution concentrations, ranging from 5.1 to 20.3 wt% [31]. They found that with increasing Q from 0.5 to 6 mL/h the fibre diameter was increased for all the above mentioned PAN solution concentrations [31]. A different result was reported by Liu and Adanur, who studied the effect of Q on fibre diameter from 10 wt% PAN solution [26]. According to their results, no significant impact from increasing Q was observed on the resulted PAN NFs [26]. However, they mentioned that the difference between the smallest and largest fibre diameter obtained within this Q range was 82 nm [26].

2.2.2 Solution Parameters

Solution parameters are another group of interesting parameters that affect the morphology in its own unique way. In general, solution parameters can include polymer type, polymer concentration, viscosity, solution conductivity, molecular weight of polymer, and surface tension [18, 25, 28, 31-33]. One of the most well researched solution parameters is solution concentration [18, 25, 31, 34]. Lee *et al.* specifically studied the effect of polystyrene (PS) solution concentration on the aspect ratio of bead [25]. The aspect ratio of the bead was defined as the ratio of bead length along the fibre axis to the one perpendicular to the fibre axis [25]. They found that the aspect ratio of the beads increased continuously with increasing concentration from 7 to 13 wt%, which led the beaded fibres to be smooth fibres [25]. Fong *et al.* studied the concentration

effect of poly(ethylene oxide) (PEO) on the morphology of the resulted fibres [18], as shown in **Figure 2.6**. It can be clearly seen that the diameter of the beads decreased with increasing solution viscosity from 13 to 1835 centipoise [18]. It was not only the morphology of the bead changed from spherical to spindle-like shape, then to bead-free fibres; but also the fibre diameter was increased from ~80 to 250 nm [18]. Demir *et al.* observed that the polyurethane fibre diameter was increased significantly by increasing concentration from 3.8 to 12.8wt% [24]. Based on these results, they noticed that the relationship between the diameter (d) and concentration obeyed the following relation $d \propto \text{concentration } (C)$ [24]. It seems that even by using different polymer solution, it is always that by increasing concentration the diameter of the fibres resulted in a larger diameter. However, the relationship between the d and C may vary with different polymer. He *et al.* found that the PAN fibre followed linear relationship between fibre diameter and solution concentration (i.e. 9-18 wt %) [35]. In addition, they also established the relationship between viscosity (η) and C , which was $\eta \propto C^6$ [35].



Figure 2.6 Morphology transformation of PEO electrospun fibres induced by increasing viscosity of PEO solution [18].

When it comes to fabricate of composite fibres by using electrospinning technique, the compatibility between the polymer solution and dispersed phase is quite important. Ko *et al.* attempted to prepared two type of polymer composite fibres with addition of purified single wall carbon nanotubes (SWNTs) [33]. They found the SWNTs only aligned well within PAN polymer matrix as shown in **Figure 2.7**, whereas using polylactic acid (PLA) solution led to the serve agglomeration within the electrospun PLA fibres [33]. They explained that the difference

appeared between two polymer matrix was partially due to their different conductivity and wetting ability [33].



Figure 2.7 Electrospun PAN NFs with SWNTs well aligned within the fibre matrix [33].

To fabricate composite nanofibres by using electrospinning, besides SWNTs were used as dispersing material, nanodiamonds (NDs) in powder form were also employed. Behler *et al.* introduced NDs into PAN fibres with concentration of NDs ranging from 0 to 90 wt% in a 8 wt% PAN solution [32]. According to their measurements, the PAN fibre diameter was decreased from 32 to 15 nm with increasing the concentration of NDs from 0 to 17 wt% [32]. With further increasing the concentration of NDs to 20-60 wt%, both the size and the number of the beads were increased [32]. **Figure 2.8** shows the electrospun PAN fibres with the addition of 10 wt% NDs. The resulted fibres exhibited relatively smooth fibres with few beads [32]. Although there were some minor agglomerations of NDs can be seen in **Figure 2.8**, this might be still so far the thinnest PAN fibres with least agglomeration at this given conditions [32].



Figure 2.8 (a) SEM image of PAN nanofibres fabricated from 8 wt% PAN solution with addition of 10 wt% NDs; (b) TEM image of single NDs loaded PAN nanofibres with highlight of NDs location [32].

To obtain interesting morphology besides from adding additives into the polymer matrix solution, as the ones explained in the above, changing the solvent or humidity might be as well create enough difference. Bognitzki *et al.* selected dichloromethane with very high vapour pressure as a solvent to produce electrospun fibres from three different polymers [36]. One of which was a partially crystalline poly-L-lactide (PLLA); and the other two were amorphous polymers, polycarbonate (PC) and polyvinylcarbazole [36]. As presented in **Figure 2.9**, the resulted fibres exhibited many pores on the surface [36]. They suggested that the pore formation was due to the rapid phase separation [36]. The locations where pores appeared were solvent rich area, hence became pores during the electrospinning process [36]. The pore structures were also observed in amorphous polymers, which showed pores with circular shape instead of elongated, and also the distribution of the pore size was narrower [36]. Furthermore, they reported that by replacing dichloromethane with chloroform which has lower vapour pressure, the tendency of the pore formation on the resulted fibres was remarkably decreased [36].



Figure 2.9 Electrospun PLLA fibres electrospun from dichloromethane solvent with a high vapour pressure [36].

2.2.3 Ambient Parameters

Apparently, applying solvent with high vapour pressure was is not the only solution to obtain fibres with pores. Casper *et al.* studied the effect of humidity on the morphology of electrospun PS fibres [37]. They carried out their experiment in five humidity ranges: < 25%, 31-38%, 40-45%, 50-59%, 66-72%, respectively [37]. At humidity level below 25%, the surface of the resulted fibres were ordinary with no special features [37]. By increasing humidity level to higher, not just the number of the pores increased, the range of the pore size and the size of the most frequent pores were increased [37]. On the other hand, Baumgarten investigated the environmental effect on the electrospinning of PAN fibres [27]. He indicated that the normal humidity level for electrospinning of PAN in air was 30-40% [27]. By dropping humidity down to less than 5%, the electrospinning was disabled within 1-2min because of solution drying out at the needle tip [27]. By elevating humidity level to be greater than 60%, the collected fibres were tangled and considered to be wet [27]. In addition, he found that electrospinning of PAN fibres in helium environment was not possible [27]. Because at voltage of 2.5 kv, the gas was found breaking down electrically [27].

Electrospinning technique is a highly sensitive technique. Temperature is also considered as one of the ambient parameters that can cause the difference in the electrospinning process, hence the morphology of the resulted fibres [38]. Wang *et al.* applied a jacket type exchanger to control the temperature of the 12 wt% PAN solution during the electrospinning process [38]. They found by increasing solution temperature from 32.2 to 88.7 °C, the straight segment of the jet was decreased from 12.29 to 2.34 mm [38]. The diameter of the PAN fibres was decreased from approximately of 1064 to 463 nm [38]. They attributed the diameter reduction to the combining effect of decreased surface tension and viscosity, and increased electrical conductivity, which was induced by increasing temperature [38].

2.2.4 Needle Type

Wang *et al.* also investigated the effect of needle size on the electrospinning process and the resulted fibre diameter of PAN nanofibres [38]. During this experiment, the PAN solution with concentration of 8 % was applied and was maintained at room temperature [38]. By increasing needle inner diameter from 0.31 to 2.16 mm, the straight segment of jet was increased from 2.42 to 7 mm, while the resulted PAN fibred was increased from approximately of 256 to 502 nm [38]. Kizildag *et al.* found similar impact on the fibre diameter of electrospun silk fibroin NFs brought by increasing needle size from 0.7 to 1.25 mm [39]. However, the increase in terms of silk fibroin NFs was small, and the difference between two ends was ~10 nm [39].

In more recent years, coaxial needle was attracted lots of attentions due to the capability of engineering nanofibres with hierarchical structures in a simple way. As illustrated in **Figure 2.10(a)**, two different materials can be introduced into an inner and outer capillaries at the same time, the electrospun fibres end up with a structure containing core material surrounded by the shell material [40, 41]. Saraf *et al.* fabricated electrospun fibres with core material of poly(ethylene) (PEG) and shell material of poly(ϵ -caprolactone) (PCL) by using coaxial

electrospinning technique [41]. The resulted fibres with two different colour under the confocal microscopy, indicating red as shell material, mainly PCL, while green represented core material of PEG [41]. They found that the diameter of the coaxial fibres was increased as the concentration of shell material increased [41]. The shell material also showed a strong influence on the diameter of core fibre [41]. Furthermore, similar to the single polymer-solvent electrospinning technique, the concentration of core material showed positive impact on the diameter of the core fibres [41].



Figure 2.10 (a) schematic diagram of coaxial electrospinning setup at needle part [40], (b) the electrospun fibres with core-shell structure produced from coaxial electrospinning [41].

2.2.5 Collector

In most cases, the deposition of electrospun fibres are happened on conducting collectors. To explore if the collector material show any impact on the morphology of the electrospun fibres, Liu and Hsieh electrospun cellulose acetate (CA) fibres on four different collector materials: copper mesh, aluminium (Al) foil, paper and water [42]. Liu and Hsieh noticed that the electrospun fibre packing was affected by the electrical conductivity of the collector [42]. In the case of conductive collectors, the charges carried by fibres were easier dissipated, hence tighter packing of fibres on the collectors [42]. As oppose to conductive collectors, the static charge tend

to accumulate on the insulator surface [42]. Looser packing of fibres were expected in other cases [42]. As demonstrated in **Figure 2.11**, the NUS pattern formed by the electrospun fibre deposition on the glass surface [43]. The idea of making this possible was to manipulate the electrical field during the electrospinning by placing the electrical conductive wire with same pattern place below the glass substrate [43]. Because the wire was connected to the ground electrode, the highly charged jet was naturally preferred to be deposited on these ‘marked’ area, guided by the electrostatic forces [43]. More interesting electrospinning designs can be found in the reference [43].



Figure 2.11 (a) Electrospun fibres deposited on glass substrate showing NUS pattern; and (b) the NUS metal wires placed below the glass surface [43].

To serve the applications where highly ordered architectures are required [44], a few smart designs in terms of electrospinning setup have been developed. Theron *et al.* have switched the collector from a simple flat conductor into a rotating disk collector [45]. By using the rotating

disk collector, the jet trajectory was different from the ones described for the fabrication of non-woven fibre mat [45]. Instead, the envelope region started to shrink at a certain point above the wheel of rotating disk and the forming an inverted envelope with its tip landing on the edge of the wheel [45]. More interestingly, the electrospun fibres fabricated in this manner resulted into parallel arrays [45]. To increase the collecting area where the aligned fibres were deposited, Li *et al.* have used a pair of Si electrodes which allowed the separation distance between 2 electrodes varied from hundreds of micrometre to a few centimetres, as illustrated in **Figure 2.12(a)** [46]. **Figure 2.12(b)** demonstrates the electrical field strength vectors within the TCD. Differing from common electrospinning, the electrical field lines near collector area were splitted into 2 portions toward to the opposite direction. In this regard, the charged fibres were considered to be experienced two set of electrostatic forces, F_1 , the force originated from the splitting field; and F_2 , the force generated from the image charges induced on the surface of 2 electrodes by contacting with charged fibres. Under the interaction of these two forces, the resulted poly(vinyl pyrrolidone) (PVP) fibres were highly aligned between two Si electrode and are shown in **Figure 2.12(c)**.



Figure 2.12 (a) Electrospinning setup used in the fabrication of aligned NFs; (b) an illustration of electric field strength between needle tip and Si collectors; and (c) optical image of aligned PVP NFs formed between a pair of Si collectors [46].

By integrating the knowledge acquired from the fabrication of aligned fibres with coaxial electrospinning, the aligned electrospun fibre with hollow structure located in the centre was achieved. **Figure 2.13(a)** demonstrates this smart idea by letting PVP/Ti(OiPr)₄ solution and mineral oil to flow through the outer and inner capillary simultaneously [47]. By immersing the resulted co-electrospun composite NFs in octane overnight, the pure titania hollow NFs were formed after the calcination in air at 500 °C. The good alignment of hollow NFs shown in **Figure 2.13(b)** was achieved by using the same method as described in reference [46].



Figure 2.13 (a) Electrospinning setup used in the fabrication of core-shell structure; and (b) SEM image of aligned titania hollow fibres with inset of magnified single fibre [47].

2.3 Background of Carbon Fibres

The first emergence of carbon fibre has to be tracked back to 1879. Around that time, Thomas Edison has made carbon fibres from cotton threads and bamboo, which were used as filaments of incandescent lamp [48]. **Figure 2.14** shows a light bulb at early stage of Edison's research. Although the filament of light bulb was eventually replaced by tungsten wire [49], the concept of producing carbon fibres from cellulose materials have given the important inspiration for the later carbonization of other polymeric materials, which started to happen in late 1950s [50].



Figure 2.14 Photograph of Edison's early light bulb [51].

In the need of searching substitute material for the control grid of vacuum tube power amplifier during the World War II; Union Carbide Corporation carried out a series of investigations, and led to the invention of carbon fibres derived from rayon, PAN and pitch in 1959, 1961, and 1963, respectively [50].

Generally speaking, a fibre contains at least 92 wt% carbon can be defined as a carbon fibre [52]. In principle, any polymeric fibre with carbon back-bone is considered to be able to use as the precursor of carbon fibre [53]. There are other polymeric materials, such as poly(vinyl alcohol)

(PVA), poly(vinylidene fluoride) (PVDF), polybenzimidazol (PBI), phenolic resin and lignin match the description, and have been attempted of using as carbon fibre precursors [50, 53]. The resulted carbon fibres from these precursors either show weak mechanical properties or associate with high costs [54]. The great carbon yield and superior mechanical properties of the resulted carbon fibres have guaranteed the predominating position of PAN precursor fibres in the carbon fibre industry [50, 55, 56]. It has been reported that 90% of commercial carbon fibres around the world are converted from PAN [55].

2.3.1 PAN Derived Carbon Fibres

In carbon fibre industry, the conversion from PAN into carbon fibres normally are required at least two heat treatments, stabilisation and carbonization [55, 56]. **Figure 2.15** shows an apparatus that used for the manufacturing of continuous high modulus carbon yarns and fibres, which was patented by Prescott *et al* [57]. The PAN precursor fibre was firstly stretched in a steam atmosphere in order to acquire a preferred orientation, which is parallel to fibre axis [49]. With the tension applied, the PAN fibre was then subjected to a stabilisation process which took place in air environment at a temperature range normally between 200 and 300 °C [56, 58]. Upon to the completion of the stabilisation process, a ladder structure can be formed so that the chain scission and relaxation of the fibre can be avoided during the subsequent carbonization process in an inert atmosphere at much high temperatures (i.e. 500-2500 °C) [58], hence led to the formation of high strength and high modulus carbon fibres [49].



Figure 2.15 Manufacturing process of carbon yarns and fibres from PAN [57].

Depends on the application of carbon fibres, different type of carbon fibres can be produced by tuning the carbonization temperature. In general, PAN fibre carbonized at up to 1000 °C refers as Type A carbon fibre, which normally exhibit low tensile strength and low modulus [58]. By increasing carbonization temperature up to 1400 °C, the resulted carbon fibre possess high tensile strength and medium modulus, which is known as Type II [58]. With further increasing carbonization temperature to be greater than 2500 °C, sometimes refers as graphitization process; Type I carbon fibre can be produced with an exceptional modulus at a expense of decreased tensile strength [58]. The general mechanical properties of PAN derived carbon fibre are summarized in **Table 2.1**.

Table 2.1 Summary of mechanical properties of three different type of PAN derived carbon fibres [49].

Mechanical properties	Standard Modulus	Type II	Type I
		Intermediate Modulus	High Modulus
Modulus (GPa)	205-235	275-310	345-550
Tensile strength (GPa)	3.45-4.65	4.35-6.9	1.86-4.14
Tensile strain, %	1.4-1.6	1.6-2.2	0.81-0.9
Density (g/cm ³)	1.76-1.79	1.76-1.79	1.87

To produce carbon fibres with desired properties, besides the careful control on the fabrication of precursor fibres, the selections on the suitable heat treatment parameters also plays a crucial role. Therefore, lots of efforts have been made in order to understand the reaction mechanism of the each heat treatment.

The fabrication of carbon fibres from PAN fibres starts from the stabilization process in air. This process is considered as one of most complicated ones, which is involved of numerous chemical reactions, including cyclization, dehydrogenation, aromatization, oxidation and crosslinking [59]. The chemistry change of PAN structure during the stabilisation proposed by Fitzer and Heine is presented in **Figure 2.16** [60].



Figure 2.16 Proposed chemistry change of PAN during the oxidative stabilisation process [60].

Although the stabilisation can be carried out in an inert atmosphere, the presence of oxygen in the fabrication environment is essential for many occurred reactions associated with stabilisation process. For instance, dehydrogenation reaction is the process that stabilizes the carbon chains by forming the double bonds. To enable this reaction, the oxygen needs to be presented as to facilitate two elementary steps associated, oxidation and elimination of water [55]. This reaction is presented in **Figure 2.17**.



Figure 2.17 Schematic diagram of dehydrogenation reactions during the stabilisation of PAN fibres with two different structures: (a) PAN fibres, and (b) cyclized PAN fibres [55].

According to the finding reported by Fitzer and Muller, who indicated that oxygen acts as an initiator of the active centre for cyclization reaction [61]. Although oxygen is not required in order for cyclization reaction to occur, having oxygen allows the formation of oxygen-bearing groups attached to the resulted ladder structure and can provide better thermal stability during the carbonization process [62]. Interestingly, cyclization was the idea came up by Houtz, who observed the colour change during the PAN stabilization in 1950 [63]. It is now convinced that the cyclization is the important reaction occurred during the stabilisation [55]. This reaction is an exothermic process which is expected to associate with the evolution of various gases as a result of non-carbon removal process [64]. In addition, this reaction also leads to the conversion from $C\equiv N$ into $C=N$ groups to form a stable ladder structure, holds all molecules together and being responsible for the stiffness of the resulted material [65].



Figure 2.18 Chemistry changes induced by the carbonization process at different carbonization temperatures [60].

Once the ladder structure is established after the course of a proper stabilisation process, the stabilized PAN structure undergoes the carbonization process in an inert atmosphere at higher

temperatures to yield carbon content to around 95%, while leaving the fibrous morphology uncompromised [58]. As indicated in **Figure 2.18**, the dehydrogenation is normally occurred at temperature between 400 and 600 °C, whereas the dehydrogenation is expected taken place at a temperature range from 600 to 1300 °C [60, 66].

At lower carbonization temperature, the cyclized polymer structure is linked up forming a graphite-like ribbon structure, and are bound by nitrogen atoms, as shown in **Figure 2.19**. The further growth into a sheet like structure from ribbons is encouraged at higher carbonization temperature, when denitrogenation normally occurs [52]. It was reported that the sheet like structures contain voids and defects [52]. By further increasing carbonization temperature, these voids and defects can be reduced, the further growth of sheet like structure into graphite-like layers, as well as the improved alignment of basal planes [49, 58].



Figure 2.19 Schematic diagram of graphite like ribbon structure formed due to dehydrogenation during the carbonization process at low carbonization temperature [67].

2.3.2 Vapour-Phase-Grown Carbon Fibres

Apart from the thermal conversion from polymeric fibres, carbon fibres can also possibly be grown directly from carbon containing gases with the assistance of metallic catalysts [56]. This group of carbon fibre is termed as vapour-phase-grown carbon fibres (VGCFs). To compare with PAN derived carbon fibres, VGCFs generally exhibit better electrical conductivity and elastic modulus, which were thought to be the result of greater orientational alignment of carbon planes [68].

Figure 2.20 shows that the growth of VGCFs can be facilitated in a furnace by using a simple temperature profile [68].



Figure 2.20 Heat treatment profile programmed for the fabrication of VGCFs at temperature of 1100 °C [68].

In 1988, Endo reported that there were three main steps involved in the formation of VGCFs [68]. Seeding with catalysts, growth of fine fibre in the vapour made of hydrocarbons diluted with hydrogen, and further growth in the radical direction of the fibre [68]. One of the proposed growth mechanism of VGCFs is presented **Figure 2.21** [69]. The substrate surface is normally catalysed

by seeding of metallic nanoparticles. The seeded locations thus serves as nucleation sites to provide the foundation for the onset of second step. The hydrocarbon decomposition acts as the “nutrition supplier” to promote the deposition of carbon species, preferably sp^2 around the metallic particles. The linear growth of the fibre is continued until the metallic particles are covered with carbon, and possibly other impurities. The radical growth of primary formed fibre is carried on due to the continuous decomposition of hydrocarbons [68]. Endo also pointed out the essential roles of hydrogen: (i) to reduce metallic particles at high temperature of ~ 1100 °C; and (ii) to improve the yielding of VGCFs [68]. On the other hand, Rodriguez *et al.* noticed that the effect of size on the conformation of the resulted carbon structure [70]. In reference [70], it was pointed out that the by using metallic particles with size smaller than 25 nm led to the formation of carbon nanotubes (CNTs), the growth of carbon nanofibres (CNFs) is occurred in otherwise.



Figure 2.21 Growth mechanism proposed for the formation of VGCFs [69].

2.3.3 Characterisations of Carbon Nanofibres

In order to obtain the carbon nanofibres (CNFs) with good quality, understanding the effect of each fabrication parameter on the properties of the final product is of a great importance. To serve this purpose, tremendous characterisation work have been carried out by using many advanced techniques.



Figure 2.22 TEM image of CNFs fabricated by two different methods: (a)-(c) heat treatment of PAN NFs by electrospinning [71], and (d)-(f) vapour phase growth [72].

It is well known that the properties of CNFs is greatly affected by its morphology [73]. **Figure 2.22** shows the TEM images of CNFs produced from different methods. **Figure 2.22 (a)-(c)** presents the appearance CNFs obtained from electrospun PAN NFs after carbonization at 1100 °C [71]. In **Figure 2.22 (a)-(b)**, the morphology of the PAN derived CNFs are considerably uniform and average fibre diameter of PAN derived CNFs was reported to be approximately 80 nm in reference [71]. By observing high resolution TEM image in **Figure 2.22(c)**, the surface layer is found to be much better graphitized than the core area (i.e. inner part) of the fibre. The inner part was found to be formed from the random mixture of ordered graphitic domains and amorphous phases [71]. Rafique *et al.* reported that the size of the ordered graphitic domains within the inner part was 4.3 nm and the thickness of the surface layer was approximated to be 15-20 nm [71]. Similar to the proposed growth mechanism of vapour grown CNFs, the resulted CNFs in **Figure 2.22(d)** shows a tiny tube within it [72]. The diameter of the hollow part was reported to be similar with the diameter of metallic particle used during the seeding [72]. The closer view of surface layer of vapour grown CNFs formed at 1200 °C is shown in **Figure 2.22(e)**. Based on the resulted diffraction pattern, this structure is considered to be a typical turbostratic structure. In contrast, the vapour grown CNFs heated treated at 2800 °C shows the sharp (00 l) spots on the selected area electron diffraction (SAED) pattern in **Figure 2.22(f)**. There is a thin amorphous layer with approximately 5 nm deposited on the stiff, regular flat carbon layers is known as contaminated carbon, which was reported to be originated from the industrial graphitization process [72].

Although the mechanical properties and electrical conductivity of CNFs grown from vapour phase with right fabrication parameters can be very good [72], the short length of the resulted CNFs and low product yield cause the difficulty to be used in the applications where good alignment, and easy assembly are required [56]. From this point of view, PAN derived CNFs from electrospinning appears to be a much more favourable option, in terms of simplicity, flexibility, high efficiency, as well as low costs [56].

One of the most common tools to study the heat treatment history of the fabricated CNFs is using SEM. Due to the unique structure of PAN NFs, two treatments were required, namely, stabilisation and carbonization. Zhou *et al.* reported that by stabilising electrospun PAN NFs with heating rate of 2 °C/min in air to 280 °C for 3h, little change was found on the average diameter of the NFs [74]. To optimize the stabilisation conditions, differential scanning calorimetry (DSC) was often applied [73, 75]. Arshad *et al.* attempted stabilisation process at three different temperatures, 250, 275, and 300 °C, respectively for 1h, by DSC [73]. The resulted DSC data suggested that the complete stabilisation occurred at 300 °C [73]. With further increasing stabilisation temperature, the PAN NFs were combusted [73]. Once the infusible ladder structure is established after using the appropriate stabilisation conditions, carbonization process was applied as the subsequent step leading to the formation of CNFs [55, 75]. Panapoy *et al.* studied the effect of carbonization temperature on the diameter of PAN derived CNFs [76]. It was found that, by increasing carbonization temperature from 800 to 1000 °C with heating rate of 5 °C/min and holding time of 10 min, the diameter of the resulted CNFs was decreased from approximately of 275 to 208 nm [76]. Rafique *et al.* found that by increasing carbonization temperature from 750 to 1100 °C with heating rate of 0.5-5 °C/min and holding time of 1h in N₂ environment, the diameter of the CNFs was decreased from 100 to 80 nm [71]. Zhou *et al.* used SEM to study the effect of carbonization temperature on the aligned PAN NFs [74]. With heating rate controlled at 2 °C/min during the carbonization process at 1000 °C in a N₂ atmosphere, the diameter of CNFs was decreased from ~330 to 250 nm [74]. By further increasing carbonization temperature to 1800 °C, the diameter was further decreased to approximately of 220 nm [74]. It was pointed out that with increasing heat treatment temperature (HTT) of carbonization during the fabrication of carbon fibres from PAN, non-carbon substances were evolved as various gases, as shown in **Figure 2.23** [77]. In **Figure 2.23**, various gases evolved during the carbonization process include H₂, CH₄, CO, CO₂, H₂O, N₂, NH₂ and HCN [77]. Interestingly, it is found that the amount of evolved gases was increased with increasing carbonization temperature [77].



Figure 2.23 Evolution of various gases as function of carbonization temperature [77].

It should be mentioned that when high stabilisation temperature was applied, the H₂O vapour might be escaped due to the reactions involved in the stabilisation process [78], as illustrated in **Figure 2.17** for dehydrogenation reaction. On the other hand, Ko carried out the elemental analysis on the carbon fibres [77, 78], which was produced at various carbonization temperatures [58]. The H₂ content was decreased from ~3.2 to almost 0 wt% with increasing carbonization temperature from 400 to more than 1000 °C [58]. In parallel, as carbonization temperature increased from 400 to 1300 °C; the N₂ content was decreased from ~20 to less than 2 wt%, while O₂ content was dropped from ~15 to 1.5 wt% [58]. This in turn led to the increase in carbon content from above 60 to ~96 wt% [58].

Fourier Transform Infrared (FTIR) spectroscopy is particularly useful in providing information regarding to the stabilisation and carbonization of PAN NFs at low carbonization temperatures. The complicated chemical reactions associated with stabilisation and low temperature carbonization, which can be revealed by the presence of corresponding functional groups on the FTIR spectrum. Ko stated that the PAN fibres after the stabilisation conversion from C≡N groups into C=N [58]. This in turn causing the intensity of the FTIR peak corresponding to C≡N groups at around 2241 cm⁻¹ to reduce, while the appearance of new peak at 1590 cm⁻¹ due to the formation

of C=N, C=C, and N=H [79]. As mentioned in early section 2.3.1, the stabilisation process also involves oxidation reaction, the peak at around 1700 cm^{-1} attributed to C=O is expected [52]. By the time that there is almost no functional group can be seen in FTIR spectrum, it is an indication that the turbostratic structure of PAN derived CNFs are formed [73].



Figure 2.24 Simplified turbostratic microstructure for PAN derived carbon fibre [80].

The turbostratic structure is typical for the CNFs derived from polymer precursor [49]. The formation of such unique structure has been attributed to the presence of defects, stacking faults and dislocations [49]. The structural disorders are considered to be originated with sp^3 bonding, which is co-existed with sp^2 bonding, representing graphitic structure within the turbostratic structure, as shown in **Figure 2.24** [80]. As indicated in **Figure 2.24**, the stack height of the ribbons is represented by L_c , whereas L_a is the graphitic crystallite size representing the straight section of the fibril [49, 80]. To probe the structural disorders and graphitic structure, Raman spectroscopy is a powerful technique to reveal the carbonization degree of the CNFs. It can be seen that in **Figure 2.25**, two peaks appeared in Raman spectra of PAN derived CNFs [69]. They are known as D peak and G peak, originated from A_{1g} zone-edge phonon associated with disorder and finite crystalline size, and zone-centre E_{2g} mode induced by crystalline graphite [71]. More

interestingly, the degree of carbonization or graphitization can be reflected by the ratio of these two peaks, which is varied with carbonization temperature [69].



Figure 2.25 Raman spectra of PAN derived CNFs produced from various carbonization temperatures, ranging from 700 to 2800 °C [69].

As the carbonization degree of the CNFs is increased, the ratio of *D* peak to *G* peak, known as *R*-value, which is decreased. It might be worth mentioning along that in the highly carbonized CNFs, second-order Raman features, such as *G'* peak around 2700 cm⁻¹ is normally seen [81]. This peak is known as the overtone of *D* peak [82]. It was reported the sharpness of the *G'* peak is affected by the crystallinity. In general, the emergence of *G'* peak generally indicates the formation of highly ordered carbon structures [81, 83, 84]. Thanks to the empirical equation proposed by Knight and White [85] shown in **Equation 2.1**.

$$L_a(\text{nm}) = \frac{4.4}{R} \quad \text{Equation 2.1}$$

Based on the magnitude of *R*-value, many authors have been able to quantitative study the carbonization degree of CNFs. Wang *et al.* reported that with increasing carbonization

temperature from 600 to 1000 °C the L_a of PAN derived CNFs was increased from 1.5 to 2.6 nm [86]. Panapoy *et al.* suggested that by increasing carbonization temperature from 800 to 1000 °C, L_a was increased from 1.48 to 3.79 nm [76]. Rafique *et al.* calculated that the L_a was increased from 4.17 to 4.62 nm with increasing carbonization temperature from 750 to 1100 °C [71].

It was later discovered that the R -value is varied with laser excitation wavelength. The empirical equation proposed by Knight and White is considered valid in the case when the laser wavelength of 514 nm is used. With applying different laser excitation wavelength of Raman experiment, the constant in **Equation 2.1** will need to be modified. Niu *et al.* stated that the empirical equation for the determination of L_a is **Equation 2.2**, when laser wavelength of 633 nm was applied [87].

$$L_a(\text{nm}) = \frac{5.8}{R} \quad \text{Equation 2.2}$$

As indicated by **Figure 2.25**, it can be seen that carbonization temperature has great influence on the carbonization degree of the resulted CNFs. Wang *et al.* also noticed that the importance of the duration of carbonization on the resulted CNFs [86]. By using **Equation 2.3**, they claimed that the mole fraction of graphite in the fibres was increased from 0.225 at 600 °C to 0.375 at 1200 °C [86].

$$X_G = \frac{1}{(1+R)} \quad \text{Equation 2.3}$$

Furthermore, they pointed out the highly kinetic nature of carbonization process, which is associated with phase transformation from disordered carbon to graphitic carbon [86]. In the temperature range of 600-1200 °C, they estimated the activation energy, Q_A to be approximately 7360 J/mol by using **Equation 2.4-2.5** [86].

$$X_G = X_0 e^{\left(-\frac{Q_A}{R_{gas}T}\right)} \quad \text{Equation 2.4}$$

$$\ln X_G = \ln X_0 - \frac{Q_A}{R_{gas}T} \quad \text{Equation 2.5}$$

where X_0 is exponential factor, R_{gas} is ideal gas constant and T is temperature in K.

For the CNFs fabricated from the high carbonization temperature, the high level of carbonization degree permits the possibility of using X-ray diffraction (XRD) technique. Zhou *et al.* obtained the value of L_c and $d_{(002)}$ spacing from XRD results for PAN NFs carbonized at 1400-2200 °C. By increasing carbonization temperature within this temperature range, L_c was increased from 1.17 to 4.94 nm, while $d_{(002)}$ was decreased from 3.52 to 3.44 Å [74]. It worth to mention that the $d_{(002)}$ of ideal graphite crystal was reported to be slightly greater than 3.35 Å, as presented in **Figure 2.26** [88]. Having $d_{(002)}$ larger than the one obtained for the graphite, further confirming the turbostratic structure of PAN derived CNFs [49].



Figure 2.26 $d_{(002)}$ spacing comparison among the ideal graphite crystal, pitch derived carbon fibre and PAN derived carbon fibre [88].

It might as well worth to mention that the CNTs fabricated from PAN exhibited skin-core structure [80], as presented in **Figure 2.27**. Having more aligned structure located at skin layer, marking skin layer mainly responsible for the load bearing. This structure is consistent with the

TEM image of PAN derived CNF at carbonization temperature of 1100 °C shown in **Figure 2.22(c)**.



Figure 2.27 Proposed skin-core structure for PAN derived carbon fibre [80].

2.4 Fabrication and Characterisation of carbon Nanofibre Composites

To further enhance the performance of materials towards to the suitable applications, various methods were utilized to achieve the goal. Hou and Reneker fabricated multiwall carbon nanotubes (CNTs) grown on PAN derived CNFs [89], as shown in **Figure 2.28**.



Figure 2.28 TEM image of the iron-catalysed growth of MWCNTs on PAN derived CNFs.

The closer view of single CNF with grown MWCNTs [89].

By adding Fe(acetylacetonate), short in Fe(Acc)₃, into PAN-DMF solution, the smooth electrospun composite fibres were resulted with fibre diameter ranged from 100 to 300 nm [89]. To obtain the carbon composite fibres presented in **Figure 2.28**, the precursor fibres were first stabilised in air at 250 °C for 3h, which was followed by the reduction process from Fe³⁺ to Fe at 500-550 °C in an Ar- H₂ atmosphere (Ar:H₂ = 3:1) for 4h [89]. During this process, the agglomeration of Fe nanoparticles was occurred with agglomeration size of 10-20 nm, mainly located on the surface [89]. Once the nucleation sites were established, the growth of the multiwall CNTs was carried out in a Ar-hexane environment at 700 °C [89]. It was explained that the decomposition of hexane was used as the source of carbon atoms to be absorbed and dissolved in

the metal [89]. These atoms were subsequently transported to the interface region between Fe nanoparticles and the head of the growing CNTs, which were ultimately led to the linear growth of CNTs [89]. In addition, they stated that the length and curvature of the fibre can be controlled by time and carbonization temperature, respectively [89]. Furthermore, they proposed that the resulted materials can be applied in a wide range applications, including high performance filters, composites and electrode materials [89].

Instead embedded the catalysts within the PAN solution, the catalysed CNTs growth can be achieved through a different route. The resulted composite NFs are shown in **Figure 2.29(b)**. Zhao *et al.* used PAN derived CNFs as substrate material, which was then heat treated at 850 °C in an Ar atmosphere while the ferrocene solution in xylene was introduced into the furnace at the same time [90]. By using this method, the catalyst particles was incorporated, as indicated in the inset of **Figure 2.29(b)** [90]. They stated that by growing CNTs on the CNFs the crystallinity of the fibrous materials was effectively increased, indicated by the reduction of *R*-value decreased from 3.98 to 1.68 [90]. Furthermore, they realised that the CNFs with CNTs grown on the surface hugely increased specific capacitance approximately 40 times in cyclic voltammetry (CV) tests [90].



Figure 2.29 (a) SEM image of PAN derived CNFs, and (b) CNTs grown on CNFs. TEM image of the grown CNT is shown in inset [90].

Besides the growth of CNTs on carbon fibrous materials, Lisi *et al.* conducted an experiment on the growth of carbon nanowalls (CNWs) on the carbon fibres by using hot filament chemical vapour deposition (HTCVD) method [91]. By controlling substrate temperature at 700 °C, pressure at 30 mBar, and the total flow of the gas mixture ($\text{CH}_4/\text{H}_2 = 2/100$) at 100 sccm, the resulted CNWs grown on carbon fibres are presented in **Figure 2.30** [91]. Judging by the thickness of the CNWs coating on carbon fibre shown in the inset of **Figure 2.30**, it was suggested that the growth of up to 3 μm CNWs can be achieved within 3 h [91]. In addition, they noticed that the growth of the CNWs on the back of the carbon fibres, which was reported to have thickness of 280 μm [91].



Figure 2.30 (a) Low magnification SEM image of CNWs grown on carbon fibres by HT-CVD; (b) higher magnification SEM image of CNWs grown on carbon fibres. The broken CNWs grown on carbon fibre is inserted as inset [91].

To further enhance the specific area and electrical conductivity, Hsu *et al.* designed a type of carbon composite fibrous materials, which containing CNWs, CNTs, and CNFs [92]. The idea of their engineered composite material is illustrated in **Figure 2.31(a)** [92]. The CNFs used as the substrate material was fabricated from stabilisation and carbonization of electrospun PAN NFs at 280 and 800 °C, respectively [92]. The CNTs growth on CNFs were catalysed with cobalt (III) nitrate in isopropanol [92]. The seasoned CNFs were heat treated in MPECVD chamber with following conditions: the ratio of CH_4 to H_2 was 40/100, processing temperature and the pressure

within the chamber were maintained at 800 °C and 40 Torr for 10 min [92]. To obtain CNWs grown on CNTs, the processing parameter of MPECVD were changed into $\text{CH}_4/\text{H}_2 = 40/100$, temperature of 1500 °C and 40 Torr for 5 min [92]. Indeed, TEM confirmed the formation of CNWs grown on CNTs in **Figure 2.31(b)** [92]. The conductivity measured by impedance for this composite fibrous materials showed 5 times higher than the PAN derived CNFs [92]. In addition, specific area of the composite fibres was 111 m^2/g compared with 10.8 m^2/g obtained for CNFs only [92].



Figure 2.31 (a) Schematic diagram of the distributing condition for CNT and GNWs on the CF; and (b) TEM image of CNW grown on CNT [92].

Apart from the possibility of growing sp^2 carbon species on 1D carbon structure, growing diamond on carbon fibre was also demonstrated [93]. **Figure 2.32** shows the diamond layer grown on VGCF in MPECVD chamber under the following conditions: H_2 of 99.9 sccm, CH_4 of 0.1 sccm, pressure of ~30 Torr, and temperature of 950-1000 °C [93]. The deposition rate at given condition was reported to be 0.1 $\mu\text{m}/\text{h}$ [93]. In fact, Ting and Lake performed the growth of diamond coating two type of carbon fibres, PAN derived carbon fibres and VGCFs [93]. The deposition was impossible on PAN derived CNTs due to severe etching from hydrogen [93]. In contrast, only small reduction on the diameter of VGCFs was noticed after the deposition [93].

Thus they concluded that the more disordered structure exhibited weaker resistance to the hydrogen etching [93].



Figure 2.32 SEM image of a thick layer of diamond coating on the vapour grown carbon fibre deposited for 12h by using MPECVD [93].

Recently, the growth of hydroxyapatite (HA) crystals, the ceramics with similar chemical composition to the human bone was carried out on the PAN derived CNFs, by using stimulated body fluid (SBF) technique [94]. **Figure 2.33** shows the state of the HA-CNFs fibres after the 20 min ultrasonication in ethanol [94]. The grown HA crystals well attached on CNFs implied the good adhesion was developed at the interface region [94]. From the mechanical test results, by increasing CNFs content the fracture strength of this composite reached 67.3 MPa [94]. It was therefore proposed that this material can potentially be used on the bone tissue engineering [94].



Figure 2.33 TEM image of the growth of HA crystals on PAN derived CNFs by using SBF technique [94].

It may come to attention that many common techniques involved in the characterisation of carbon materials are seen as destructive methods. In more recent years, impedance spectroscopy has gained much attention, due to its non-destructive nature and the capability of study both dielectric and semiconductor materials [95-98]. In comparison to conventional electrical measurement conducted under the DC condition, such as I-V curve; impedance measurement relies on the current response by applying excitation of a small-amplitude AC signal between 10^{-4} and $\sim 10^6$ Hz. The impedance is varied with frequency and generally described by using complex number shown in **Equation 2.6**.

$$Z(\omega) = Z' + jZ'' \quad \text{Equation 2.6}$$

where Z' and Z'' represent the real part and imaginary part of $Z(\omega)$, and ω is angular frequency, respectively. In some cases, the resistive contribution is reflected by the real part, whereas the imaginary part represents the capacitive contribution [96]. By plotting Cole-Cole plot with imaginary part against real part, the corresponding conduction mechanism can be deduced based

on the shape of the plot. Su *et al.* reported that the Cole-Cole plot of the un-treated nanodiamond (ND) powders exhibited a near-perfect semicircle, which can be represented by **Figure 2.34(a)** [95]. It was suggested that single semicircle indicated one primary conduction path, and the associated resistance can be determined from the diameter of the semicircle that is intercepted on the real part of the plot [95]. By using fitting procedures, the electrical properties of the un-treated ND powders were represented by a single resistor-capacitor parallel electrical circuit [95]. By applying surface treatment on original ND powders in hydrogen plasma, the shape of the Cole-Cole changed significantly and Warburg diffusion component was noticed in **Figure 2.34(b)** [95]. It was found that the electrical resistance was significantly reduced from 7×10^9 to $2.5 \times 10^5 \Omega$, indicated by the reduced size of the diameter of semicircle in **Figure 2.34(b)** [95]. In addition, the emergence of Warburg component was related to the porous structure of NDs as well as the formation of C-H bonds during the hydrogen treatment. Warburg component is a special case of a constant phase element (CPE), whose n value is equal to 0.5.



Figure 2.34 (a) Un-treated ND powders, (b) the ND powders after the hydrogen plasma treatment [95].

The impedance of common electrical components is summarized in **Table 2.2**. Besides CPE can equivalent to Warburg component when $n = 0.5$, CPE is also equivalent to ideal resistor, ideal inductor and ideal capacitor when n is equal to 0, 1, and -1, respectively. As presented in **Table**

2.2, the impedance of a pure resistor is not dependent on the frequency, thus, the impedance of resistor does not have imaginary part. On the contrary, the impedance of capacitor and inductor are influenced by frequency, the impedance of these two electronic components therefore contains imaginary part.

Table 2.2 Impedance of various electrical circuit elements.

Electrical circuit element	Description	Impedance
R	Resistance	R
C	Capacitance	$1/j\omega C$
L	Inductance	$j\omega L$
W	Semi-infinite Warburg	$1/Y_0\sqrt{j\omega}$
CPE	Constant Phase Element	$Y_0(j\omega)^n$

The impedance measurement is not only applied to the materials with powder form, but also can be used to investigate conduction mechanism of composite materials with various electrical conductive portion within the matrix materials. Wang *et al.* successfully employed impedance measurement in the investigation of conductive network of high density polyethylene (HDPE)/carbon black (CB) with varied carbon black concentration [98]. It was found that with increasing CB concentration from 15 to 19 wt%, the magnitude of resistances and capacitance was decreased, and inductance was merged in the case of 19 wt%. With further increasing CB to 25 wt%, the further reduction on the resistance magnitude was found associated with the disappearance of capacitance [98]. They also attributed the change of electrical components extracted from Cole-Cole plots to the change of CB aggregates within the HDPE [98].

2.5 Aim and Objectives

Given by many desirable properties of carbon nanofibres and its associated carbon materials, it is crucial to be able to tailor the suitable structure and properties, hence to maximize the performance of the material in the intended applications. Therefore, the aim of the thesis was to study the synthesis and characterisation of carbon nanomaterials derived from various fabrication methods. As introduced in the previous sections, the characterisation of carbon fibres was either restricted by the examining technique either with limited penetration depth, or associated with complex sample preparation and operation procedures. Furthermore, the characterisation technique to study the carbon material in some occasions was considered to be destructive. Therefore it is essential to develop a method to examine the carbon fibre non-destructively, while the information was not restricted to the surface only. Thanks to the small diameter of the carbon nanofibres, such material was thought to be a good candidate using as the supercapacitor materials, due to the large specific area, as well as good electrical conductivity. To further enhance the supercapacitor performance of the carbon nanofibres, both desirable features of carbon nanofibres can be improved by growing other carbon species on its surface [92]. From the viewpoint of cost and simplicity of the fabrication method, it was always desirable to develop a method with greater flexibility, and simpler procedures. In this regard, there were seven objectives, in order to achieve the aim of the project.

- 1) To systematically study the effect of four parameters of electrospinning, voltage, TCD, Q and C on the morphology of the resulted PAN products under the different parameter settings.
- 2) To determine the optimized processing parameters in order to produce bead-free carbon nanofibres with good reproducibility and long stability. Therefore, the thick sample can be prepared by using such parameter for the preparation of substrate material for the later chapters.

- 3) To fabricate carbon nanofibres by carbonizing the electrospun PAN fibres derived from the optimized processing parameters at different carbonization temperatures, ranging from 500 to 1000 °C.
- 4) To investigate the effect of carbonization temperature on the morphology, functional groups, chemical structure, crystallinity and electrical properties of CNFs.
- 5) To correlate the microstructure evolution induced by increasing carbonization temperature with the change of electrical properties of CNFs.
- 6) To fabricate CNWs-CNFs hybrid material directly from the stabilized PAN NFs by using MPECVD technique.
- 7) To investigate the morphology, functional groups, and chemical structure of CNWs-CNFs hybrid materials in comparison to conventionally carbonized PAN NFs by using SEM, FTIR, and Raman.
- 8) To initiate the initial work for CNWs-CNFs hybrid materials to be used as supercapacitor material, by using CV test and charge-discharge measurement to characterise the electrochemical properties of the hybrid materials, respectively.

3 Experimental Procedures and Characterization Techniques

3.1 Experimental Procedures

In this project, there were three main sets of experiment involved. Started with the electrospinning of PAN NFs, then carbonization of PAN NFs, and finally followed with the fabrication of CNFs-CNWs hybrid materials. By following same sequence of the experiments, the detailed information regarding to the synthesis of above mentioned materials were separately presented in the following subsections from 3.1.1 to 3.1.3.

3.1.1 Electrospinning of PAN NFs

To enable PAN NFs produced by electrospinning technique, the PAN solution was required to obtain before the fibreization process. As depicted in **Figure 3.1**, dimethylformamide (DMF) solvent was added into a predetermined amount of PAN powders with molecular weight (M_w) of 150000. Both chemicals were respectively purchased from Scientific Polymer Products and Fisher Scientific and used directly without any purification. The mixture was then subjected to 2 h ultrasonication (ultrasonic processor: Hielscher UP 400S), in order to yield homogenous PAN solution with targeted concentration, C . By using the method described as above and is shown in **Figure 3.1**, a series of PAN solution with various concentrations, ranging from 2 to 16 wt% were produced, and are presented in **Figure 3.2**.

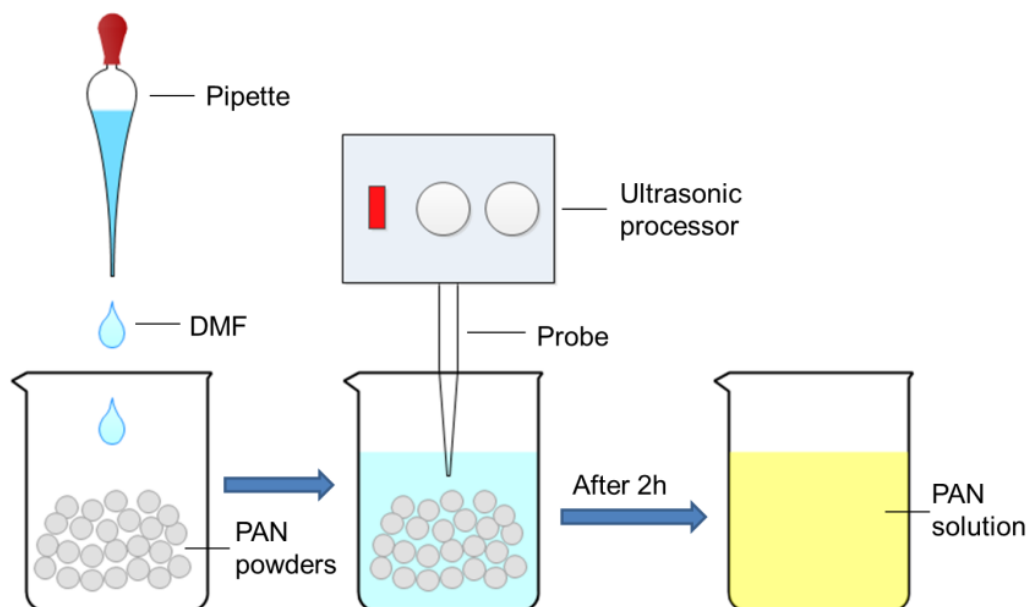


Figure 3.1 Schematic diagram of showing the preparation of PAN solution.

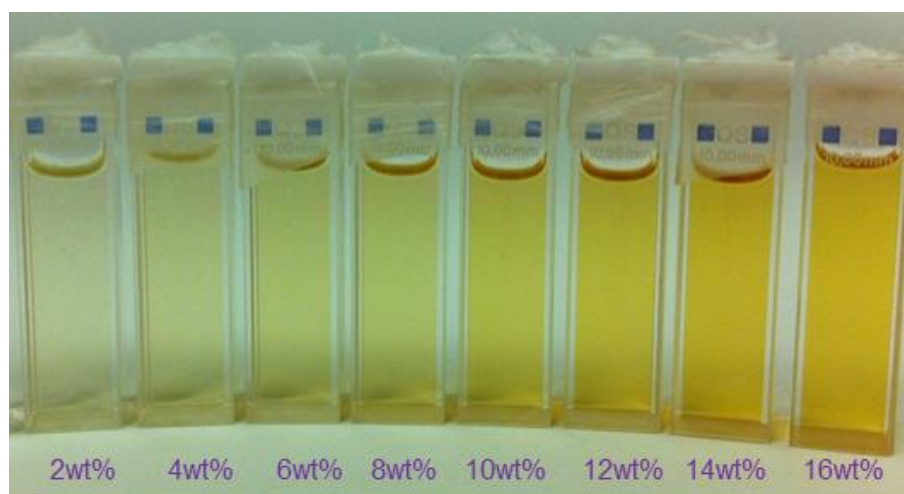


Figure 3.2 Photograph of a series of PAN solutions with various concentrations, ranging from 2% to 16%.

Once the PAN solution with targeted concentration was ready, it was transferred into a plastic syringe, in which the solution flow rate, Q was controlled by the syringe pump (NE-300 “Just Fusion” TM). To continuously produce ultrathin fibres from selected PAN solution, the whole process of electrospinning was constantly driven by an electrical field difference within the given

suitable needle tip to collector distance. To induce the electrical field, the metallic needle connected to the syringe via a plastic tubing was also connected to a high positive voltage supply (Genvolt), while the aluminium (Al) foil collector which was grounded to earth electrode. These forms the home-built electrospinning setup used in Aston University, as illustrated in **Figure 3.3**. To assure the accuracy of the deposition time, the fibre ejection at the Taylor cone was constantly monitored by the camera (Olympus 3.0, GXCAM-3). Due to the simple configuration of the electrospinning setup used in this project, all the PAN fibres collected on the collector were non-woven type. To be able to control the morphology and the size of the resulted PAN materials, four types of the parameters were selected under the investigation. They were processing parameters, and solution parameter. The processing parameters included voltage, tip-to-collector distance (TCD) and Q , whereas the solution parameter was referred to PAN solution concentration.

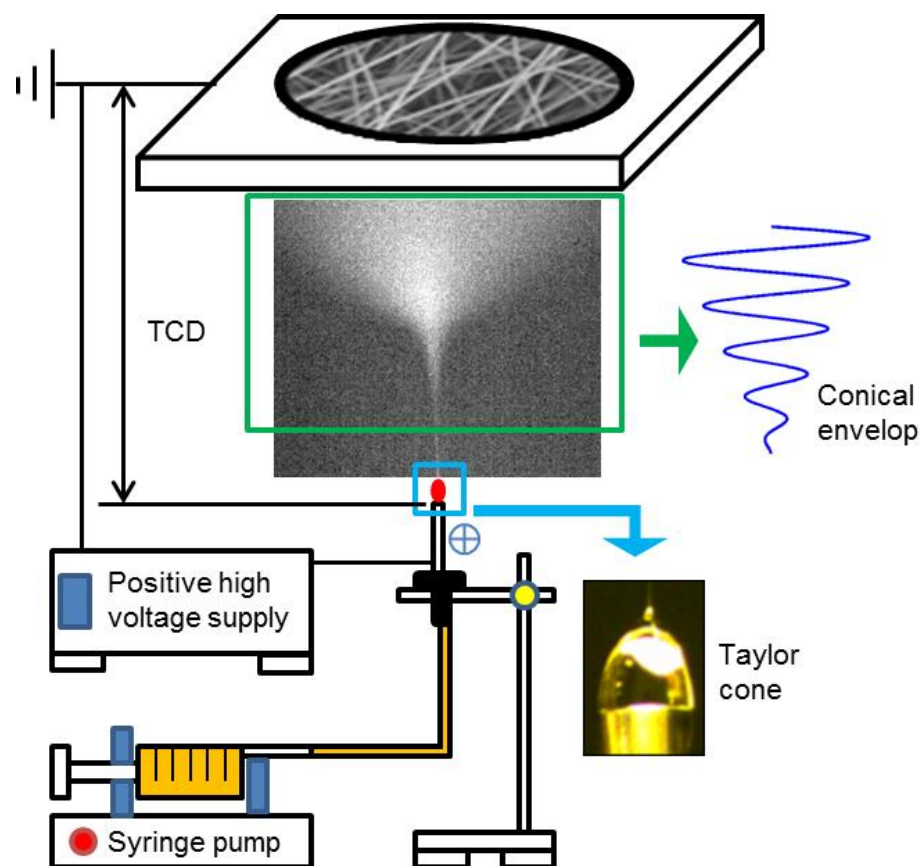


Figure 3.3 Schematic diagram of electrospinning setup used in Aston University.

In order to gain the understanding on the effect of individual parameter, several groups of samples were prepared and their corresponding parameters are summarized in **Table 3.1** to **Table 3.4**. After the optimized processing parameters were obtained, the reproducibility and long stability of the parameters used for the fabrication of Q-8 and Q-9 in **Table 3.3** with long deposition time of 70 and 120 min were attempted. These two samples were renamed as D-1 and D-2, respectively.

Table 3.1 Matrix of processing parameters with various voltages.

Sample	Voltage (kV)	TCD (cm)	Q (ml/h)	EFS (kV/cm)	Taylor cone
V-1	0	15	1.5	0	No
V-2	5	15	1.5	0.33	No
V-3	10	15	1.5	0.67	Discontinued
V-4	15	15	1.5	1	Discontinued
V-5	20	15	1.5	1.67	Stable
V-6	25	15	1.5	2	Unstable
V-7	30	15	1.5	1.07	Unstable
V-8	16	15	1.5	1.13	Stable
V-9	17	15	1.5	1.2	Stable
V-10	18	15	1.5	1.27	Stable
V-11	19	15	1.5	1.33	Stable

Table 3.2 Matrix of processing parameters with various TCD.

Sample	TCD (cm)	Voltage (kV)	Q (ml/h)	EFS (kV/cm)	Taylor cone
T-1	5	16	1.5	3.2	Unstable
T-2	10	16	1.5	1.6	Stable
T-3	15	16	1.5	1.07	Stable
T-4	20	16	1.5	0.8	Stable
T-5	25	16	1.5	0.64	Very faint
T-6	30	16	1.5	0.53	Very faint
T-7	11	16	1.5	1.45	Stable
T-8	12	16	1.5	1.33	Stable
T-9	13	16	1.5	1.23	Stable
T-10	14	16	1.5	1.14	Stable

Table 3.3 Matrix of processing parameters with various Q.

Sample	Q (ml/h)	Voltage (kV)	TCD (cm)	Time (min)	Taylor cone
Q-1	0.5	16	10	2	Unstable
Q-2	1	16	10	2	Stable
Q-3	1.5	16	10	2	Stable
Q-4	2	16	10	2	Stable
Q-5	2.5	16	10	2	Stable
Q-6	3	16	10	2	Multi-jet
Q-7	0.5	16	14	2	Unstable
Q-8	1	16	14	2	Stable
Q-9	1.5	16	14	2	Stable
Q-10	2	16	14	2	Stable
Q-11	2.5	16	14	2	Stable
Q-12	3	16	14	2	Stable

Table 3.4 Matrix of optimized processing parameters with various PAN solution concentrations from 2 to 16%.

Sample	C (%)	Expected deposition time (min)	Actual deposition time (min)
C-1	2	2	2
C-2	4	2	2
C-3	6	2	2
C-4	8	2	2
C-5	10	2	2
C-6	12	2	2
C-7	14	2	2
C-8	16	2	2
C-9	2	10	10
C-10	4	10	10
C-11	6	10	10
C-12	8	10	10
C-13	10	10	10
C-14	12	10	10
C-15	14	10	10
C-16	16	10	8.5

3.1.2 Synthesis of CNFs

Given to the nature of PAN, the synthesis of CNFs from PAN NFs required two-step heat treatments. One of which was to heat treat PAN NFs at stabilisation temperature, $T_{\text{stabilisation}}$ in air, whereas the other one was the subsequent heat treatment which was carried out in an inert atmosphere. The benefits of applying stabilisation process first were to enhance the carbon yielding and to form a ladder structure, which gives a good heat resistance. Hence, avoiding the melting and fusing of the fibres at higher temperature in the subsequent carbonization process. Electrospun 14% PAN NFs fabricated with processing parameters of 16kV, 14cm, and 1.5 ml/h was selected to be converted into CNFs. The selected PAN NFs was heated at 280 °C for 1h with the presence of air in the square furnace (Carbolite, Sheffield, UK). After the stabilisation process, the colour of the PAN NFs was changed from white to dark brown, as shown in **Figure 3.4**.

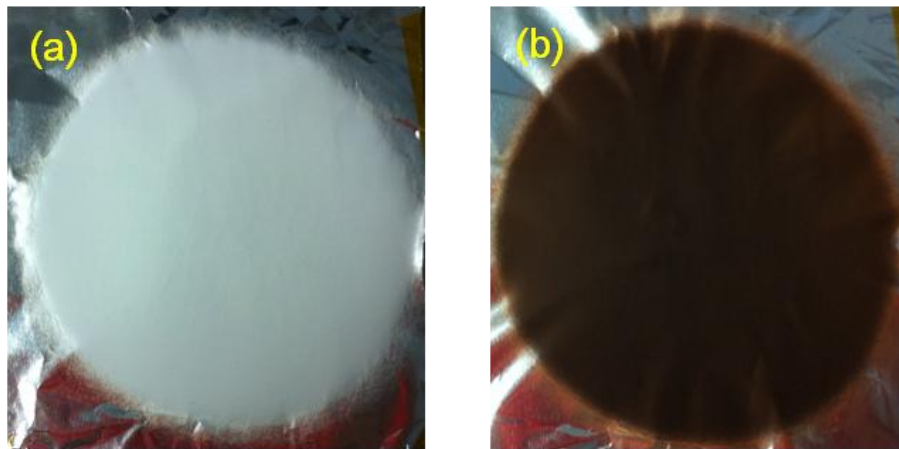


Figure 3.4 Comparison between the electrospun PAN NFs (a) before oxidative stabilisation, and (b) after oxidative stabilisation in air.

The stabilised PAN NFs were cut into small squares with dimension of approximately of $1 \times 1 \text{ cm}^2$ and each small square was subsequently subjected to the carbonization process at different carbonization temperatures, $T_{\text{carbonization}}$ ranging from 500 to 1000 °C. The carbonization process was taken place in the tube furnace (Carbolite, Sheffield, UK) with heat rate of 10 °C/min in a N_2

atmosphere. The holding time for the targeted $T_{\text{carbonization}}$ was 1h and then followed with a furnace cooling process. For the simplicity, the electrospun PAN NFs and stabilized PAN NFs were named as PAN and SPAN, respectively. Whereas the stabilised PAN NFs carbonized at 500, 600, 700, 800, 900, and 1000 °C were named as CNF-500, CNF-600, CNF-700, CNF-800, CNF-900 and CNF-1000, as summarized in **Table 3.5**.

Table 3.5 Experimental conditions of PAN NFs with various treatments.

Sample	Condition	$T_{\text{carbonization}}$ (°C)
PAN	Electrospun PAN NFs	N/A
SPAN	Stabilised PAN NFs	N/A
CNF-500	Carbonization of stabilised PAN NFs	500
CNF-600	Carbonization of stabilised PAN NFs	600
CNF-700	Carbonization of stabilised PAN NFs	700
CNF-800	Carbonization of stabilised PAN NFs	800
CNF-900	Carbonization of stabilised PAN NFs	900
CNF-1000	Carbonization of stabilised PAN NFs	1000

3.1.3 Synthesis of CNWs-CNFs Hybrid Materials

To avoid the unnecessary melting of PAN NFs, the stabilised PAN NFs were used as precursor for the fabrication of CNWs-CNFs hybrid materials, by using microwave plasma enhanced chemical vapour deposition (MPECVD) technique. The image of ASTeX5010 MPECVD system is shown in **Figure 3.5**.



Figure 3.5 Photograph of ASTeX5010 MPECVD system: (a) assembly of main components; and (b) plasma ball glows in the reactor chamber during the deposition process [99].

In the reactor chamber, the hydrogen plasma was ignited at the following conditions: H₂ flow rate of 90 standard cubic centimetre per minute (sccm), microwave power of 800W and gas pressure of 10 Torr. Once the stable H₂ plasma ball was established in the chamber, CH₄ gas with flow rate of 10 sccm was introduced into the reactor chamber to form CH₄/H₂ mixture. The selected precursor was treated in CH₄/H₂ atmosphere for 30 min with pressure of 40 Torr. The general condition in the MPECVD chamber during the synthesis of CNWs-CNFs hybrid materials is illustrated in **Figure 3.6** and summarized in **Table 3.6**. As indicated in **Figure 3.6**, the top layers of the stabilized PAN NFs piece became a bright orange-red colour. To explore the unique impact brought by MPECVD on the stabilized PAN NFs, the same precursor was heat treated by using a conventional tube furnace from room temperature to carbonization temperature of 910 °C in a N₂ atmosphere. During the conventional carbonization process, the heating rate and holding time were controlled at 20 °C/min and 30min, respectively. The reason for choosing 910 °C this particular temperature was consulted with Mr Vojtěch Kunderát, who conducted a series of temperature calibration work within the MPECVD chamber. It was estimated that the temperature in the MPECVD chamber at given condition in **Table 3.6** was approximately 910 °C.

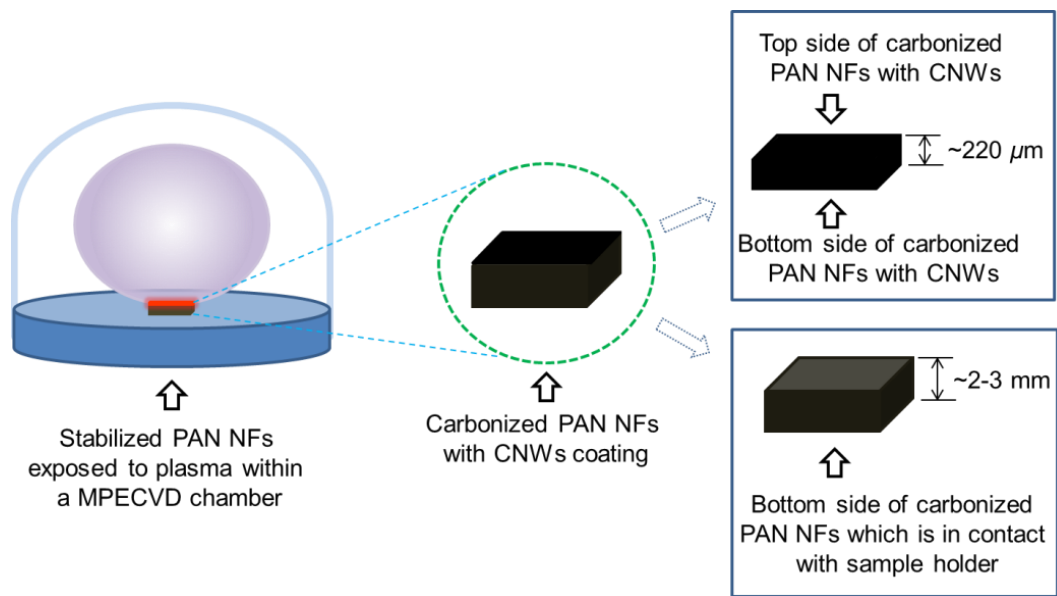


Figure 3.6 Sample preparations for carbonized PAN NFs with CNWs coating after MPECVD process.

Table 3.6 Experimental conditions for PAN NFs with different treatments.

Sample	Description	Conditions
S-1	Electrospun PAN NFs	14.5%, 16 kV, 14cm, 1.5ml/h for 5h
S-2	Stabilized PAN NFs	Heating at 280 °C for 1h in air
S-3	Furnace carbonized PAN NFs	Heating to 910 °C with heating rate of 20 °C/min and holding time of 30min in N ₂
S-4	MPECVD carbonized PAN NFs	Microwave power of 800W, and pressure of 40 torr in a CH ₄ /H ₂ environment for 30min with flow rate of CH ₄ and H ₂ at 10 and 90 sccm
S-5	MPECVD grown CNWs on the surface layers of the CNFs	
S-6	MPECVD grown CNWs on the deeper layers of the CNFs	

3.2 Characterisation Techniques

The experimental parameters for each characterisation technique in addition to the electrochemical characterisations in section 3.2.6 used in this project along with the description of data process, which were included at the end of corresponding subsection.

3.2.1 Scanning Electron Microscopy

Scanning electron microscopy (SEM) is an indispensable technique for modern science researches across numerous fields. Because it is not only able to acquire the morphological information at surface, near surface, or even the bulk structure; but also can provide the information regarding to the chemical composition and electrical conductivity of the examined object [100]. A simplified illustration of SEM is presented in **Figure 3.7**.

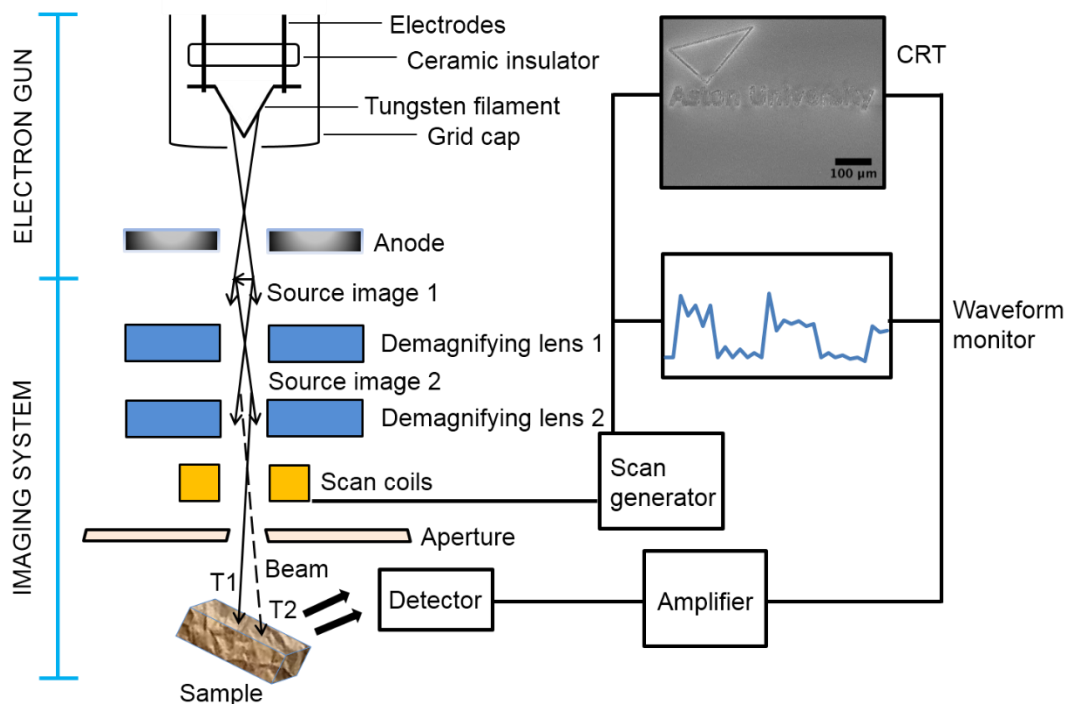


Figure 3.7 Schematic diagram of SEM with basic components.

In the current project, the morphology of all fabricated samples were characterized by SEM (JEOL, JSM-700F) using secondary electron signals. All electrospun PAN samples described in section 3.1.1 and stabilised PAN samples were gold coated using sputter coater (emscope, SC 500) before imaging by SEM. Each characterizing piece was cut out from the centre area of the electrospun non-woven mat (see **Figure 3.4**) with dimension of approximately $1 \times 1 \text{ cm}^2$. As the fibre diameter was one of the most important criterion used to quantify the quality of the fibres synthesized from the different experimental conditions, the quantitative study based on the SEM images of each synthesized sample was carried out by using software Image-J. In order to provide the reliable result on the fibre diameter, the average diameter (d_a) of each sample from its corresponding SEM images was obtained by counting 100 fibre diameters, as expressed by **Equation 3.1**. To ensure the accuracy of the fibre diameter, the standard deviation (d_{SD}) was also calculated by using **Equation 3.2**. Other quantitative data was also extracted from the SEM image of the electrospun PAN fibres, including total deposition area of electrospun PAN NFs per SEM image, A_d ; total deposition area of beads per SEM image, A_b , ratio of deposited area to the total SEM image area, F_A ; ratio of deposited bead area to the total SEM image area, F_b .

$$d_a = \sum_{i=1}^N d_i / N \quad \text{Equation 3.1}$$

$$d_{SD} = \frac{1}{N} \sum_{i=1}^N (d_i - d_a)^2 \quad \text{Equation 3.2}$$

where N represents the counting time which is 100.

3.2.2 Transmission Electron Microscopy

Transmission electron microscopy (TEM) is an advanced characterisation technique, which is used to study the morphology, crystallographic structure (i.e. internal structure) and chemical composition of materials by transmitting electron beam through the examined sample. The thickness of the sample is examined by TEM needs to be extremely thin, preferably, 100-200 nm. The results of carbonized PAN NFs presented in section 5.4 were characterized by using TEM (JOEL, JEM 2100). The CNFs were cut into small pieces and then were ultrasonicated in ethanol for 5 min. One drop of suspension which contain CNFs was transferred to the copper grid with glassy carbon coating on and later dried in air. TEM images were obtained under the accelerating voltage of electron beam at 200 keV. The size of electron beam to obtain SAED patterns was controlled at a few micrometres.

3.2.3 Fourier Transform Infrared Spectroscopy

In the current project, the functional groups of electrospun PAN NFs with various treatments were examined by using FTIR Thermo Scientific Nicolet iS5, as shown in **Figure 3.8**. The dimension of the sample was approximately 1 x 1 cm². Each sample, two random positions were chosen. The software used to collect FTIR data was OMNIC. The FTIR measurement was conducted at attenuated total reflectance (ATR) mode. The obtained FTIR spectrum shows the relationship between transmittance and wavenumber, while the wavenumber was selected as a full range from 4000 to 550 cm⁻¹. The resolution of each spectrum was 4 cm⁻¹ and the number of scan for each sample was 16.



Figure 3.8 FTIR machine with model name of Nicolet iS5 used in Aston University.

3.2.4 Raman Spectroscopy

The chemical structure of PAN NFs with various treatments was explored by Raman spectroscopy (Renishaw inVia Raman Microscope), as shown in **Figure 3.9**. The wavelength of the excitation laser was 633 nm and the Raman spectra were collected by using software Wire 3.1. To ensure the accuracy of the Raman results, at least 3-4 different locations of each carbonized sample were randomly selected by using the integrated optical microscope with magnification lens of $\times 20$. For each location, the exposure time was 10 s and accumulation was 10 while the laser power was 10 mW. The sample with dimension of approximately $1 \times 1 \text{ cm}^2$ was placed on a glass slide, which was held by sample stage shown in **Figure 3.9(b)** during the Raman measurements.

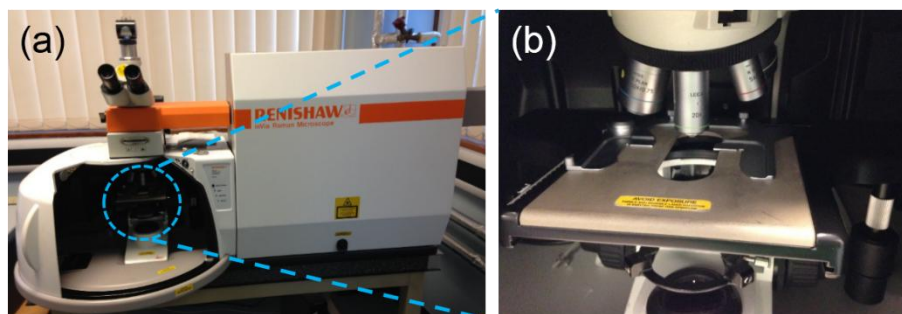


Figure 3.9 Renishaw Raman spectroscopy in University of Birmingham: (a) the overview of the technique; (b) the sample stage for optical focusing with different magnifications.

The main focus of using Raman in the current project was to extract R -value (i.e. intensity ratio of D peak to G peak) and understand the graphitization degree and the size of graphitic crystallites. Peak deconvolution of D and G peak was carried out by fitting with Gaussian–Lorentzian mixed shape via software OriginPro 9.0, according to reference [86]. The R -value calculated for each sample was the average value obtained from different locations of the sample. The estimation of L_a was obtained by using **Equation 2.2**. The mole fraction of graphite, X_G was obtained by using **Equation 2.3**. The activation energy for the growth of graphitic crystallites with increasing carbonization temperature was calculated by using **Equation 2.4** and **Equation 2.5**.

3.2.5 Impedance Spectroscopy

Impedance spectroscopy (IS) is a powerful tool that used to characterize the electrical properties of materials, and the interfaces between the materials and electronically conducting electrodes. In the current project, impedance measurement of CNFs was carried out by using Autolab electrochemical system (Windsor Scientific, PGSTAT 302N), which is shown in **Figure 3.10**. All the electrical measurements presented in Chapter 5 were conducted in air using the testing cell as depicted in **Figure 3.11**. The impedance data was collected over a frequency range from 10^6 to 10^2 Hz.



Figure 3.10 Electrochemical system in Nanoscience group of Aston University.

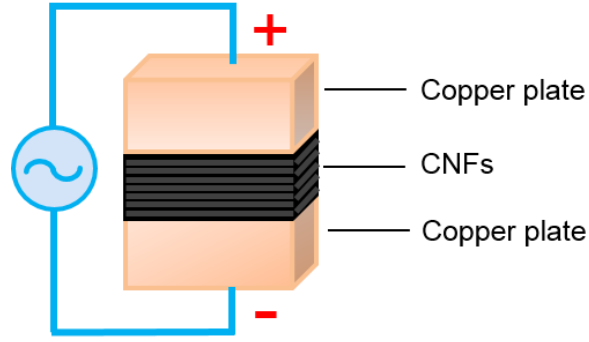


Figure 3.11 Schematic diagram of testing cell for CNFs during the impedance measurement.

The Cole-Cole plot of the CNFs carbonized with carbonization temperature from 500 to 800 °C were recorded by impedance spectroscopy. The other two samples with higher carbonization exceed the measuring limit of the current experimental setup. The fitting curves in the section 5.5 for sample CNF-500 to CNF-800 were generated by using following Equations from 3.1 to 3.4.

$$Z(\omega) = R_s + \frac{1}{\frac{1}{R_p} + j\omega C} \quad \text{Equation 3.1}$$

$$Z(\omega) = R_s + \frac{1}{\frac{1}{R_p} + Q(j\omega)^n} \quad \text{Equation 3.2}$$

$$Z(\omega) = R_s + \frac{1}{\frac{1}{Q(j\omega)^n + j\omega L} + \frac{1}{R_p}} \quad \text{Equation 3.3}$$

$$Z(\omega) = R_s + \frac{1}{\frac{1}{R_p} + j\omega L} \quad \text{Equation 3.4}$$

where R_s is contact resistance between PAN derived CNFs and copper electrodes, and R_p is parallel resistance.

3.2.6 Electrochemical Characterisations

To evaluate the supercapacitor performance of CNFs produced from conventional furnace and CNWs-CNFs fabricated with MPECVD, the electrochemical characterisations were carried out by using a standard three-electrode configuration in 0.5M H₂SO₄ solution, as illustrated in **Figure 3.12**.

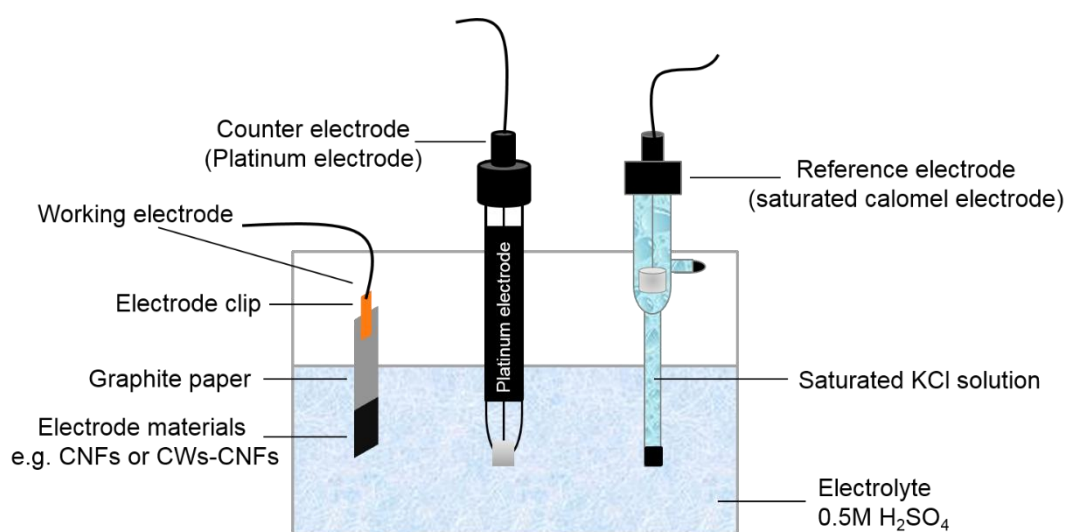


Figure 3.12 Schematic diagram of a standard 3 electrode configuration applied during the electrochemical measurements of CNFs and CNWs-CNFs.

The configuration was composed of a working electrode, a platinum electrode used as counter electrode, and a saturated calomel electrode used as reference electrode, respectively. The working electrode was assembled by combining electrode clip, graphite paper and electrode materials in such fashion. To ensure the good precision of the measurement, the electrode materials and the graphite paper was carefully prepared by using following procedures. The graphite paper was first cleaned by wiping the surface with ethanol. The cleaned graphite paper was cut into dimension of 5 × 1.5 cm², and further cleaned by immersing into the ethanol for hours and dried in the oven at 60 °C. The mass of the dried clean graphite paper was measured by the microbalance, so that the weight of the electrode materials can be deduced in the later step. To

provide a good adhesion between the electrode materials and the prepared graphite paper, the binder was made by dissolving predetermined amount of PVDF into N-methylpyrrolidinone (NMP) solvent to yield a binder solution concentration of 2.5%. The electrode materials, conductive carbon black (super K) and binder was mixed in the mass ratio of 8:1:1. The mixture was then further stirred by using magnetic stirrer to achieve good homogeneity. The homogeneous mixture was later applied on the graphite paper to generate electrode material area of $1 \times 1.5 \text{ cm}^2$. The graphite paper was then dried in vacuum oven at $120 \text{ }^\circ\text{C}$ for 12 h. The dried graphite paper was then measured again by microbalance, so that the mass of the electrode materials can be obtained.

Two different tests carried out for electrochemical characterizations were cyclic voltammetry (CV), and charge-discharge, respectively. The CV was conducted by using PARSTAT2273 electrochemical working station (Princeton Applied Research, USA), whereas the charge-discharge measurement was performed on Land CT2001A battery testing system. The experimental voltage range used for all electrochemical measurements was 0-0.9V.

4 Electrospinning of PAN NFs

4.1 Optimization of Processing Parameters at PAN Solution Concentration of 12%

The optimization process was carried out by varying three processing parameters, voltage, tip to collector distance (TCD), and flow rate (Q), while the PAN solution concentration was fixed at 12%. The goal for this section was to obtain bead free fibres with smallest diameter, while the deposition area A_d per SEM image was high. In addition, the long stability and high reproducibility of the optimized processing parameter were also assessed.

4.1.1 Voltage

As discussed in Chapter 2, the fibre ejection was initiated from the tip of the Taylor cone. Therefore, the status of the solution drop attached to the needle tip was monitored. **Figure 4.1** shows the solution drop change in the voltage range from 0 to 30 kV with each increment of 5kV, while TCD and Q were fixed at 15 cm and 1.5 mL/h, respectively. In the voltage range from 0 to 5 kV, the solution drop was remained in a hemispherical shape sitting on the needle tip in **Figure 4.1(a)**. No significant disturbance on the solution drop was observed from the induced electrical field, defined as the ratio of voltage to TCD. As voltage increased to 10-15 kV, the shape of solution drop started to transform from hemispherical into conical. In **Figure 4.1(b)-(c)**, a very faint fibre jet was seen to eject from the tip of the Taylor cone. However, the fibre ejection was ceased within 2 min without disabling the induced electrical field. In contrast, a continuous fibre ejection was found in the higher voltage range from 20 to 30 kV. Taylor cones were found constantly on in **Figure 4.1(d)-(f)**, and no fibre ejection ceased as observed in **Figure 4.1(b)-(c)**, when the electrical field was applied. Interestingly, it can be seen that the elongation of the solution drop along the needle axis was more pronounced with increasing voltage, because of the

larger electrical field was induced within the constant TCD. It should be mentioned that, the stability of the solution drop started to deteriorate quickly when the voltage increased to very high values, 25 and 30 kV in **Figure 4.1(e)-(f)**. When the electrospinning system experienced high instability, the volume of the solution drop on the needle tip was changing constantly.

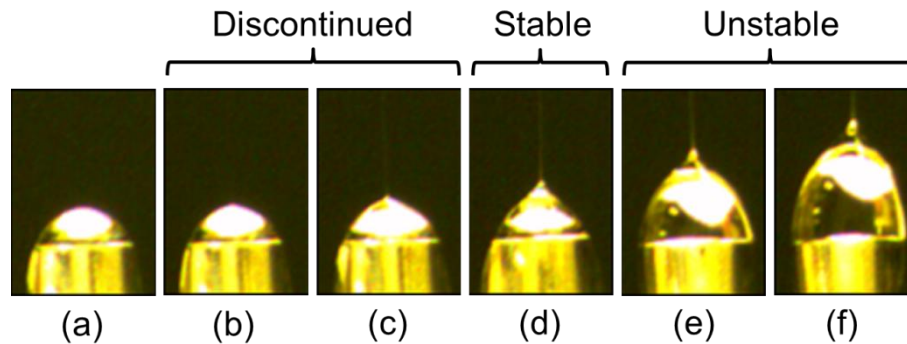


Figure 4.1 Optical images of solution drop formed at the needle tip as a function of voltage: (a) 0-5 kV, (b) 10 kV, (c) 15 kV, (d) 20 kV, (e) 25 kV, and (f) 30 kV.

As no modification on the Al foil collector was made, the resulted PAN NFs was expected to be collected as non-woven mats. Under the influence of different voltage from 0 to 30 kV, the images of the resulted fibre mats with dimension information are presented in **Figure 4.2**. Consistent with the observation seen in **Figure 4.1(a)**, by applying voltage of 0-5 kV no deposition was resulted, as shown in **Figure 4.2**. While the voltage was increased to 10-15kV, the fibre ejection was ceased, hence shorter deposition time. This in turns led to the formation of smaller fibre mats with much less fibres, when compared with the ones deposited with continuous fibre ejection in the higher voltage range. In the continuous fibre ejection region, it can be seen that the size of the fibre mat was decreased with increasing voltage from 20 to 30 kV, while the thickness of the mat was increased.

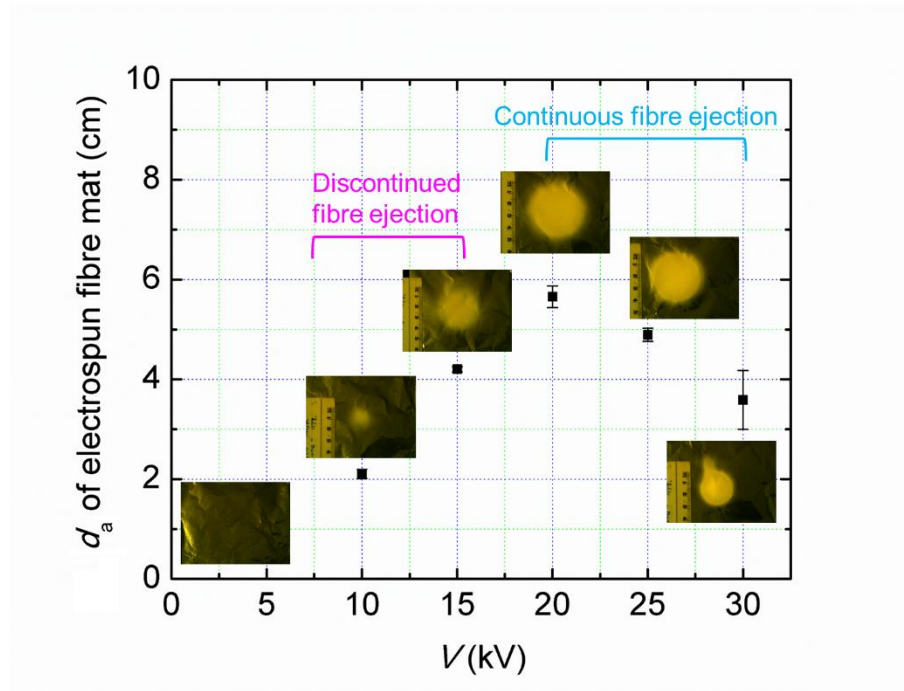


Figure 4.2 Quantitative plot of d_a of electrospun PAN fibre mat as a function of voltage from 10 to 30 kV. The photos of electrospun PAN fibre mats are inserted.

Morphology is a particular important characteristic for electrospun NFs, as it greatly affects the performance of nanomaterials in their applications [89, 90, 92, 101]. **Figure 4.3** shows the morphology of electrospun PAN NFs deposited on Al foil collector with increasing voltage from 0 to 30 kV. It is not surprised that only the bare Al foil can be seen in **Figure 4.3(a)** in the voltage range from 0 to 5 kV. In the discontinued fibre ejection region, beaded fibres observed in **Figure 4.3(b)** with voltage of 10 kV, whereas the much smoother fibres were deposited at voltage of 15 kV shown in **Figure 4.3(c)**. All the fibres deposited in the continuous fibre ejection region exhibited beaded morphology, which are presented in **Figure 4.3(d)-(f)**. Some quantitative information extracted from SEM images of **Figure 4.3** are listed in **Table 4.1**.

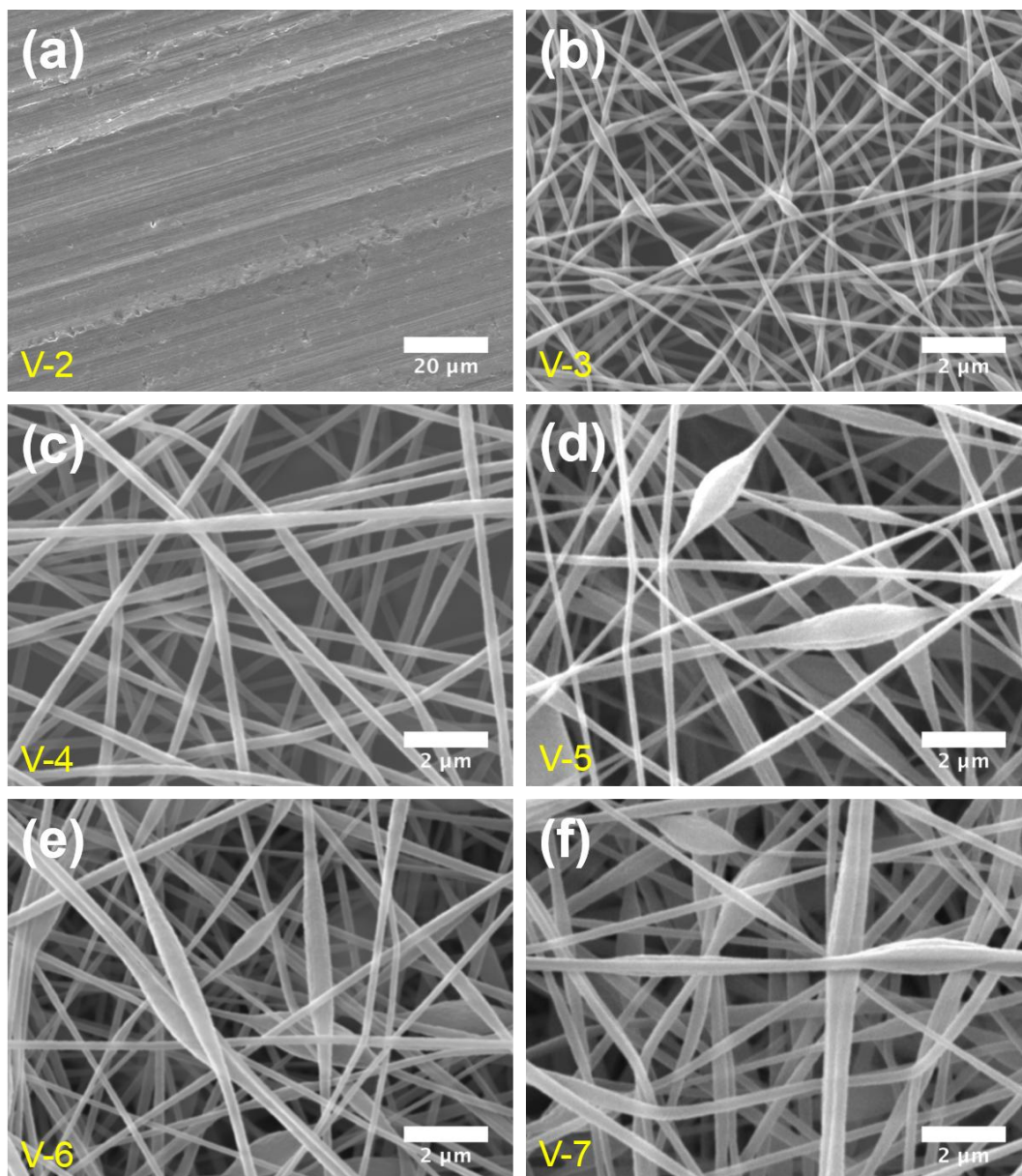


Figure 4.3 SEM images of electrospun PAN NFs deposited on Al collector at various voltages: (a) 5 kV, (b) 10 kV, (c) 15 kV, (d) 20 kV, (e) 25 kV, and (f) 30 kV.

Table 4.1 Quantitative data extracted from SEM images of PAN NFs in the voltage range from 10 to 30 kV.

Sample	Voltage (kV)	d_a (nm)	A_d (μm^2)	F_A	A_b (μm^2)	F_b
V-3	10	131 \pm 23	78.87	0.73	11.40	0.11
V-4	15	234 \pm 31	85.35	0.79	-	-
V-5	20	195 \pm 47	90.79	0.84	30.90	0.28
V-6	25	211 \pm 43	96.45	0.89	18.81	0.17
V-7	30	252 \pm 50	100.97	0.93	15.06	0.14

To determine the voltage which yields smooth fibre but is also associated with a continuous fibre ejection, the voltage range from 16 and 19 kV was selected with the narrower increment of 1 kV each time. The solution drop change in the voltage range from 16 to 19 kV is shown in **Figure 4.4**. As expected, the continuous fibre ejection from Taylor cone with reasonably good stability was observed in this new voltage range.

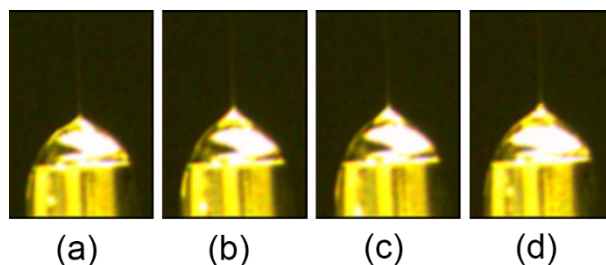


Figure 4.4 Optical images of solution drop formed at the needle tip as a function of voltage: (a) 16kV, (b) 17 kV, (c) 18 kV, and (d) 19 kV.

Under the influence of different voltage from 16 to 19 kV, the images of the resulted fibre mats with dimension information are presented in **Figure 4.5**. It can be seen that the smallest fibre mat was obtained at voltage of 16 kV, by increasing to the higher voltages from 17 to 19 kV, the size of the fibre mats was increased but no significant variations found amongst these three higher voltage values.

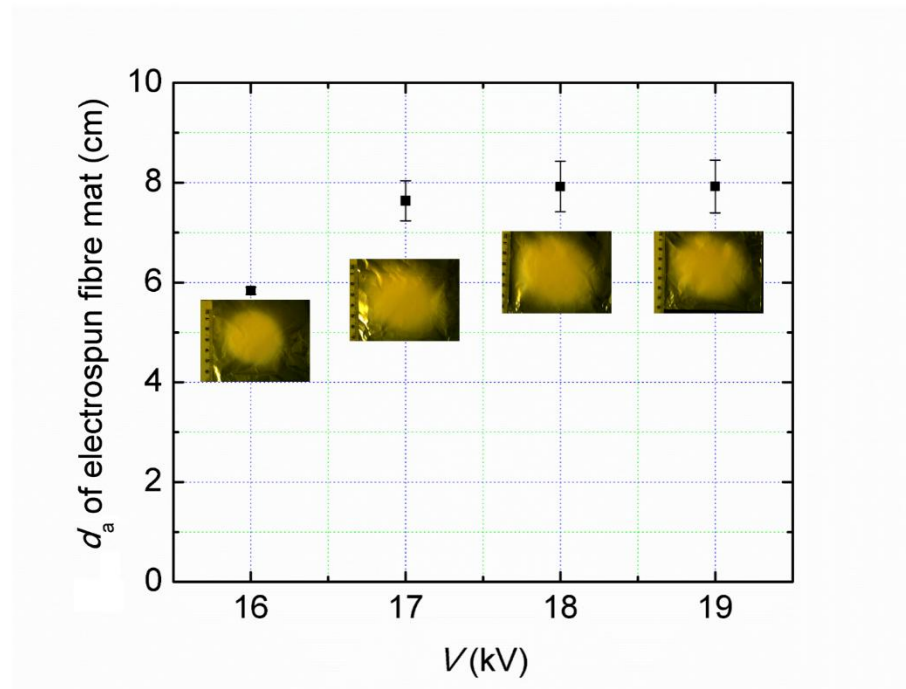


Figure 4.5 Quantitative plot of d_a of electrospun fibre mat as a function of voltage of 16-19 kV. The photos of electrospun PAN fibre mats are inserted.

Figure 4.6 shows the morphology of electrospun PAN NFs deposited on Al foil collector with increasing voltage from 16 to 19 kV. In **Figure 4.6(a)**, smooth fibres with high uniformity was observed at voltage of 16 kV. With further increasing voltage to higher values, only beaded fibres were found in **Figure 4.6(b)-(d)**. The quantitative information extracted from SEM images of **Figure 4.6** are listed in **Table 4.2**.

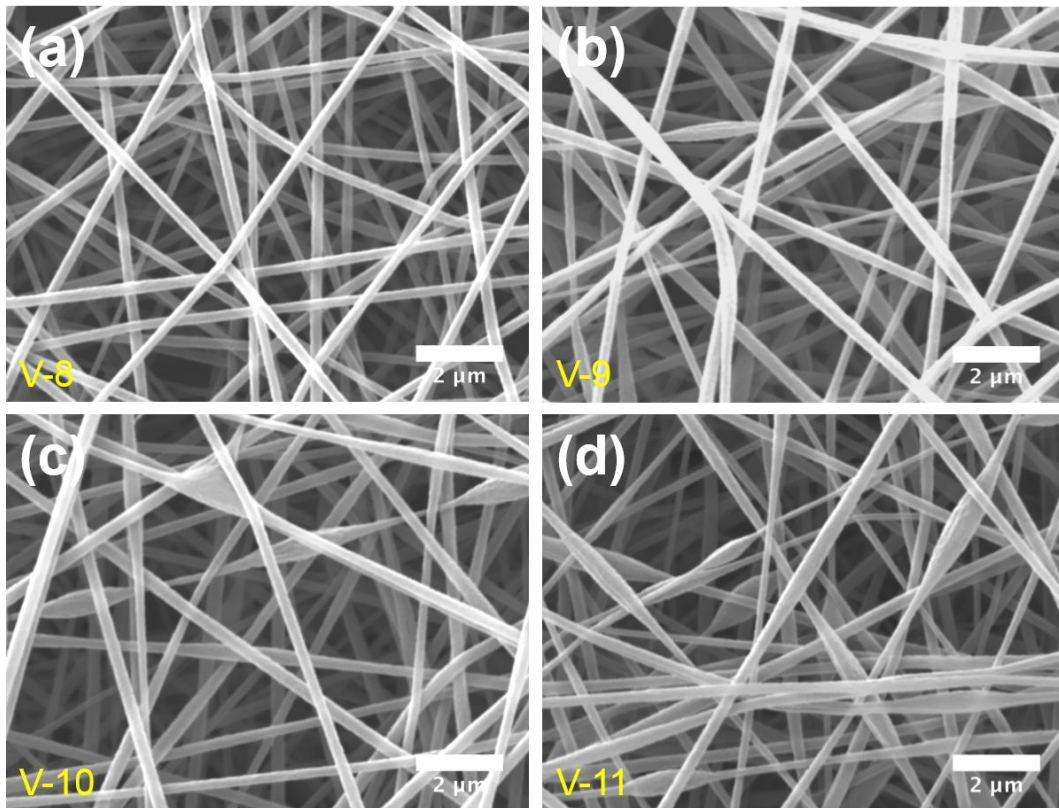


Figure 4.6 SEM images of electrospun PAN NFs deposited on Al collector at various voltages: (a) 16 kV, (b) 17 kV, (c) 18 kV, and (d) 19 kV.

Table 4.2 Quantitative data extracted from SEM images of PAN NFs in the voltage range from 16 to 19 kV.

Sample	Voltage (kV)	d_a (nm)	A_d (μm^2)	F_A	A_b (μm^2)	F_b
V-8	16	223 \pm 28	93.39	0.86	-	-
V-9	17	252 \pm 52	90.63	0.83	2.87	0.03
V-10	18	268 \pm 51	95.51	0.88	4.82	0.04
V-11	19	233 \pm 58	90.64	0.83	11.55	0.11

It was found in the current investigation of effect of voltage, there was not enough electrical forces induced on the electrified solution drop at the needle tip in the voltage range from 0 to 5 kV, as seen in **Figure 4.1(a)**. This is consistent with other evidence shown in **Figure 4.2** and **Figure 4.3(a)**. Similar result was reported by Liu and Adanur, who attributed the absence of the fibre ejection to the too low electrostatic forces induced when compare with the surface tension of the solution [26]. Although the fibre ejection was noticed from voltage of 10 kV, the continuous ejection only started from voltage of 16 kV, which was closely monitored by the camera. Within the continuous fibre ejection region (see **Figure 4.2** and **Figure 4.3**), the diameter of thinnest fibre and thickest fibre is approximately 223 nm and 268 nm, which was obtained at 16 kV and 18 kV, respectively.

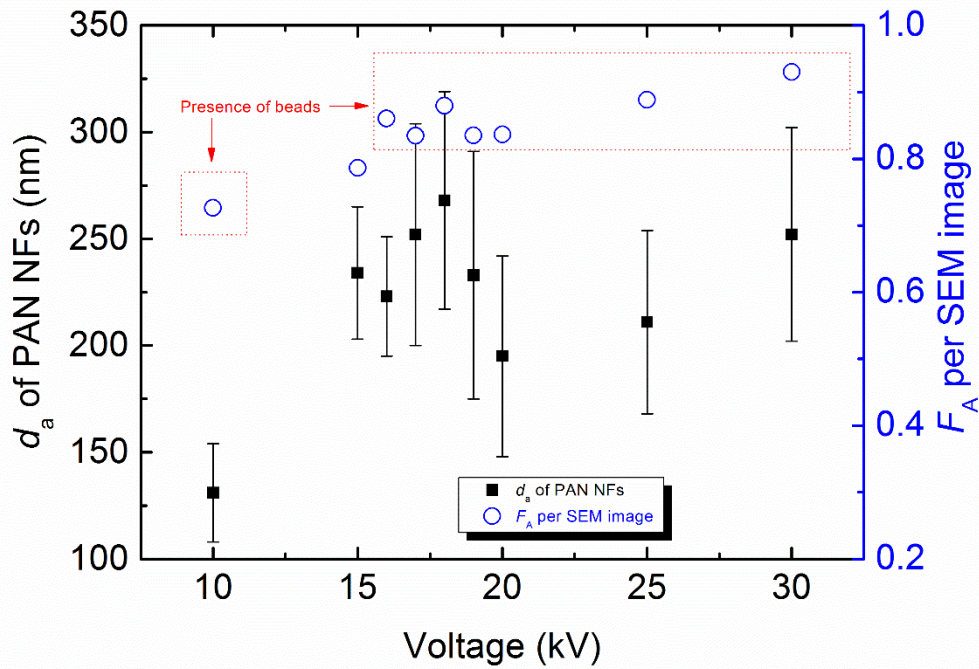


Figure 4.7 d_a of PAN NFs and F_A per SEM image as a function of voltage from 10 to 30 kV.

As presented in **Figure 4.7**, no particular pattern of d_a of PAN NFs was observed with increasing voltage from 16 to 30 kV within the continuous fibre ejection region. Some authors claimed that with increased voltage, the resulted fibre diameter should increase because more polymer ejection occurred [102]. On the other hand, there are reports suggesting that the smaller fibre is formed at higher voltage due to the enhanced electrostatic repulsive forces on the polymer jet [20]. Due to the irregular pattern observed in the current study regarding to the average fibre diameter of electrospun PAN fibres with increasing voltage, it is not realistic to attribute such observation to either of the statements described as above. It worth to mentioned that besides the change of fibre diameter, the emergence of the beads was noticed for the electrospun fibres produced under the voltage magnitude greater than 16 kV. The formation of beads was reported as a prevalent problem associated with high voltage for electrospinning technique. Deitzel *et al.* correlated beaded morphology with spinning current, which can reflect the mass flow rate of electrified solution from needle tip to the collector, while other parameters were held the same [29]. Garg and Bowlin suggested that the jet velocity was increased as well as the polymer solution at needle

tip was consumed more quickly with increasing voltage [15]. This led to the violent oscillation of Taylor cone as well as the instability of the jet [15, 29]. The irregular fibre diameter change with increasing voltage observed in the current investigation might be likely attributed to the instability of the system at certain voltage range described as above, at least, to a certain extent.

4.1.2 Tip-to-Collector Distance

To follow the work in section 5.1.3, the effect of TCD was carried out in the TCD range from 5 to 30 cm with each increment of 5 cm, while voltage and Q were fixed at 16 kV and 1.5 mL/h, respectively. **Figure 4.8** shows the solution drop change in the TCD range from 5 to 30 cm. By consulting **Figure 4.1**, it was expected the solution drop with TCD of 5 cm at fixed voltage would experience the most elongation in the direction parallel to the needle axis. Indeed, the large solution drop on the needle tip was strongly attracted toward to collector shown in **Figure 4.8(a)**. As TCD was increased to higher values from 10 to 30 cm, less attraction was witnessed and are presented in **Figure 4.8(b)-(f)**.

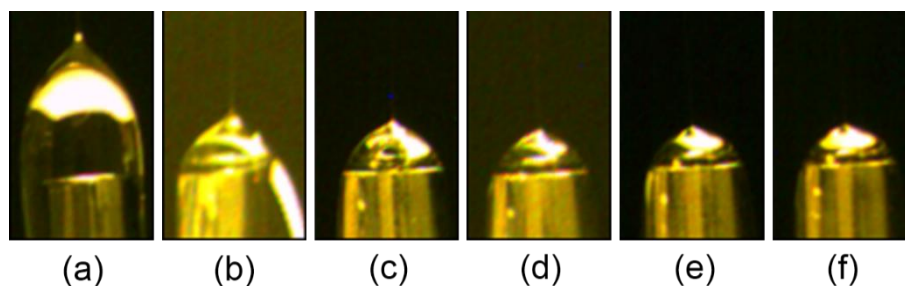


Figure 4.8 Optical images of solution drop formed at the needle tip as a function of TCD:

(a) 5 cm, (b) 10 cm, (c) 15 cm, (d) 20 cm, (e) 25 cm, and (f) 30 cm.

Under the influence of different TCD from 5 to 30 cm, the images of the resulted fibre mats with dimension information are presented in **Figure 4.9**. It can be seen that with increasing TCD from 5 to 30 cm, size of PAN fibre mat was significantly increased. However, the thickness of the fibre

mat was reduced dramatically, in particular at higher TCD values from 25 to 30 cm. During to the extremely wide distribution of PAN NFs on the collector, the extract size of fibre mat was difficult to be determined, hence only photos of these two samples were inserted in **Figure 4.9**. It might be worth mentioning that, the changes in the fibre mat observed in **Figure 4.9** are consistent with the ones presented for the continuous fibre ejection region in **Figure 4.2**. It seems now that the smaller fibre mat was favoured by the higher electrical field [102].

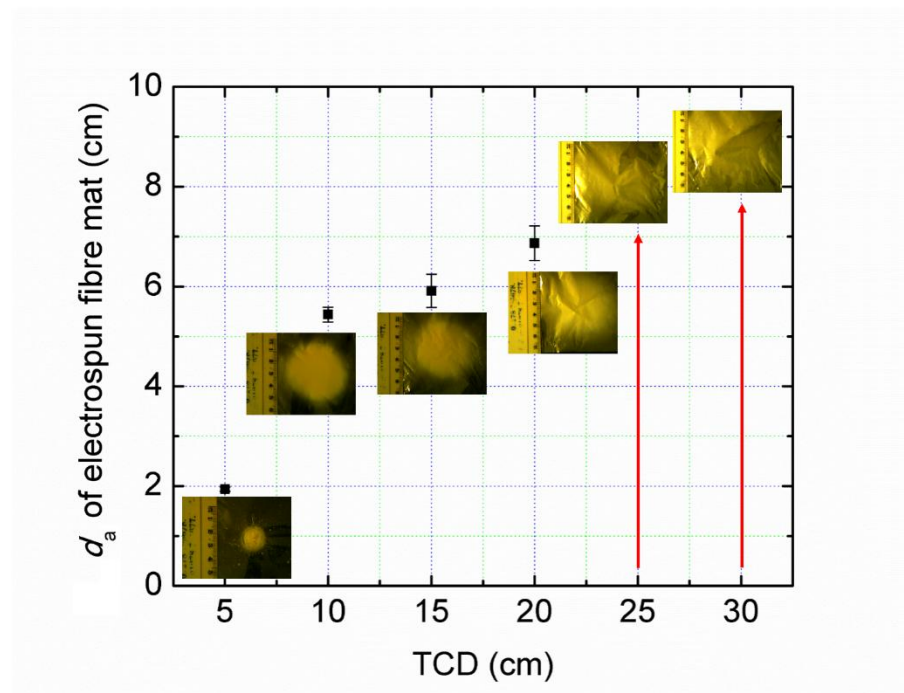


Figure 4.9 Quantitative plot of d_a of electrospun PAN fibre mat as a function of TCD of 5-20 cm. The photos of electrospun PAN fibre mats including with TCD at 25 and 30 cm are inserted.

Figure 4.10 shows the morphology of electrospun PAN NFs deposited on Al foil collector with increasing TCD from 5 to 30 cm. As appeared in **Figure 4.10(a)**, the resulted PAN NFs with TCD of 5 cm was greatly fused and lack of uniformity. The formation of the fused PAN NFs was likely caused by the insufficient flying time for the solvent evaporation, given by the short distance of 5 cm. By increasing TCD to 10 cm or higher, the morphology of the fibres was greatly improved.

But the deposition area extracted from SEM images was hugely decreased. More quantitative information extracted from SEM images of **Figure 4.10** are listed in **Table 4.3**.

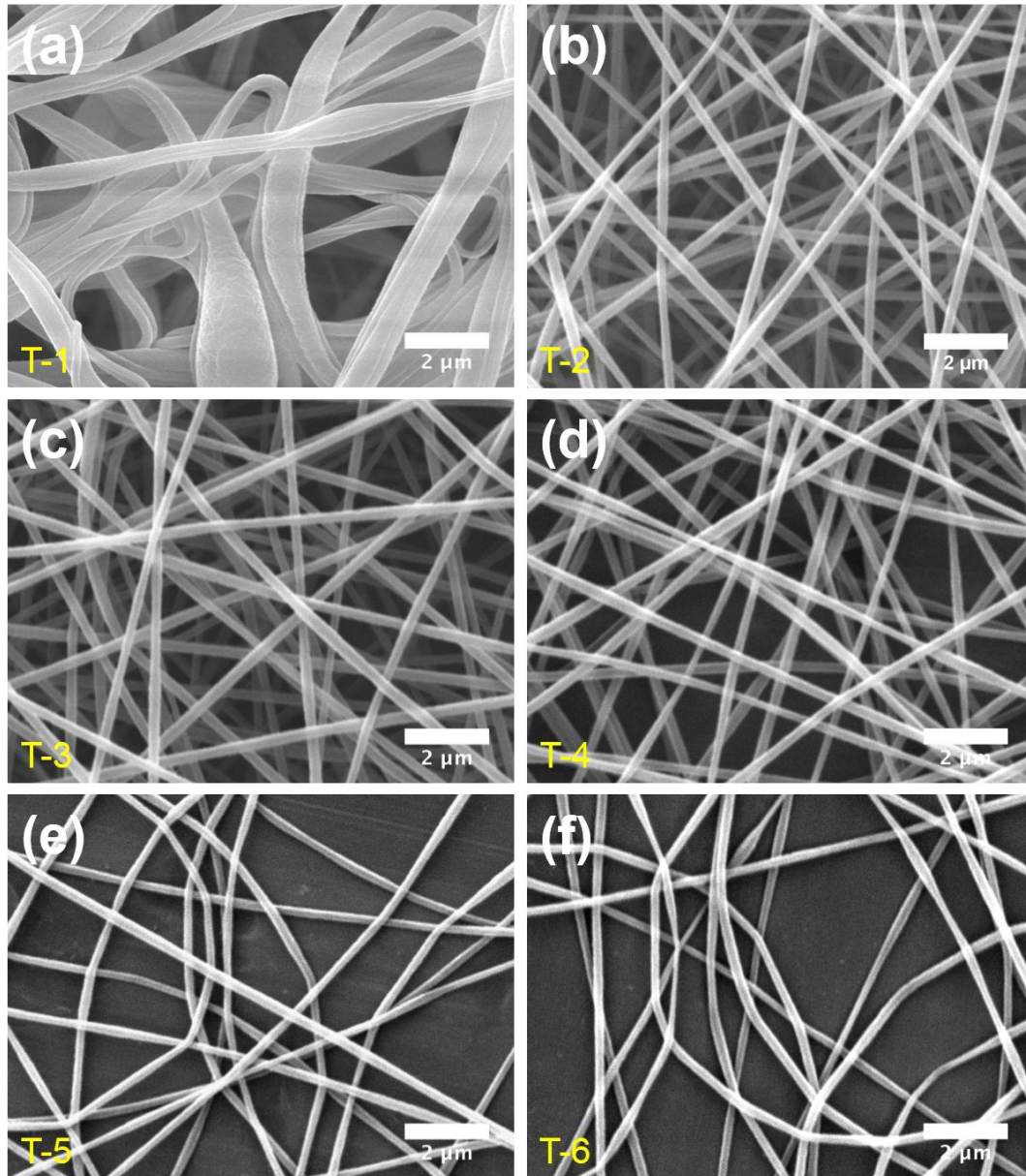


Figure 4.10 SEM images of electrospun PAN NFs deposited on Al collector at various TCD: (a) 5 cm, (b) 10 cm, (c) 15 cm, (d) 20 cm, (e) 25 cm, and (f) 30 cm.

Table 4.3 Quantitative data extracted from SEM images of PAN NFs in the TCD range from 10 to 30 kV.

Sample	TCD (cm)	d_a (nm)	A_d (μm^2)	F_A	A_b (μm^2)	F_b
T-1	5	279 \pm 94	98.59	0.91	13.07	0.12
T-2	10	224 \pm 39	91.70	0.84	-	-
T-3	15	256 \pm 38	90.68	0.84	-	-
T-4	20	241 \pm 33	66.70	0.61	-	-
T-5	25	197 \pm 27	31.21	0.29	-	-
T-6	30	198 \pm 25	31.60	0.29	-	-

To follow the selection rules set for the optimization of processing parameter described in section 4.1, the smaller TCD range from 11 to 12 cm with each increment of 1 cm was selected for the further experiment. The solution drop change in the TCD range from 11 to 14 cm is shown in **Figure 4.11**. Little change of solution drop with increasing TCD was noticed.

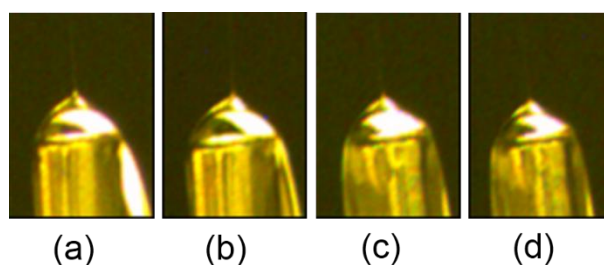


Figure 4.11 Optical images of solution drop formed at the needle tip as a function of TCD:
(a) 11 cm, (b) 12 cm, (c) 13 cm, and (d) 14 cm.

Under the influence of different TCD from 11 to 14 cm, the images of the resulted fibre mats with dimension information are presented in **Figure 4.12**. With increasing TCD from 11 to 14 cm, a very steady increase in the size of PAN mats associated with decrease in thickness was observed.

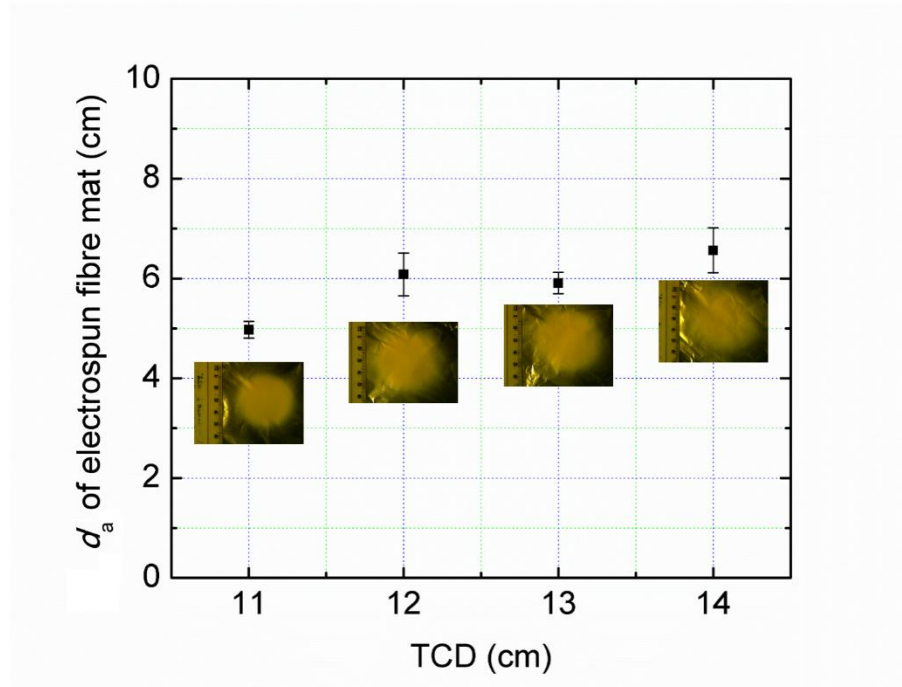


Figure 4.12 Quantitative plot of d_a of electrospun PAN fibre mat as a function of TCD of 11-14 cm.

Figure 4.13 shows the morphology of electrospun PAN NFs deposited on Al foil collector with increasing TCD from 11 to 14 cm. As shown in **Figure 4.13**, all the fibres were bead-free and with good uniformity. The quantitative information extracted from SEM images of **Figure 4.13** are listed in **Table 4.4**.

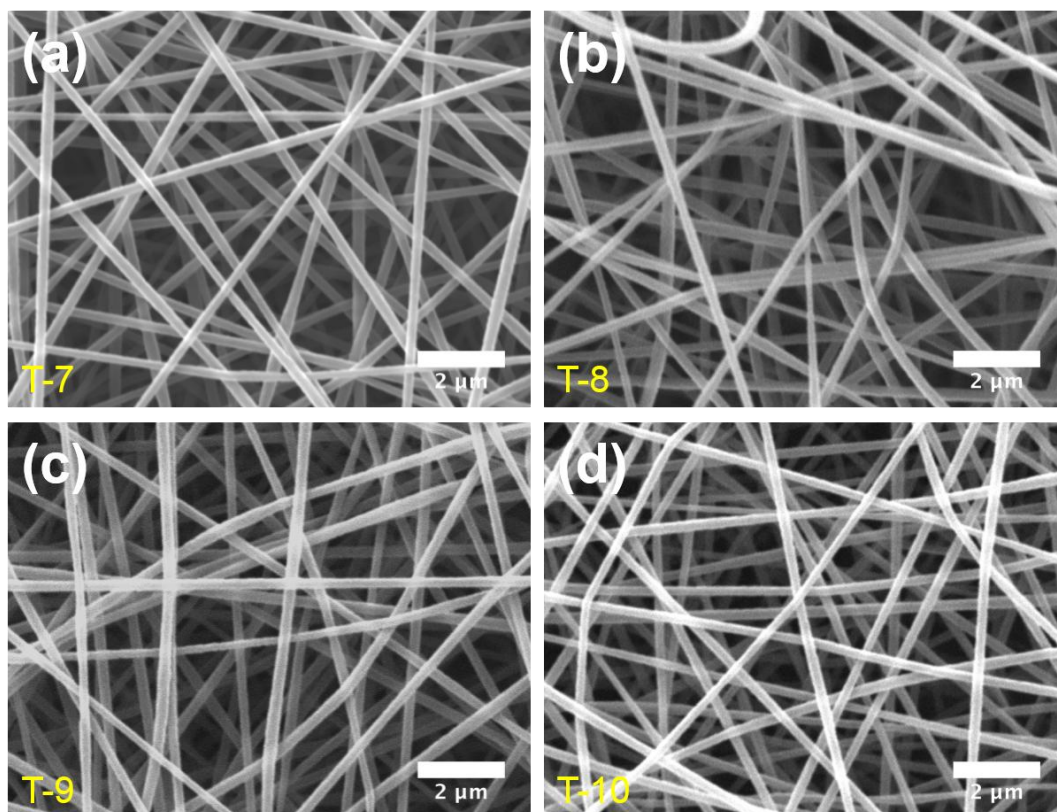


Figure 4.13 SEM images of electrospun PAN NFs deposited on Al collector at various TCD: (a) 11 cm, (b) 12 cm, (c) 13 cm, and (d) 14 cm.

Table 4.4 Quantitative data extracted from SEM images of PAN NFs in the TCD range from 11 to 14 cm.

Sample	TCD (kV)	d_a (nm)	A_d (μm^2)	F_A	A_b (μm^2)	F_b
T-7	11	254 ± 32	94.38	0.87	-	-
T-8	12	238 ± 40	91.96	0.85	-	-
T-9	13	242 ± 31	96.50	0.89	-	-
T-10	14	236 ± 32	96.40	0.89	-	-

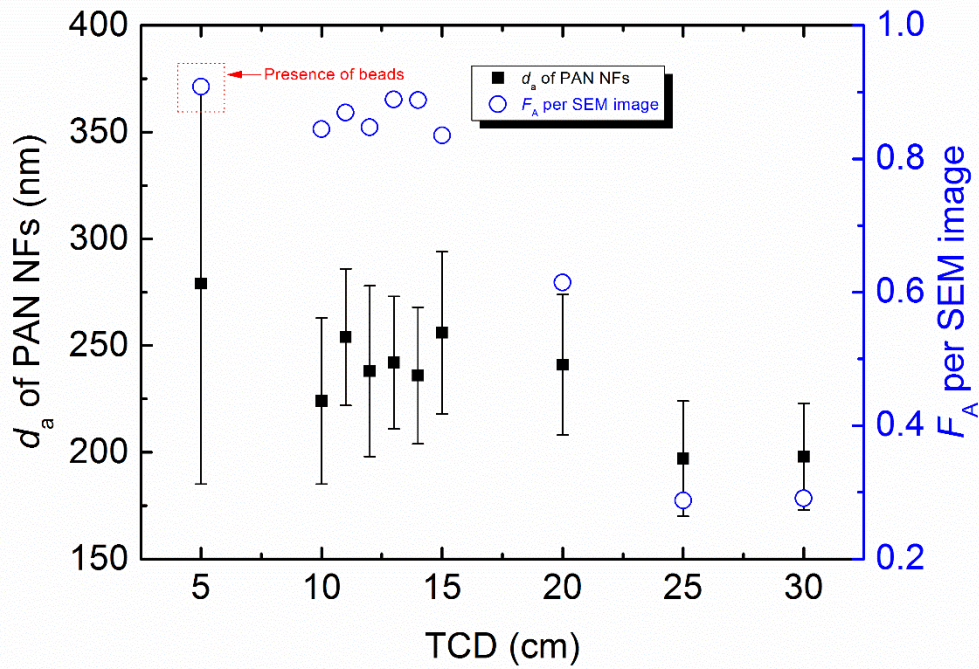


Figure 4.14 d_a of PAN NFs and F_A per SEM image as a function of TCD from 5 to 30 cm.

In general, it can be seen that with increasing TCD the average diameter was generally decreased in **Figure 4.14**. The thickest fibre diameter in the investigation of effect of TCD was obtained at TCD of 5 cm, which was due to the too short evaporation time, given by strong electrical field. The large diameter variation observed in the same case is due to the formation of fused fibres due to the insufficient time required for the solvent evaporation before hit the collector. Besides sample T-1 collected at TCD of 5 cm, the relatively good uniformity of the fibres were obtained for samples electrospun at TCD of 10 to 30 cm. The longer distance permitted the sufficient fibre stretching, hence smallest diameter approximately at 198 nm was obtained at higher TCD from 25 to 30 cm. Apart from the trend observed in the fibre diameter against increasing TCD, the change on the F_A per SEM image was more magnificent. As presented in **Figure 4.10**, the least deposition area per SEM image was found in sample T-5 and T-6 which associated with higher TCD at 25-30 cm. The scarce deposition at higher TCD is likely due to the less polymer ejection caused by the weaker electrical field, induced by the fixed voltage to increased TCD [102].

4.1.3 Flow Rate

Based on the analysis of the results obtained from section 4.1.1 and 4.1.2, two different TCD at 10 and 14 cm were likely to yield optimized fibrous morphology. For this reason, the effect of Q was carried out at 10 and 14 cm, respectively. **Figure 4.15** shows the solution drop change in the Q range from 0.5 to 3 mL/h with each increment of 0.5 mL/h, while TCD was fixed at 10 cm. The solution drop change in the same Q range with TCD of 14 cm is presented in **Figure 4.16**.

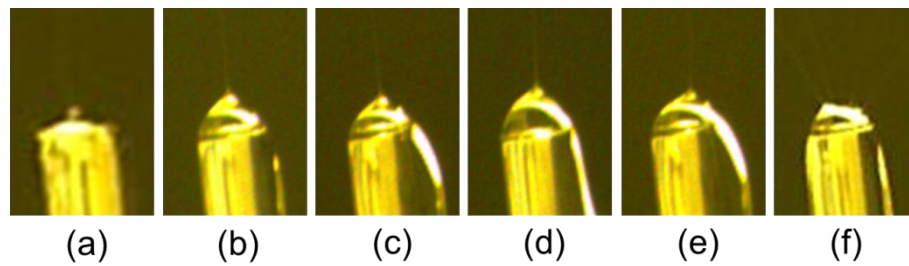


Figure 4.15 Optical images of solution drop formed at the needle tip as a function of Q with TCD of 10cm: (a) 0.5 mL/h, (b) 1 mL/h, (c) 1.5 mL/h, (d) 2 mL/h, (e) 2.5 mL/h, and (f) 3 mL/h.

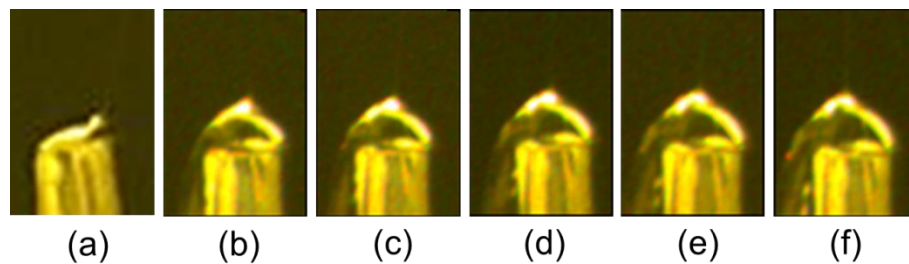


Figure 4.16 Optical images of solution drop formed at the needle tip as a function of Q with TCD of 14cm: (a) 0.5 mL/h, (b) 1 mL/h, (c) 1.5 mL/h, (d) 2 mL/h, (e) 2.5 mL/h, and (f) 3 mL/h.

In the cases with TCD of 10 cm, the status of the solution drop in the middle range of Q from 1 to 2 mL/h looked similar in **Figure 4.13(b)-(d)**. However, the solution drops with Q of 0.5 and 2.5-3 mL/h, experienced very unstable events. At Q of 0.5 mL/h, the fibre ejection in **Figure 4.15(a)** was found originated from the inside of the needle tip. As for Q at 2.5-3 mL/h, more than one jet was initiated from the solution drop as seen in **Figure 4.15(e)-(f)**. In comparison with TCD of 14 cm, only the solution drop with Q of 0.5 mL/h showed unstable activity around the needle in **Figure 4.16(a)**. Whereas for the Q with higher rate, the status of the solution drop was very similar to each other, as presented in **Figure 4.16(b)-(f)**.

Under the influence of different Q from 0.5 to 3 mL/h with TCD of 10 and 14 cm, the images of the resulted fibre mats with dimension information are presented in **Figure 4.17**.

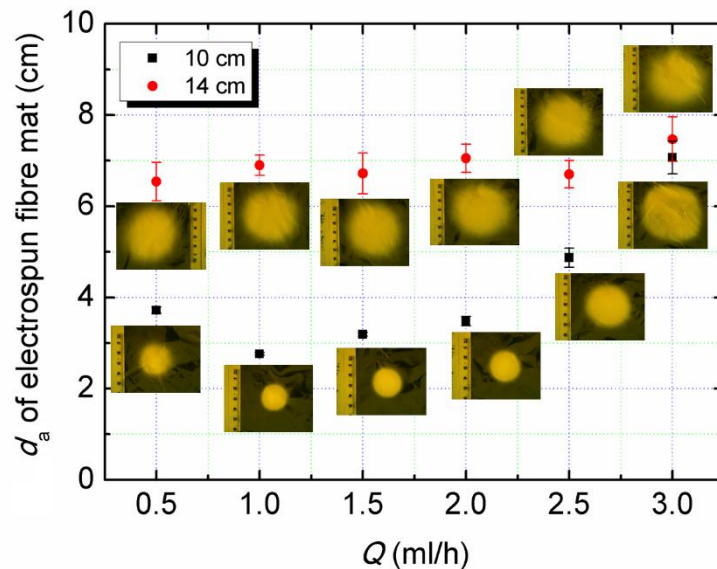


Figure 4.17 Quantitative plot of d_a of electrospun PAN fibre mat as a function of Q of 0.5-3 mL/h with TCD of 10cm and 14 cm, respectively. The photos of electrospun PAN fibre mats are inserted.

As indicated in black, the size of the fibre mat at TCD of 10 cm was firstly decreased by increasing Q from 0.5 to 1 mL/h, then started to increase with further increasing Q from 1 to 3 mL/h. The

enormous size of fibre mat observed with Q of 3 mL/h was thought to be the result of multi-jet ejection. In contrast, at TCD of 14 cm the fibre mat size almost shown no change with increasing Q .

Figure 4.18 shows the morphology of electrospun PAN NFs deposited on Al foil collector with increasing Q from 0.5 to 3 mL/h at TCD of 10 cm. It can be seen that with Q from 0.5 to 2 mL/h, the resulted PAN NFs were highly beaded in **Figure 4.18(a)-(d)**. By increasing Q increased to 2.5-3 mL/h, smooth fibres were resulted in **Figure 4.18(e)-(f)**. On the other hand, when TCD of 14 cm was applied. The resulted fibres were generally smooth with one exception when Q was 0.5 mL/h, as evidenced in **Figure 4.19**. The quantitative information extracted from the SEM images of **Figure 4.18-Figure 4.19** are listed in **Table 4.5**. A plot of d_a of PAN NFs with various Q at two different TCD, 10 cm and 14 cm are presented in **Figure 4.20**.

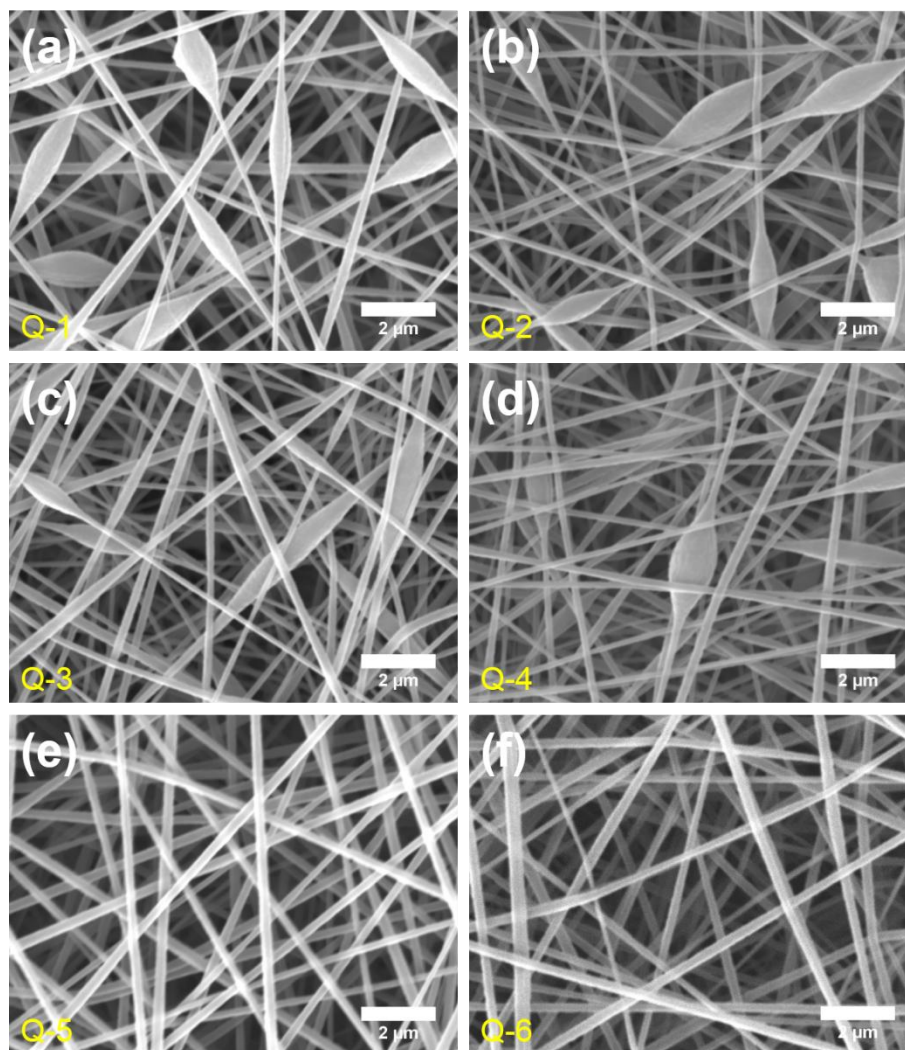


Figure 4.18 SEM images of electrospun PAN NFs deposited on Al collector with various Q at TCD of 10 cm: (a) 0.5 mL/h, (b) 1 mL/h, (c) 1.5 mL/h, (d) 2 mL/h, (e) 2.5 mL/h, and (f) 3 mL/h.

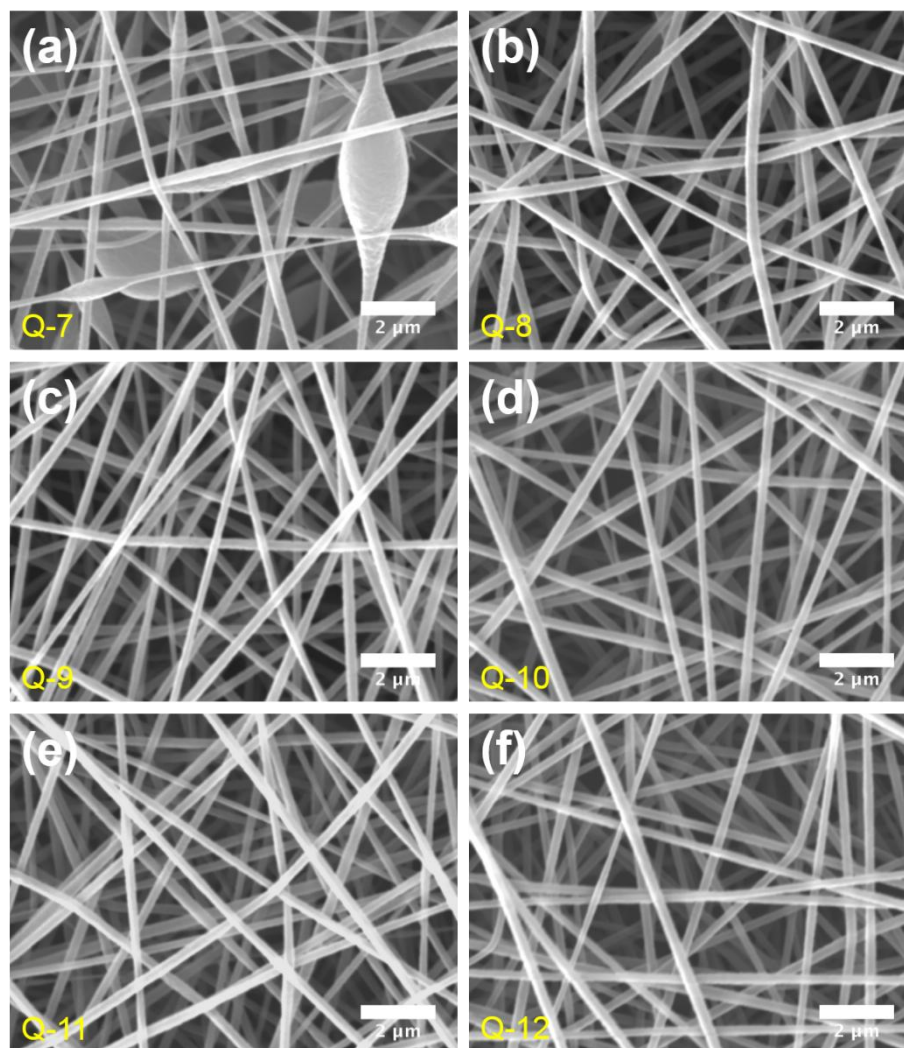


Figure 4.19 SEM images of electrospun PAN NFs deposited on Al collector with various Q at TCD of 14 cm: (a) 0.5 mL/h, (b) 1 mL/h, (c) 1.5 mL/h, (d) 2 mL/h, (e) 2.5 mL/h, and (f) 3 mL/h.

Table 4.5 Quantitative data extracted from SEM images of PAN NFs with various Q ranging from 0.5 to 3 mL/h at TCD of 10 and 14 cm.

Sample	Q (mL/h)	TCD (cm)	d_a (nm)
Q-1	0.5	10	189 ± 46
Q-2	1	10	185 ± 63
Q-3	1.5	10	186 ± 65
Q-4	2	10	205 ± 34
Q-5	2.5	10	243 ± 41
Q-6	3	10	251 ± 27
Q-7	0.5	14	196 ± 48
Q-8	1	14	267 ± 30
Q-9	1.5	14	252 ± 37
Q-10	2	14	257 ± 36
Q-11	2.5	14	254 ± 33
Q-12	3	14	252 ± 33

After the optimization of voltage and TCD from section 4.1.1 and 4.1.2, both TCD of 10 cm and 14 cm were chose to study the effect of Q from 0.5 to 3 mL/h. Unlike the results obtained for sample T-2 shown in **Figure 4.10**, sample Q-2 with same processing parameters showed beaded structure within the fibres. The discrepancy of the results from two batches can be attributed to

the combining effect from other uncontrolled parameters, such as temperature, humidity, and slight concentration difference, etc. With TCD of 10 cm, the beads disappeared when Q increased to 2.5 mL/h or more. Whereas for TCD of 14 cm, only sample Q-7 with Q of 0.5 mL/h contained beads. Similar to the effect of voltage, no significant impact of Q on the fibre diameter for each TCD was observed in Figure 4.20 for both TCD. However, it was found that the diameter of electrospun fibres with TCD of 14 cm larger than the one with 10 cm. The smaller diameter observed in the cases with TCD of 10 cm is likely due to the stronger electrostatic repulsive force induced on the fibre jet [20].

By recalling **Figure 4.15** and **Figure 4.16**, it can be seen that Q did show significant impact on the bead formation within the electrospun fibres. The solution drop was receded into the needle tip with Q of 0.5 mL/h from a hemispherical shape for a stable condition. This change in the shape and volume of the solution drop on the needle tip suggested that the rate of solution drop was consumed much more quickly than the rate it was delivered to the needle [23]. By increasing Q to 1-2 mL/h, the fibres obtained with TCD of 14 cm were all smooth with good uniformity, suggesting the stable state of electrospinning. While the fibres with TCD of 10 cm remained beaded, the good balance was restored when Q reached 2.5-3 mL/h. The change in the morphology from beaded fibre to smooth fibre, suggested that the quicker consumption of solution at needle tip was compensated by the increased Q .

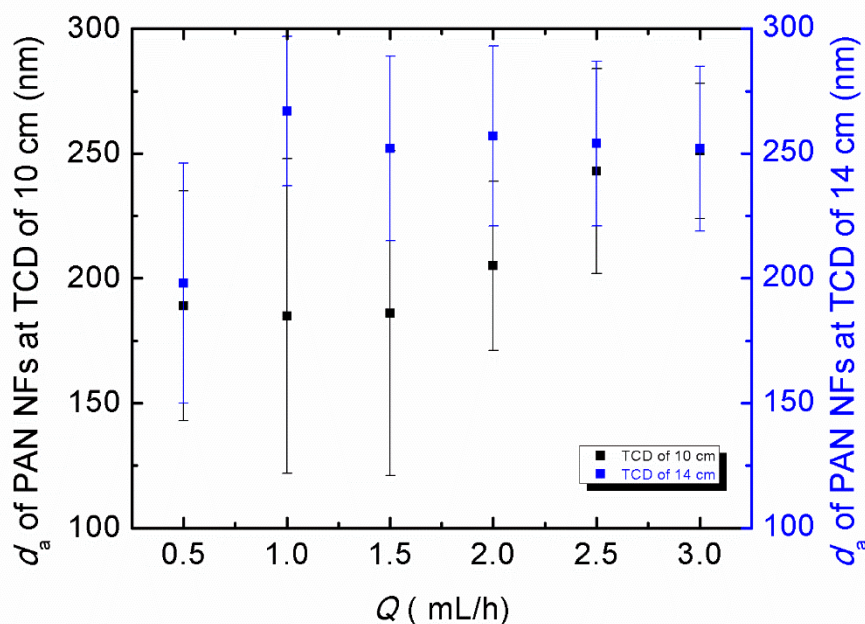


Figure 4.20 d_a of PAN NFs as a function of Q from 0.5 to 3 mL/h with two different TCD, 10 cm and 14 cm.

4.1.4 Long Stability and High Reproducibility

According to the data shown in **Table 4.5**, when Q value was greater than 0.5 mL/h while voltage of 16 kV and TCD of 14 cm were applied, good fibres with high uniformity were resulted. While little difference was notice on deposition area in **Figure 4.17**, **Figure 4.19** and **Table 4.5**, to discover the processing parameters with high reproducibility as well as long stability; Q at 1 and 1.5 mL/h were selected for the longer deposition at 70 and 120 min, respectively. **Figure 4.21** shows the morphology of electrospun PAN NFs deposited on Al foil collector with Q at 1 and 1.5 mL/h for 70 and 130 min, respectively. In **Figure 4.21(a)**, the processing parameters with Q of 1 mL/h which can yield smooth fibre in **Figure 4.19(b)** resulted the beaded fibres with d_a of 247 ± 58 nm at longer deposition time, reflecting its poor reproducibility and high instability of sample D-1. On the other hand, by using Q of 1.5 mL/h with 16 kV and 14 cm, the fibres maintained their high uniformity and were bead-free, as shown in **Figure 4.21(b)**. The resulted d_a for sample D-2 was measured to be 255 ± 42 nm.

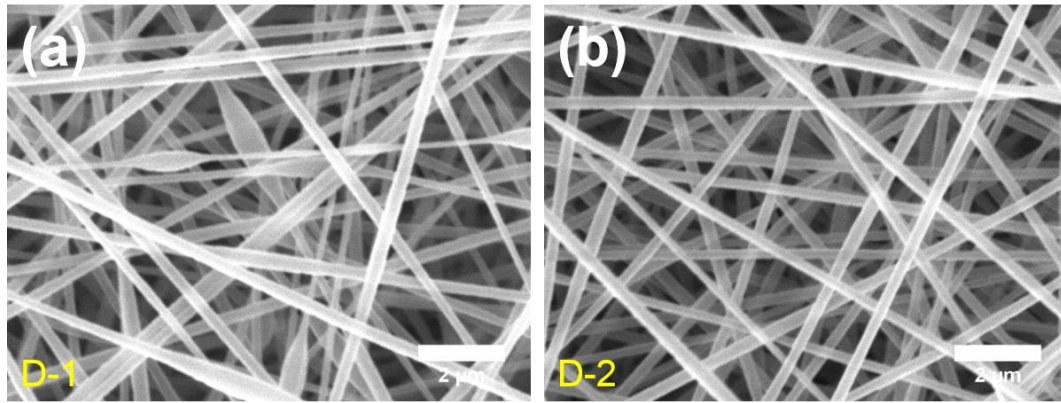


Figure 4.21 SEM images of electrospun PAN NFs deposited on Al collector with voltage of 16 kV and TCD of 14 cm at various Q : (a) 1 mL/h for 70 min, and (b) 1.5 mL/h for 120 min.

Figure 4.22 presents the diameter fluctuation of PAN NFs produced at this optimized conditions, where voltage, TCD and Q were maintained at 16 kV, 14 cm and 1.5 mL/h, respectively from section 5.11, 5.12, 5.13, and 5.14. The sample name for each point is presented next to it in **Figure 4.22**. The detailed experimental condition for each sample can be found in section 4.1.1. Again, the small fluctuation observed here indicated that the optimized processing parameters of 16 kV, 14 cm and 1.5 mL/h possessed high reproducibility and long stability.

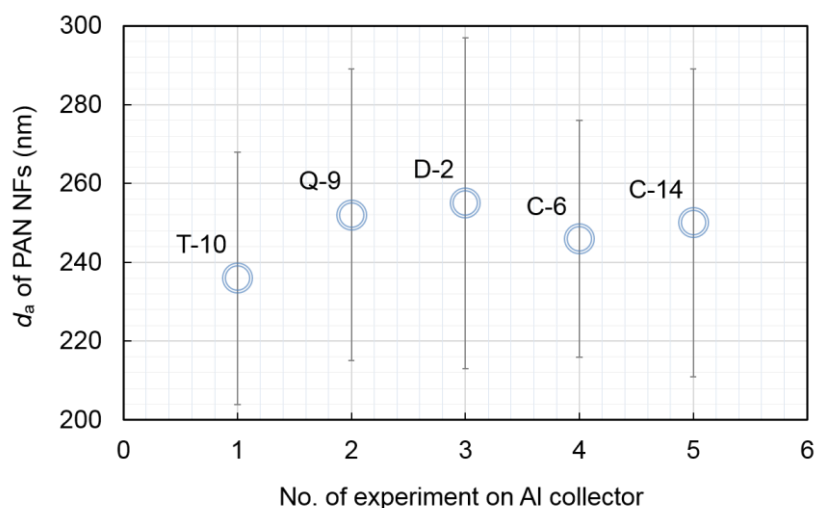


Figure 4.22 Summary of the d_a of PAN NFs electrospun with the optimized processing parameters collected from different samples.

4.2 Solution Parameter

4.2.1 Solution Concentration

The optimized processing parameters obtained with fixed PAN concentration (C) of 12 wt% in section 5.1.4 were fixed in the current section, in order to investigate the effect of various PAN solution concentrations, ranging from 2 to 16 wt% with each increment of 2 wt%. Under the influence of different C from 2 to 16 wt% at deposition time of 2 and 10 min, the images of the resulted PAN mats with dimension information are presented in **Figure 4.23**.

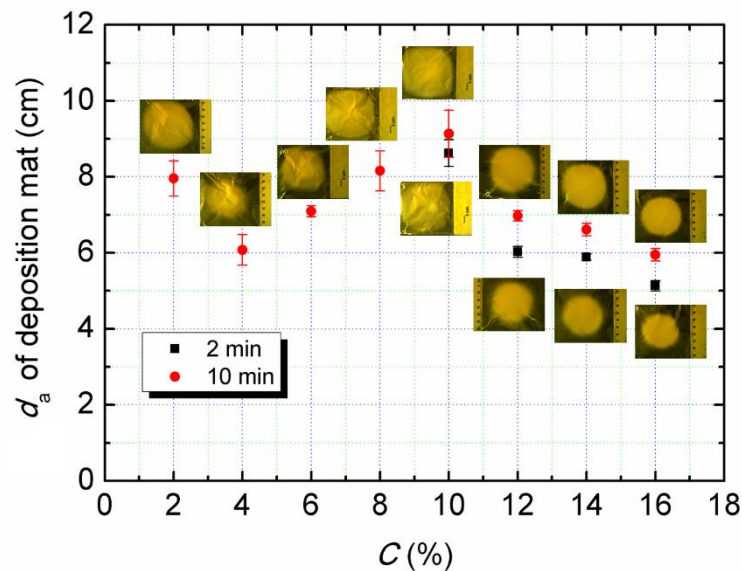


Figure 4.23 Quantitative plot of d_a of PAN mat as a function of C from 2 to 16% at deposition time of 2 and 10 min, respectively. The photos of PAN mats on Al foil collectors are inserted.

In the same deposition time of 10 min, the largest PAN mat was obtained at 10 wt%. With further increasing C , the size of PAN mat decreased while the thickness was increased. Baumgarten investigated the relationship between the length of the straight segment and PAN solution concentration [27]. It was found that the formation of fibre jet was formed when the C was

increased to 7.5 wt% [27]. By increasing C to 17.5 wt%, the straight jet length was increased from ~ 1 to < 20 mm [27]. The observation made by Baumgarten, in fact might be as well able to explain the size change of PAN mat observed in **Figure 4.23**. At fixed TCD, with higher concentration the ratio of straight jet to the TCD was higher, hence reducing the distance for bending instabilities. In addition, higher concentration resulted in higher viscosity which provide better resistance in opposition to bend. For both reasons, the smaller size of PAN mat was found at higher concentrations in **Figure 4.23**.

For the same reasons, it is expected that the thicker diameter resulted from higher concentration. The morphology of electrospun PAN NFs deposited on Al foil collector with increasing C from 2 to 16 wt% at deposition time of 2 and 10 min are respectively shown in **Figure 4.24** and **Figure 4.25**. The quantitative information of fibres extracted from SEM images of **Figure 4.24** and **Figure 4.25** are listed in **Table 4.6**. It can be seen that with C in the range of 2% to 6%, the morphology of the resulted PAN products was bead predominant. Whereas in the higher C region from 8% to 16%, the resulted morphology was transformed into fibre dominated and ultimately smooth fibre with thicker diameter. As proposed by Wang and Kumar, the origin of the bead formation can be caused by two factors, high surface tension and poor polymer entanglement of solution [31]. It was pointed out with increasing solution concentration, the polymer chain entanglement was increased while no significant change was found on surface tension of the solution [31]. In this regard, the morphology transition from beads only to beaded fibres, and finally to the smooth fibres with increasing PAN solution concentration observed in the current study, which can be attributed mainly to the increased polymer chain entanglement in the increased PAN solution [31].

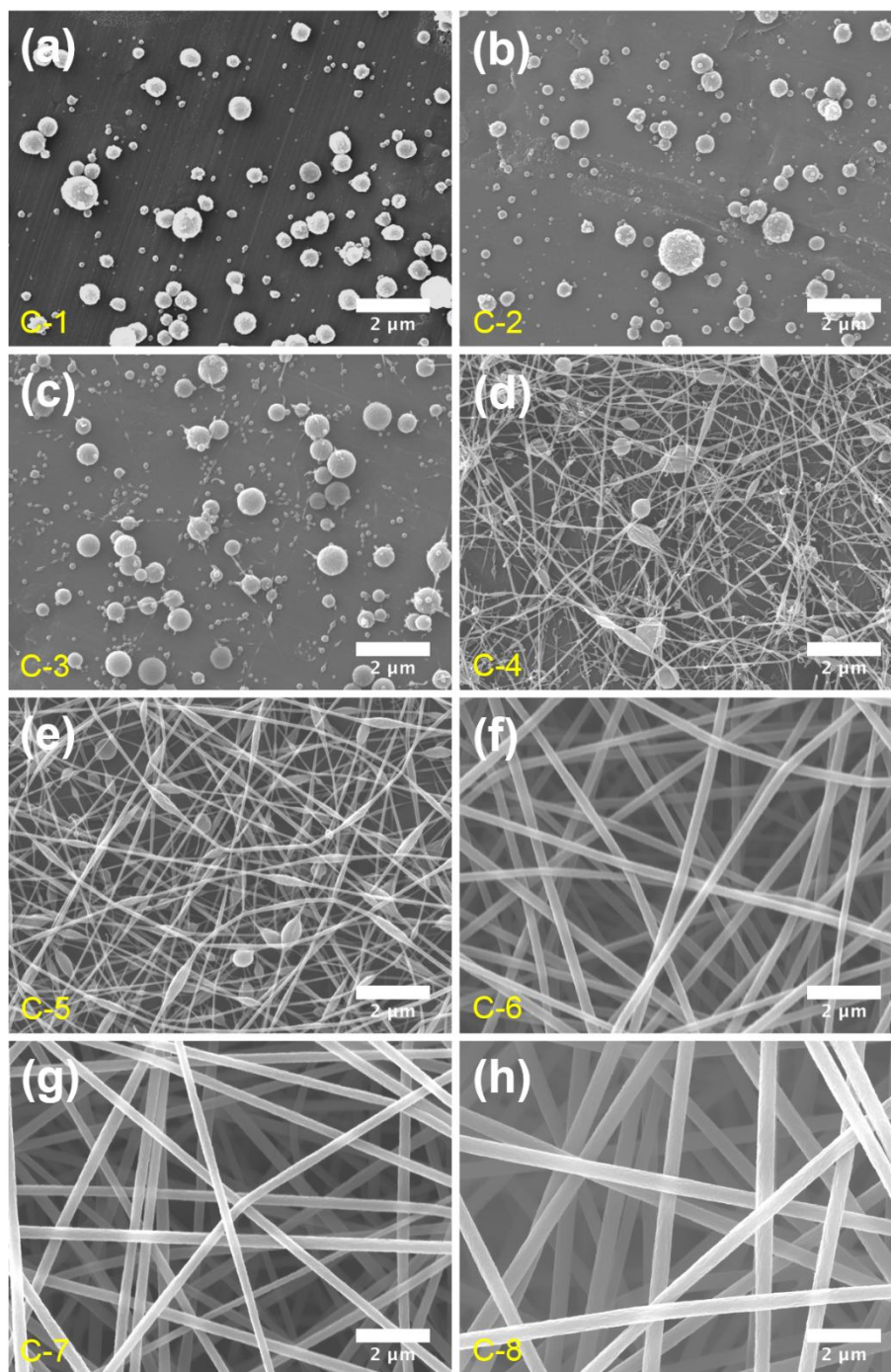


Figure 4.24 SEM images of electrospun PAN products deposited on Al collector for 2min at various concentrations: (a) 2%, (b) 4%, (c) 6%, (d) 8%, (e) 10%, (f) 12%, (g) 14%, and (h) 16%.

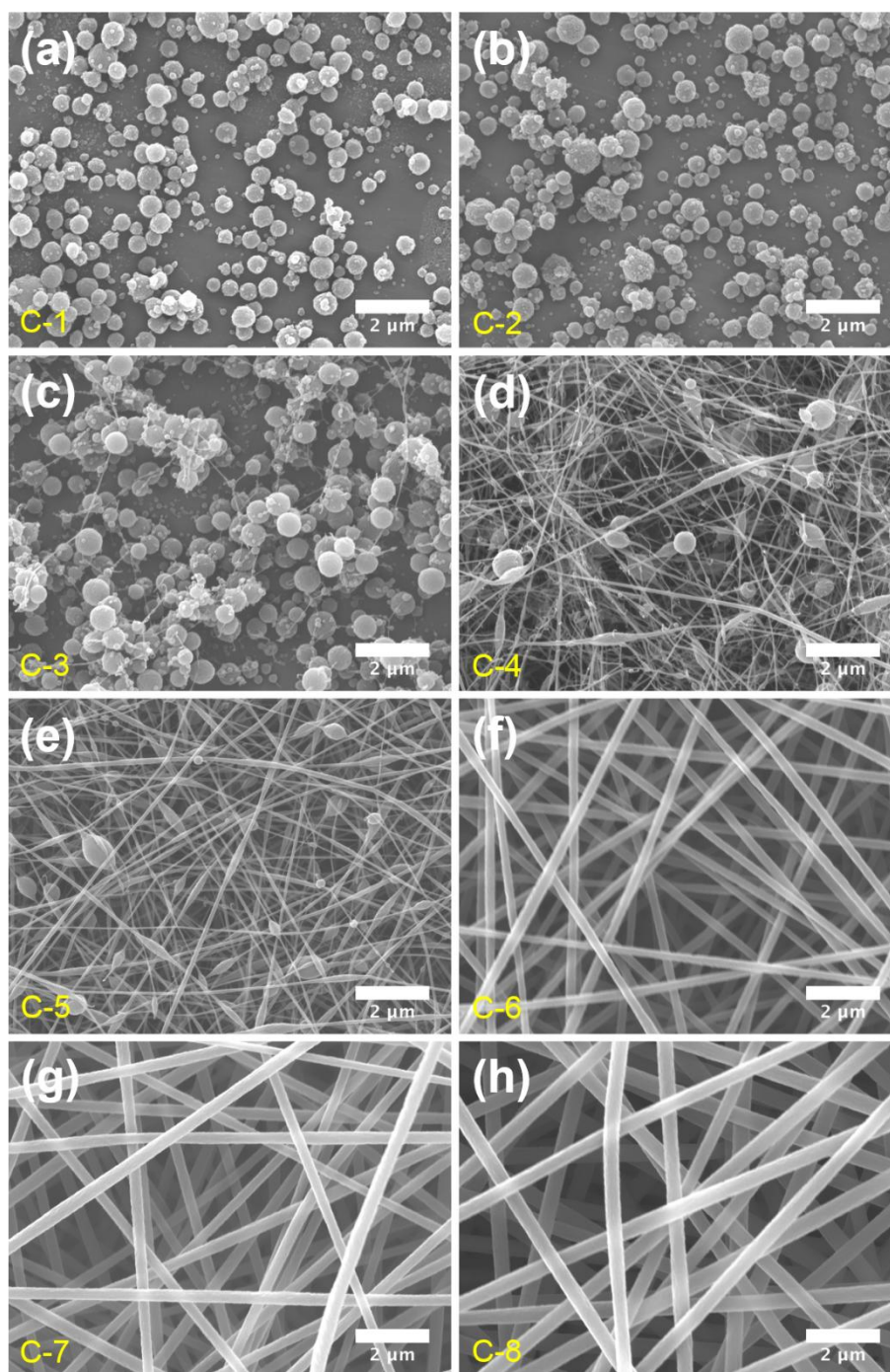


Figure 4.25 SEM images of electrospun PAN products deposited on Al collector for 10min at various concentrations: (a) 2%, (b) 4%, (c) 6%, (d) 8%, (e) 10%, (f) 12%, (g) 14%, and (h) 16%. With an exception for 16% with 8min30s deposition time.

Table 4.6 Quantitative data for d_a of PAN NFs with various PAN solution C from 6 to 16% at deposition time of 2min, and 10min, respectively.

Sample	C (%)	Intended deposition time (min)	Actual deposition time (min)	d_a (nm)
C-4	8	2	2	44 ± 9
C-5	10	2	2	72 ± 18
C-6	12	2	2	246 ± 30
C-7	14	2	2	302 ± 40
C-8	16	2	2	467 ± 45
C-12	8	10	10	50 ± 12
C-13	10	10	10	76 ± 23
C-14	12	10	10	250 ± 39
C-15	14	10	10	315 ± 36
C-16	16	10	8.5	481 ± 38

Due to the same reason, a linear relationship between the average fibre diameter of PAN fibres and PAN solution concentration from 8% to 16% was found at two different time duration, 2min and 10 min, as shown in **Figure 4.26**. Similar observation was also reported by other authors [31, 35].

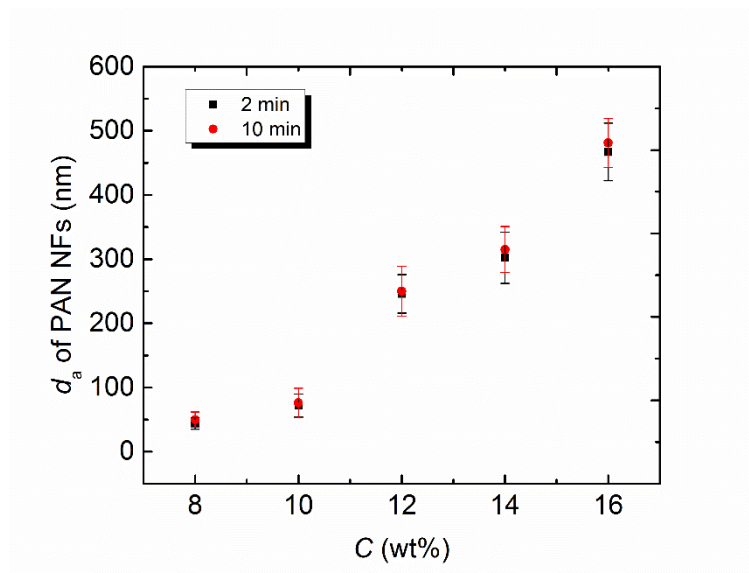


Figure 4.26 Plot of average diameter of the fibres versus concentration from 2 to 16 wt% at two different deposition time of 2 and 10 min.

4.3 Summary

In summary, the effect of four parameters, voltage, TCD, Q and solution concentration on the morphology of the deposited PAN materials was investigated in this chapter. The study on the effect of processing parameters was carried out at fixed PAN solution concentration of 12 wt%. In this study, it was found that both voltage and Q have little impact on the fibre diameter. However, both parameters contributed to the formation of beads. In the investigation of voltage, while TCD and Q controlled at 15 cm and 1.5 mL/h, the formation of beads were observed when voltage was greater than 16 kV. Two different TCD, 10 cm and 14 cm were applied to study the effect of Q from 0.5 to 3 mL/h. The beaded fibres occurred when the mass imbalance occurred at solution drop attached to the needle tip. It was found that a minimum Q was required in order to avoid the mass imbalance. In the case of TCD of 14 cm, the minimum Q for long hour deposition was 1.5 mL/h (see **Figure 4.21**), although the minimum Q of 1 mL/h was observed for short deposition in **Figure 4.19(b)**. Whereas for TCD of 10 cm, the minimum Q was established to be 2.5 mL/h, which was the threshold value to maintain the balance between the rate of the jet consumed from the solution drop at needle tip to the collector and the rate of delivery of solution to the needle tip [29]. The reason for TCD of 10 cm having larger Q to achieve a stable electrospinning condition was forced by the larger electrical field induced by the same magnitude of voltage to smaller TCD. Hence, faster rate of solution being consumed to eject fibre jet from the solution drop was expected. To balance the loss of the solution volume at the solution drop, the larger Q was required. With increasing TCD, a regular pattern of average diameter of the electrospun PAN fibres and more deposition area per SEM image was observed. The decreased fibre diameter with increasing TCD was due to the longer stretching time given by the increased distance between the needle-tip to the collector. The less deposition area per SEM image was due to attractive electrostatic force was weakened by increasing TCD with fixed voltage. The optimized processing parameters was established as voltage of 16 kV, TCD of 14 cm, and Q of 1.5 mL/h. Five individual experiments were carried out to confirm the good reproducibility and long stability of the optimized processing parameters. Small variation of fibre diameter ranging

from approximately 236 to 255 nm was observed. The effect of C was also investigated by fixing the processing parameters on the optimized value. It was found that with increasing C from 2 to 16%, the morphology of PAN product changed from beads only to beaded fibres, and finally smooth fibres. The reasons for the morphological change observed was due to the increasing polymer chain entanglement with increasing C . At low C from 2 to 6%, the ejected polymer jet was broken up into electrified droplets due to the surface tension, which preferred to be in spherical shapes with small surface area per unit mass [14]. With increasing C to 8-16%, the increased polymer chain entanglement provided the enhanced resistance for fluid jet against surface tension, and hence to encourage the formation of the fibre. It was found that with increasing concentration, the diameter of the PAN NFs was increased from approximately 47 to 474 nm with increasing C from 8 to 16%.

Although many data available in literature about various electrospinning parameters, a large variation of final chosen parameters can be found due to the different system setup. It is important to carry out and gain understanding through the optimization process which was specific used in this project, therefore the desired morphology can be obtained and tuned if necessary. The optimization method presented in this work can be applied to any electrospinning system. As an outcome, the information regarding to the optimized processing parameters with effect of C acquired in Chapter 4 was further applied in the fabrication of thick PAN NFs mat with the desirable fibre morphology, which was used as starting material and substrate material for marking CNFs in Chapter 5 and CNWs-CNFs in Chapter 6, respectively.

5 Fabrication and Characterisations of CNFs

5.1 SEM

To verify the reproducibility of the optimized processing parameters obtained from Chapter 4, the PAN NFs studied in Chapter 5 were prepared from 14% PAN solution concentration with processing parameters of 16 kV, 14 cm, and 1.5 ml/h. **Figure 5.1** shows that the resulted electrospun NFs with smooth appearance without no sign of beads, confirming that the electrospinning condition for this PAN sample was stable. As indicated by the inset of **Figure 5.1**, the diameter of electrospun PAN NFs exhibited a normal distribution and d_a was measured to be 306 ± 35 nm, which is very close to the value obtained in **Table 4.6** of Chapter 4, further confirming the good reproducibility of the optimized processing parameters.

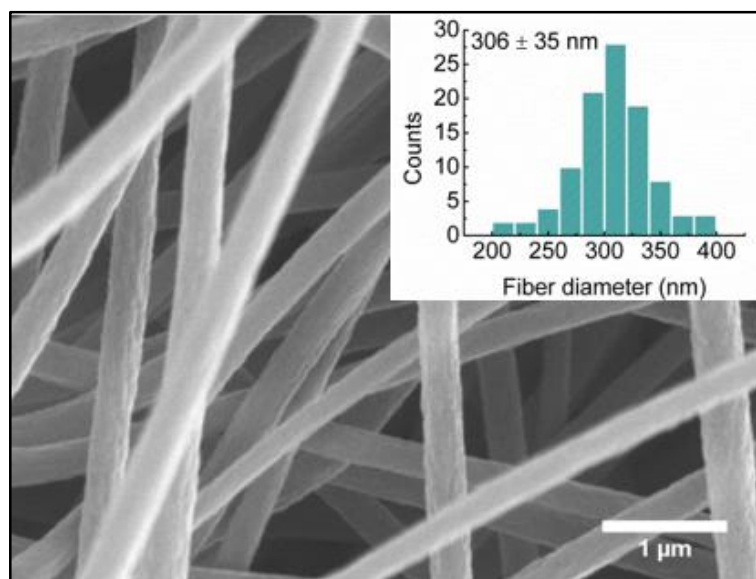


Figure 5.1 SEM image of PAN NFs electrospun from 14% PAN solution with optimized processing parameters of 16 kV, 14 cm and 1.5 ml/h. The average fibre diameter distribution plot counted from 100 fibres is inserted as an inset.

After oxidative stabilisation process, the PAN NFs was slightly reduced to approximately 281 nm, while the general morphology of the fibre shows little change, as evidenced in **Figure 6.2**. To investigate the characteristics of PAN derived CNFs, the stabilized PAN NFs (sample SPAN) was carbonized at various carbonization temperatures, ranging from 500 to 1000 °C.

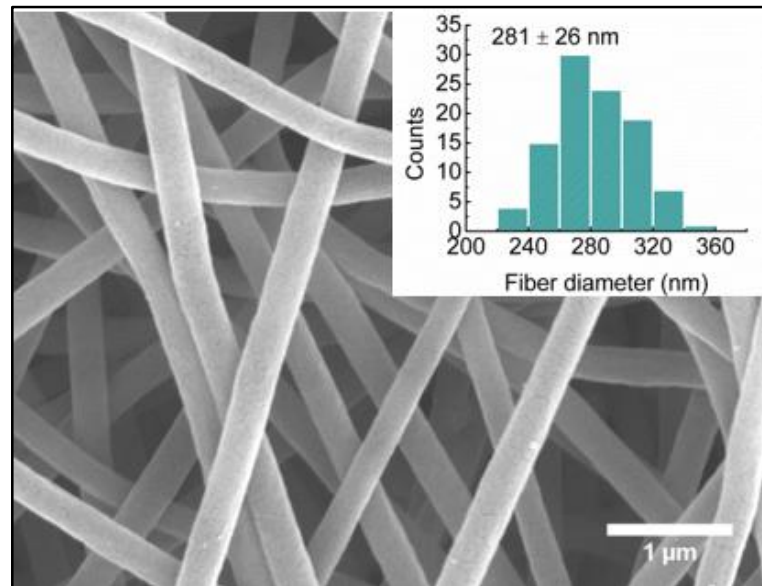


Figure 5.2 SEM image of electrospun PAN NFs after oxidative stabilisation process. The average fibre diameter distribution plot counted from 100 fibres is inserted as an inset.

Similar to the change brought by stabilisation, the morphology of the fibres remained similar to the original fibres while there is a fibre diameter reduction associated. As presented in **Figure 5.3-Figure 5.8**, d_a is reduced progressively with increasing carbonization temperature.

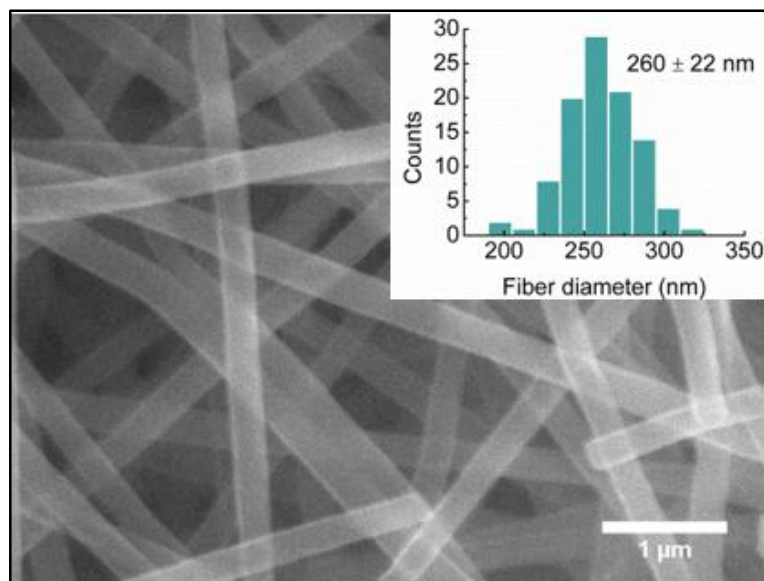


Figure 5.3 SEM image of stabilized PAN NFs after carbonization process at carbonization temperature of 500 °C. The average fibre diameter distribution plot counted from 100 fibres is inserted as an inset.

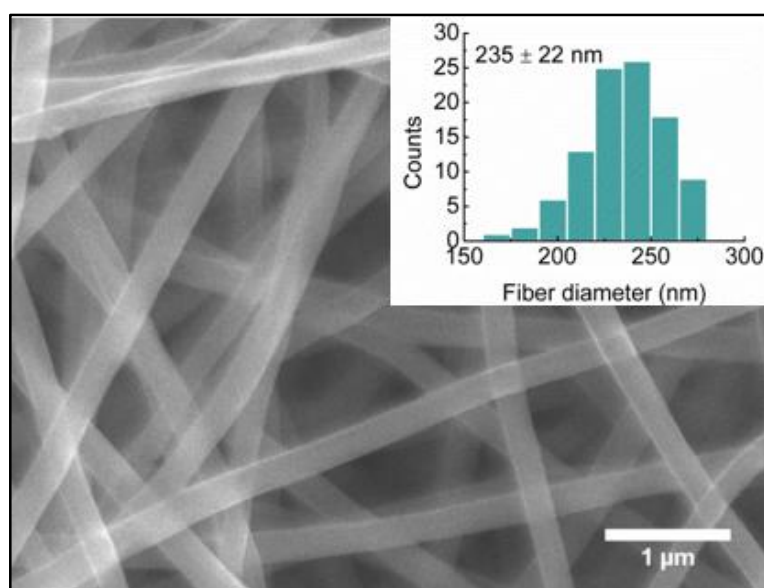


Figure 5.4 SEM image of stabilized PAN NFs after carbonization process at carbonization temperature of 600 °C. The average fibre diameter distribution plot counted from 100 fibres is inserted as an inset.

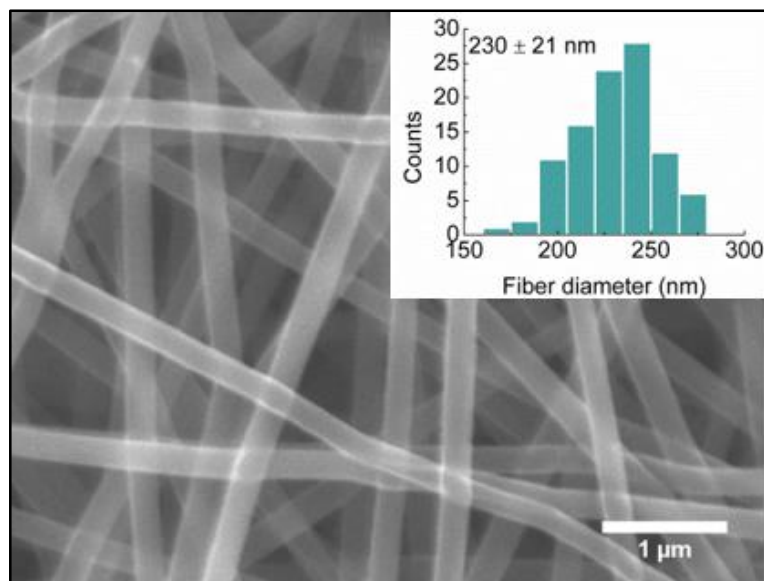


Figure 5.5 SEM image of stabilized PAN NFs after carbonization process at carbonization temperature of 700 °C. The average fibre diameter distribution plot counted from 100 fibres is inserted as an inset.

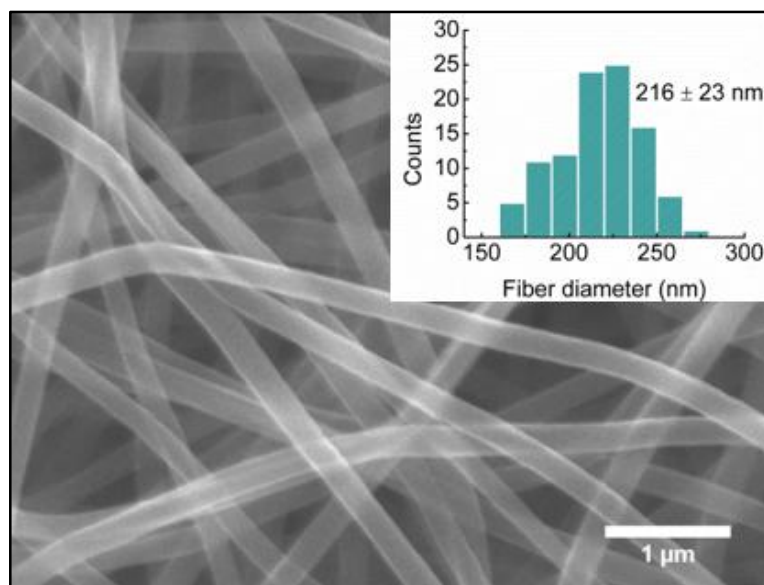


Figure 5.6 SEM image of stabilized PAN NFs after carbonization process at carbonization temperature of 800 °C. The average fibre diameter distribution plot counted from 100 fibres is inserted as an inset.

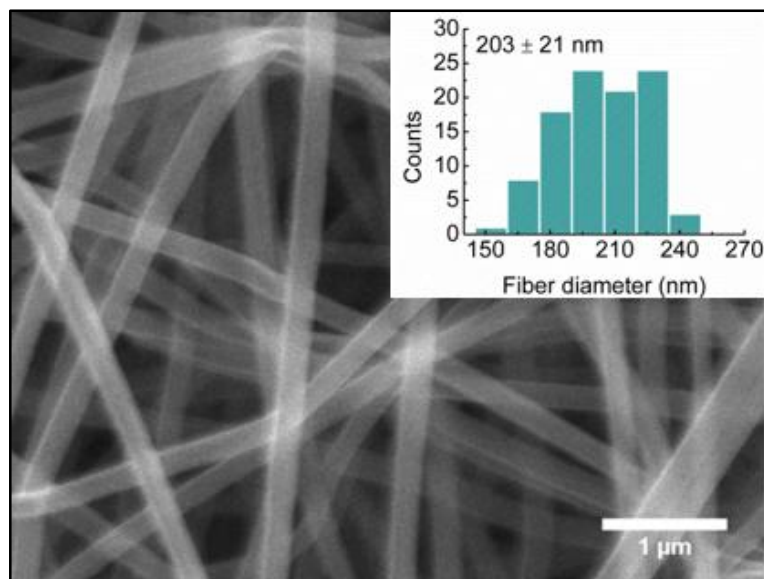


Figure 5.7 SEM image of stabilized PAN NFs after carbonization process at carbonization temperature of 900 °C. The average fibre diameter distribution plot counted from 100 fibres is inserted as an inset.

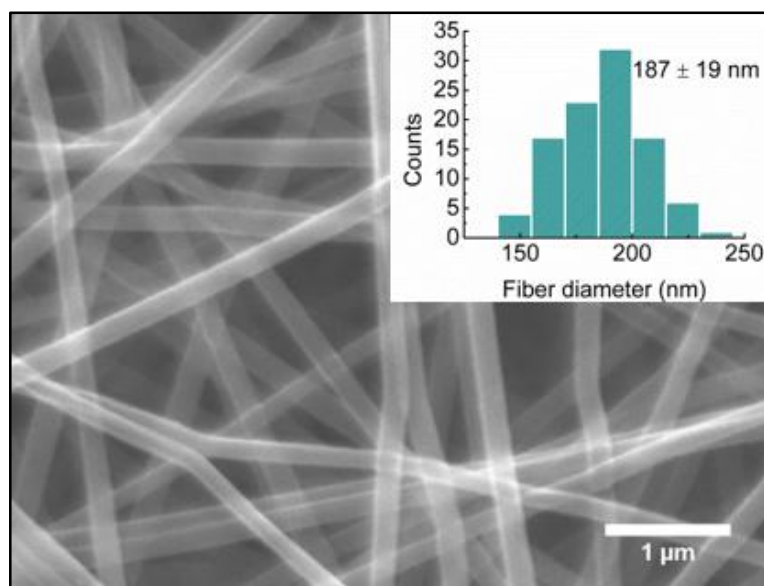


Figure 5.8 SEM image of stabilized PAN NFs after carbonization process at carbonization temperature of 1000 °C. The average fibre diameter distribution plot counted from 100 fibres is inserted as an inset.

The d_a of electrospun PAN NFs treated various conditions was summarized in **Table 5.1**.

Table 5.1 Summary of change of d_a with various heat treatments.

Sample	Description	Carbonization temperature (°C)	d_a (nm)
PAN	Electrospun PAN NFs	-	306 ± 35
SPAN	Stabilized PAN NFs	-	281 ± 26
CNF-500	Carbonized PAN NFs at various carbonization temperatures	500	260 ± 22
CNF-600		600	235 ± 22
CNF-700		700	230 ± 21
CNF-800		800	216 ± 23
CNF-900		900	203 ± 21
CNF-1000		1000	187 ± 19

The linear relationship between d_a and carbonization temperature is plotted in **Figure 5.9**.

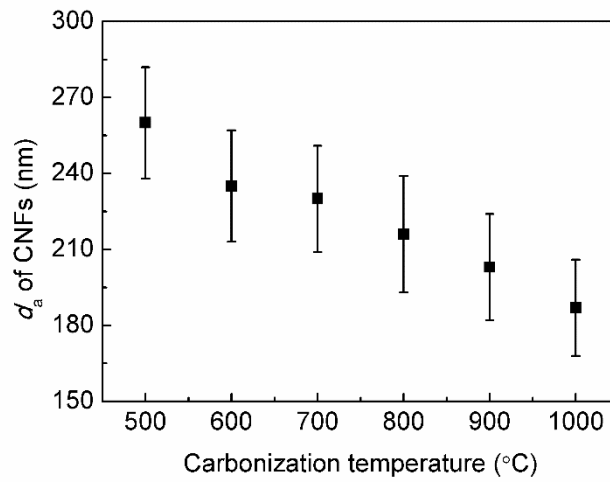


Figure 5.9 Quantitative relationship between the average fibre diameter of CNFs and carbonization temperatures.

As reviewed in Chapter 2, the reduction on the fibre diameter after heat treatments: stabilisation and carbonization are known as a result of non-carbon removal process associated with the evolution of various gases, H₂O, HCN, N₂ and others [77].

5.2 FTIR

FTIR spectra of PAN NFs treated with various heat treatments are presented in **Figure 5.10**.

Figure 5.10(a) shows a typical FTIR spectrum of PAN, which exhibited peaks at 2243 cm^{-1} , 2938 cm^{-1} , 1452 cm^{-1} , 1359 cm^{-1} , and 1253 cm^{-1} . These FTIR peaks are attributed to the presence of nitrile ($\text{C}\equiv\text{N}$) group, and various aliphatic CH groups, including CH, CH_2 and CH_3 , respectively [73]. FTIR peak appears at 1666 cm^{-1} attributed to $\text{C}=\text{O}$ group is considered to be originated from residual DMF solvent due to the insufficient solvent evaporation during the electrospinning process [103]. In the FTIR spectrum of as-purchased PAN powders, such peak is absent [104].

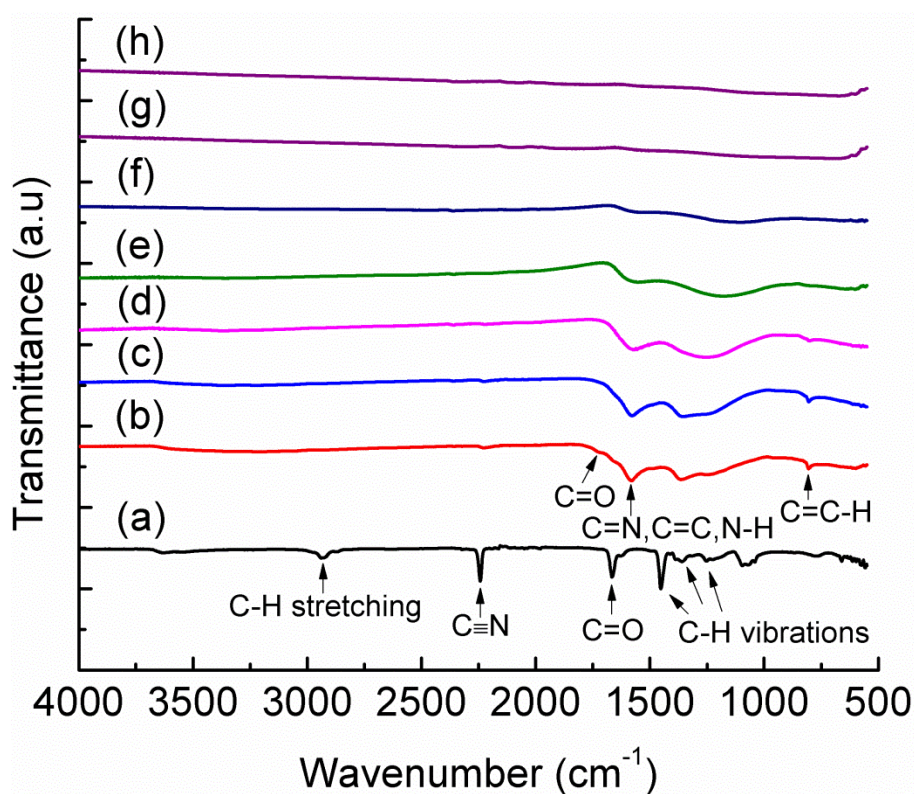


Figure 5.10 FTIR spectra of PAN NFs with various heat treatments: (a) PAN, (b) SPAN, (c) CNF-500, (d) CNF-600, (e) CNF-700, (f) CNF-800, (g) CNF-900 and (h) CNF-1000.

After the oxidative stabilisation, the intensity of the characteristic FTIR peaks for PAN is greatly reduced and this particularly obvious for $\text{C}\equiv\text{N}$ group which is located at 2243 cm^{-1} [71]. Concurrently, there are several new peaks arisen at $\sim 1710\text{ cm}^{-1}$, 1579 cm^{-1} , and 805 cm^{-1} in **Figure**

5.10(b). These newly formed peaks are respectively assigned to C=O, a mix of C=N, C=C and N-H groups, and C=C-H groups [105]. The above noted changes observed in **Figure 5.10(b)** are good indications revealing the chemistry change of PAN NFs during the stabilisation process, cyclization, crosslinking, dehydrogenation, and oxidation [106]. The ladder structure with good heat resistance can be formed upon to the completion of stabilisation process in air [55] and which then allows the survival of fibrous morphology of PAN without melting during the subsequent carbonization process at higher temperature in an inert atmosphere. By using low carbonization temperature of 500 °C, the FTIR spectrum of CNF-500 in **Figure 5.10(c)** shows a high similarity with **Figure 5.10(b)** for stabilised PAN NFs, with only small difference which is the disappearance of C=O peak at $\sim 1710\text{ cm}^{-1}$. By increasing the carbonization temperature to 600-800 °C, the FTIR peaks assigned to C-H vibrations at 1452 cm^{-1} , 1359 cm^{-1} , and 1253 cm^{-1} are merged into one broad peak, as shown in **Figure 5.10(d)-(f)**. With further increasing carbonization temperature to 900-1000 °C, very few functional groups can be seen in **Figure 5.10(g)-(h)**, which is caused by the high absorbance of carbon products [73]. The assignment of main peak of PAN NFs treated with various heat treatments is summarized in **Table 5.2**.

Table 5.2 Assignment of main FTIR peaks of PAN NFs treated with various heat treatments.

Sample	FTIR peak position (cm ⁻¹)					
	C≡N	C-H stretching	C-H vibrations	C=O	C=N, C=C, N-H	C=C-H
PAN	2243	2938	1452, 1359, 1253	1666	-	-
SPAN	2228	-	1364, 1251	1710	1579	805
CNF-500	2227	-	1354,1276	-	1575	804
CNF-600	-	-	1258	-	1574	802
CNF-700	-	-	1178	-	1557	-
CNF-800	-	-	1101	-	1537	-
CNF-900	-	-	-	-	-	-
CNF-1000	-	-	-	-	-	-

5.3 Raman

Raman spectra of SPAN sample carbonized with various carbonization temperatures ranging from 500 to 1000 °C, are correspondingly presented from **Figure 5.11** to **Figure 5.16**. By adhering to the Gaussian–Lorentzian mixed shape, two deconvoluted Raman peaks locate at around 1346 cm⁻¹ and 1580 cm⁻¹ are attributed to *D* peak and *G* peak, respectively [86]. The extract peak position of *D* peak and *G* peak for each carbonized PAN samples is listed in **Table 5.3**. Having both *D* peak and *G* peak signifies that the PAN derived CNFs possessing a turbostratic structure. It is revealed that the imperfect microstructural nature of carbonized PAN NFs, including poor alignment of basal planes, various defects and dislocations [49].

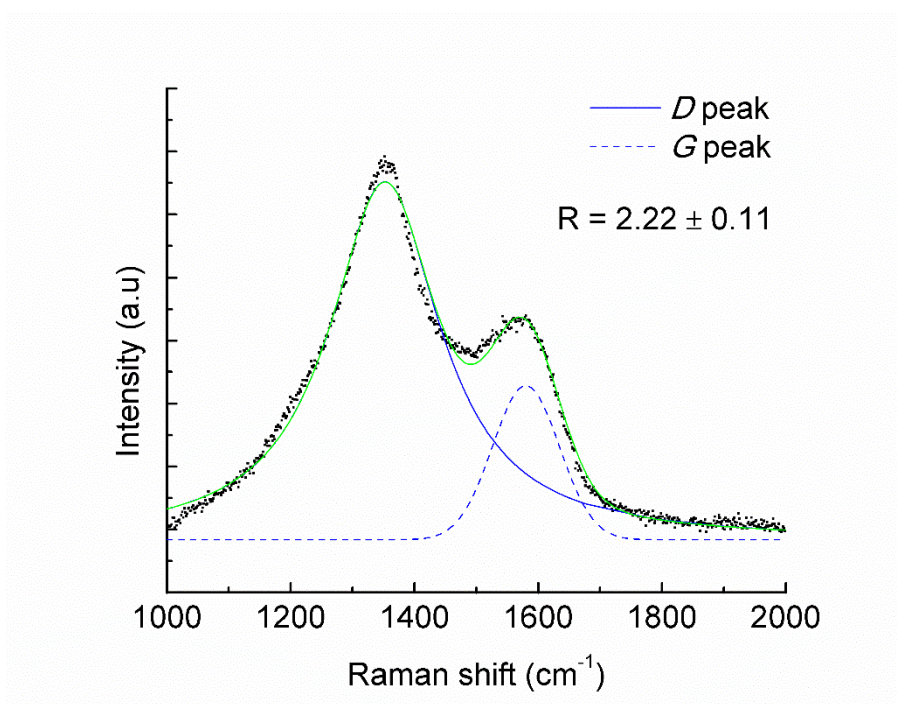


Figure 5.11 Raman spectrum of sample CNF-500.

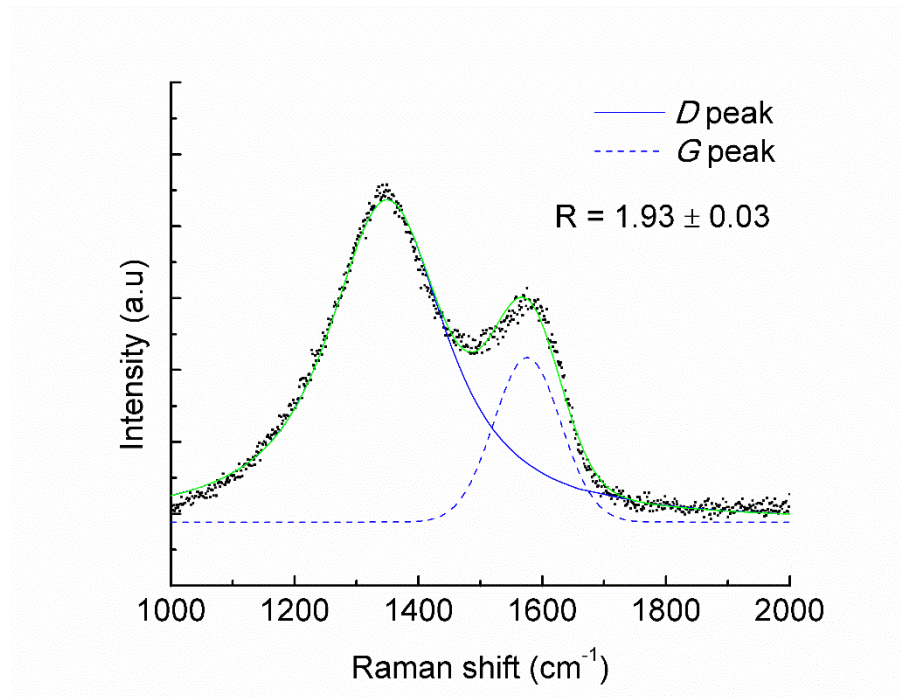


Figure 5.12 Raman spectrum of sample CNF-600.

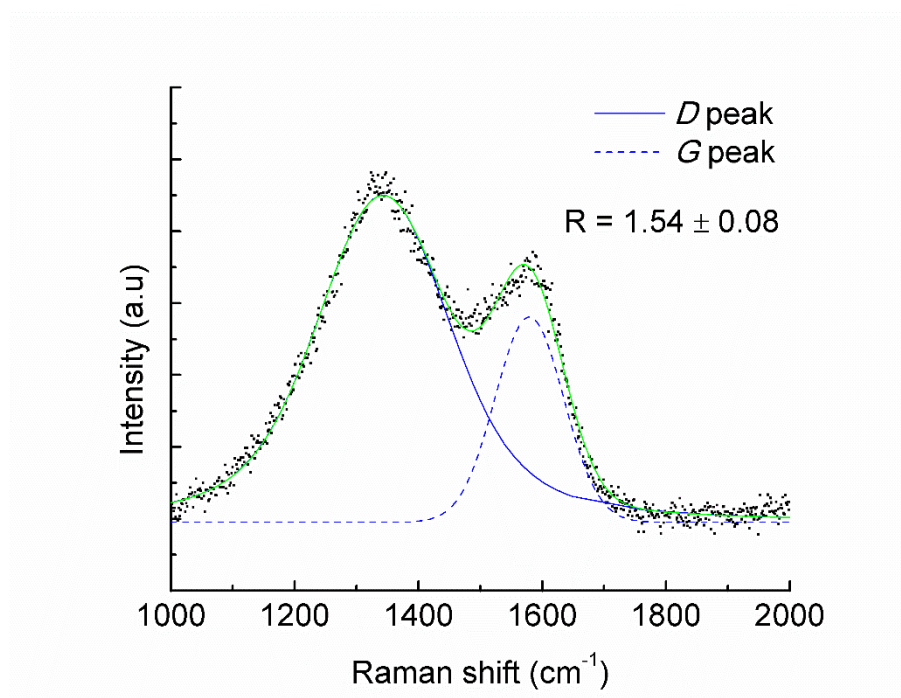


Figure 5.13 Raman spectrum of sample CNF-700.

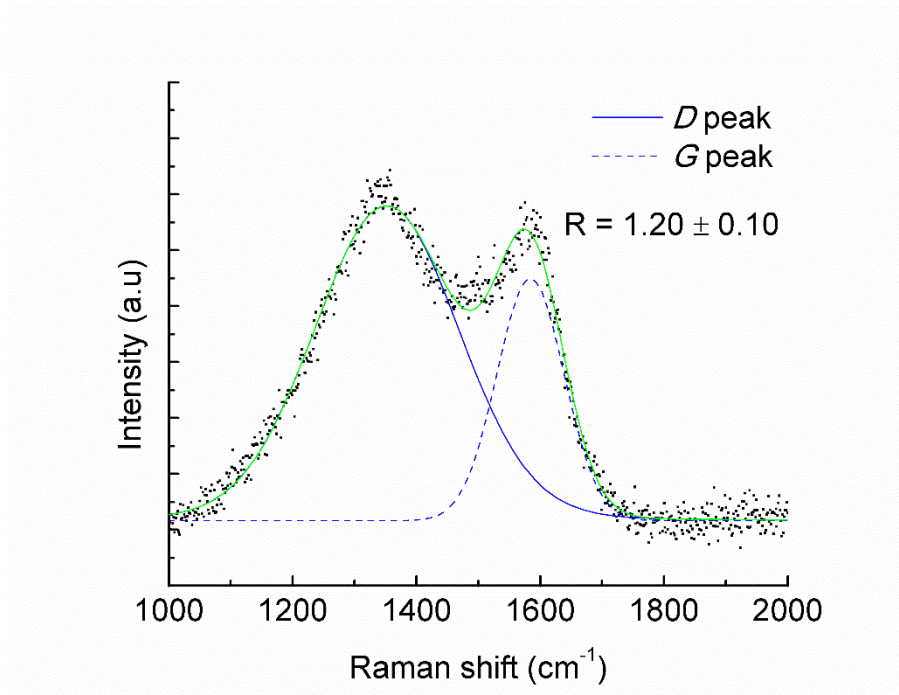


Figure 5.14 Raman spectrum of sample CNF-800.

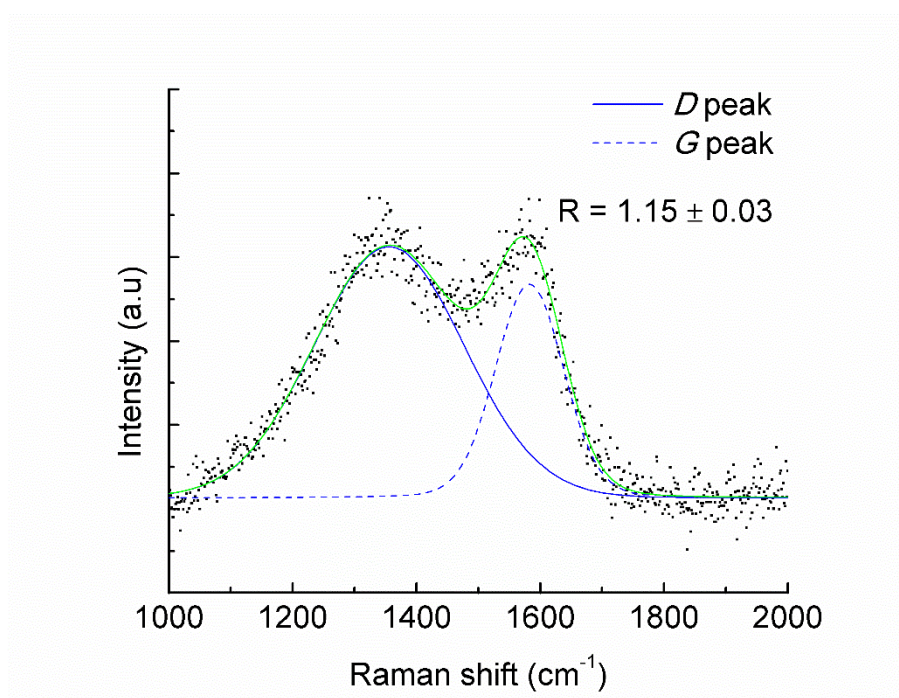


Figure 5.15 Raman spectrum of sample CNF-900.

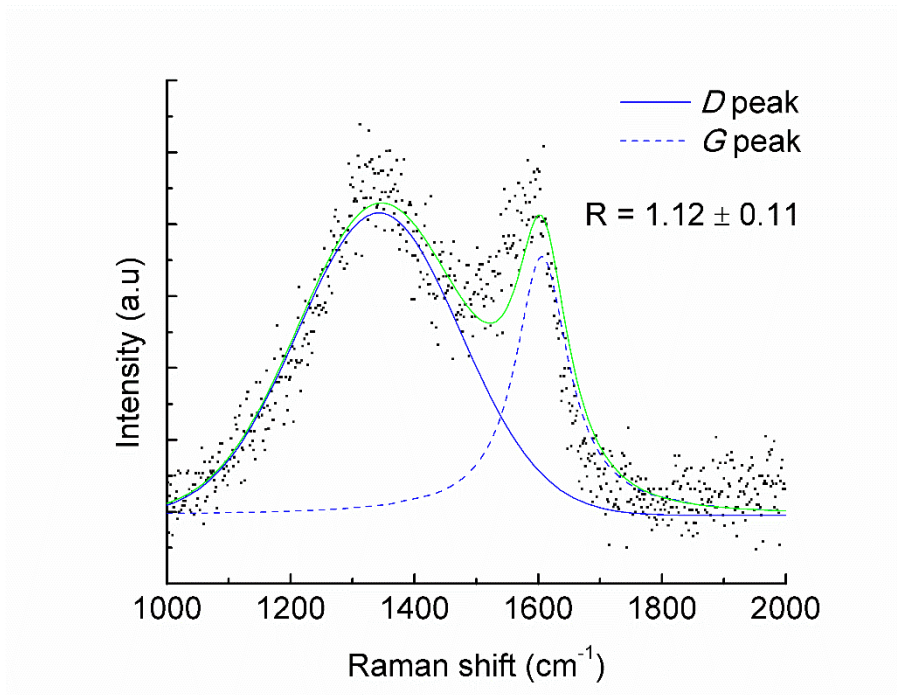


Figure 5.16 Raman spectrum of sample CNF-1000.

Table 5.3 Summary of details extracted from Raman spectra of CNFs carbonized with various carbonization temperatures, ranging from 500 to 1000 °C.

Sample	ν_D (cm ⁻¹)	ν_G (cm ⁻¹)	<i>R</i> -value	L_a (nm)	x_G
CNF-500	1351 ± 4	1576 ± 3	2.22 ± 0.11	2.62 ± 0.13	0.30 ± 0.01
CNF-600	1346 ± 3	1577 ± 1	1.93 ± 0.03	3.01 ± 0.05	0.34 ± 0.00
CNF-700	1347 ± 3	1574 ± 10	1.54 ± 0.08	3.77 ± 0.21	0.39 ± 0.01
CNF-800	1342 ± 18	1586 ± 5	1.20 ± 0.10	4.84 ± 0.42	0.45 ± 0.02
CNF-900	1350 ± 5	1578 ± 6	1.15 ± 0.03	5.06 ± 0.12	0.47 ± 0.01
CNF-1000	1347 ± 14	1592 ± 4	1.12 ± 0.11	5.24 ± 0.65	0.47 ± 0.02

As observed in all presented Raman spectra of CNFs, the ratio of *D* peak to *G* peak, denoted as *R*-value is decreased with increasing carbonization temperature from 500 to 1000 °C. It is well-known that the *R*-value is an important parameter to evaluation the graphitization degree of CNFs. By using the empirical equation shown in **Equation 2.2** [87], L_a of graphitic crystallite was calculated. It was found that with increasing carbonization temperature the crystallite size is increased from approximately 2.62 to 5.24 nm, as shown in **Figure 5.17** and summarized in **Table 5.3**.

By following the **Equation 3.4**, the mole fraction of graphite, X_G can be obtained. The change of X_G as a function of $1000/T$ was plotted and is shown in **Figure 5.18**. By Ln both side of **Equation 2.4**, as shown in **Equation 2.5**, the new plot of $\ln X_G$ versus $1000/T$ can be obtained and is presented in **Figure 5.19**. The activation energy required for the growth of the graphitic crystallite from 2.62 to 5.24 nm with increasing 500 to 1000 °C was 7570 J/mol.

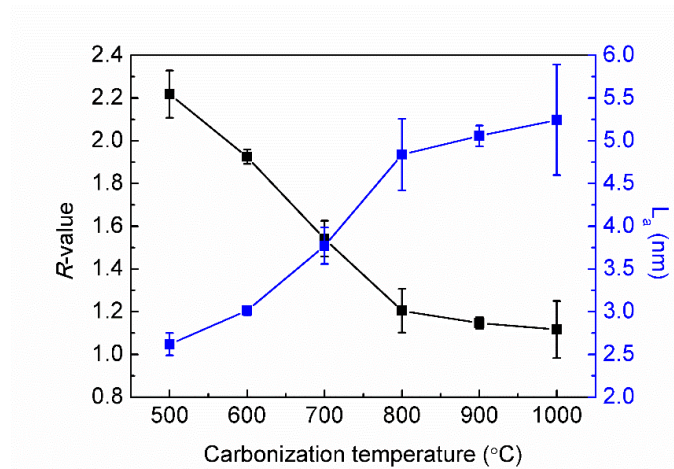


Figure 5.17 *R*-value and L_a of CNFs as function of carbonization temperature.

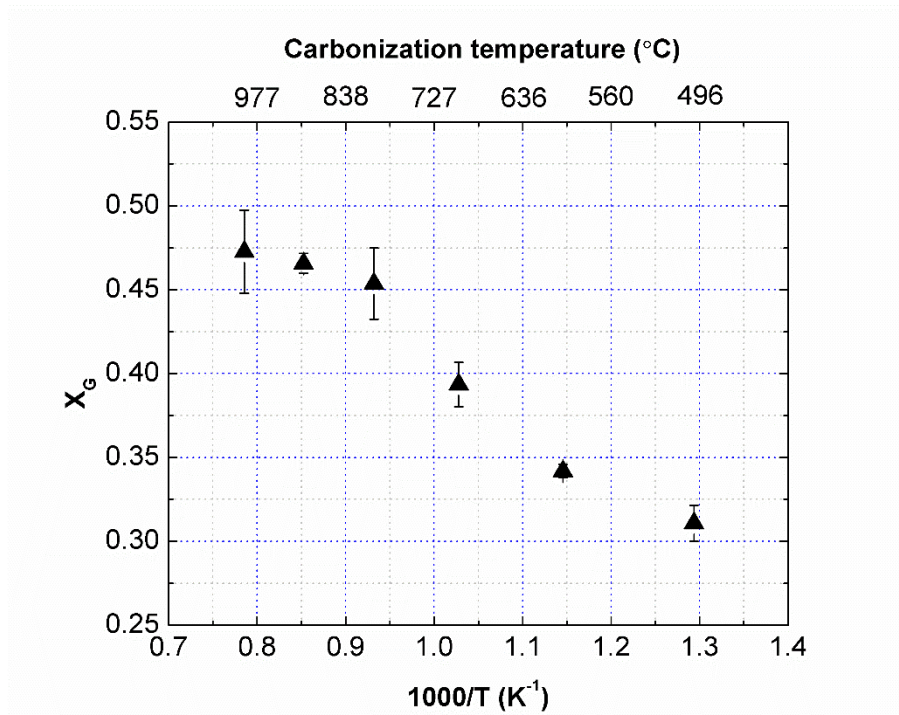


Figure 5.18 The relationship between X_G and $1000/T$.

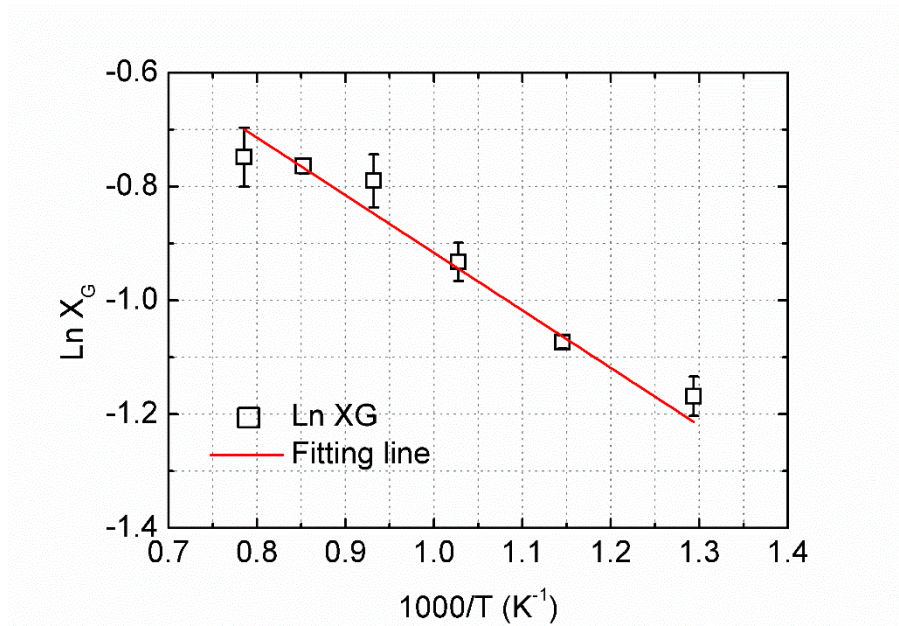


Figure 5.19 The relationship between $\text{Ln } X_G$ and $1000/T$.

5.4 TEM

To further characterize carbonized PAN NFs (i.e. denoted as CNFs) with various carbonization temperatures, ranging from 500 to 1000 °C, the low magnification TEM images with selected area electron diffraction (SAED) patterns are summarized in **Figure 5.20**. It can be seen that the morphology of the CNFs is smooth which is highly resemble to the ones observed by SEM images shown in **Figure 5.3-5.8**. In addition, the similar trend on the fibre diameter with increasing carbonization temperature from 500 to 1000 °C is also noticed. More interestingly, with increasing carbonization temperature the SAED pattern of the CNFs is developed from a very diffusive type to a well-defined ring type. This development observed in the SAED patterns reveals that degree of crystallinity of the CNFs was increased.

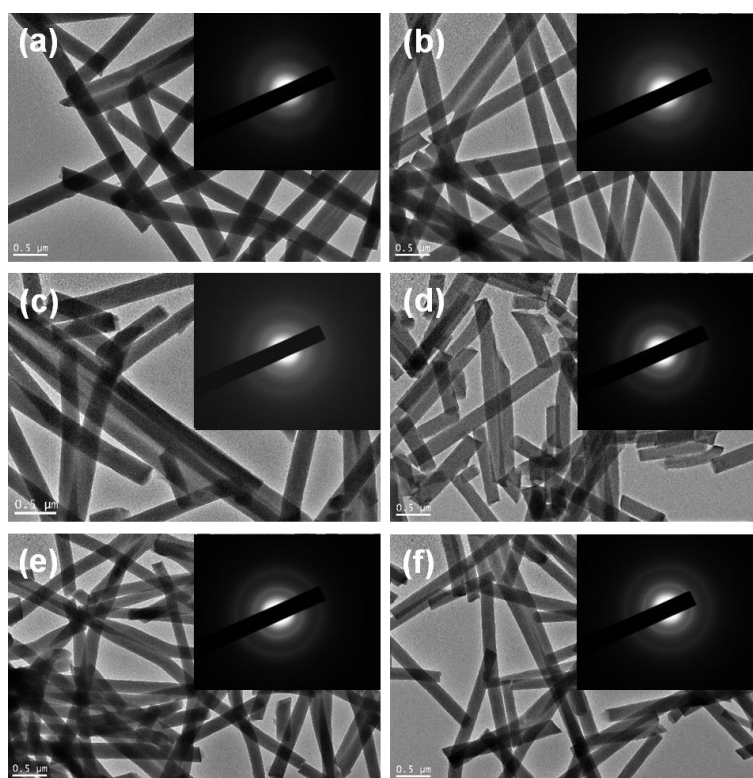


Figure 5.20 Low magnification TEM images of CNFs with various carbonization temperatures from 500 to 1000 °C: (a)-(b) CNF-500, (c)-(d) CNF-600, (e)-(f) CNF-700, (g)-

(h) CNF-800, (i)-(j) CNF-900 and (k)-(l) CNF-1000. The SAED patterns of CNFs are inserted at top right corner.

To get closer look of the morphology or microstructure of the CNFs, high resolution TEM (HRTEM) characterisation was carried out and their HRTEM images are shown in **Figure 5.21**. The main matrix of the fibre is seen to be made of amorphous in nature. Nevertheless, small portion of crystalline phase is noticed locating at surface layer of the fibre as well as randomly scattered distributing within the core of the fibre.

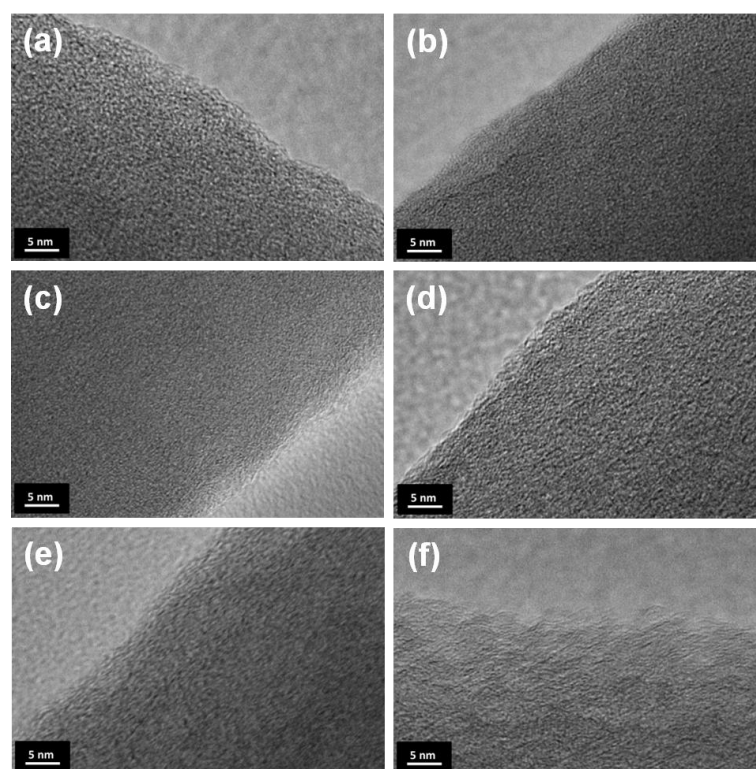


Figure 5.21 HRTEM images of CNFs with various carbonization temperatures from 500 to 1000 °C: (a) CNF-500, (b) CNF-600, (c) CNF-700, (d) CNF-800, (e) CNF-900 and (f) CNF-1000.

5.5 Impedance spectroscopy

Impedance spectra of four CNFs heat treated at carbonization temperatures ranging from 500 to 800 °C, in the form of Cole-Cole plots, are presented in **Figure 5.22-Figure 5.25**. By utilizing an approach similar to that described in the previous studies, the Cole-Cole plots can be fitted using four different equivalent electrical circuits [95, 107, 108]. The complex impedance can be expressed by using **Equation 2.6**.

Figure 5.22 shows the Cole-Cole plot of PAN derived CNFs formed at a carbonization temperature of 500 °C. This plot features an arc-shaped curve, which indicates the presence of an R_pC parallel component within the equivalent circuit. After fitting the Cole-Cole plot, the inserted circuit in **Figure 5.22** can be used to describe the dielectric behaviour as shown in **Equation 3.1**. R_pC parallel circuit represents the internal conduction path between the electrodes.

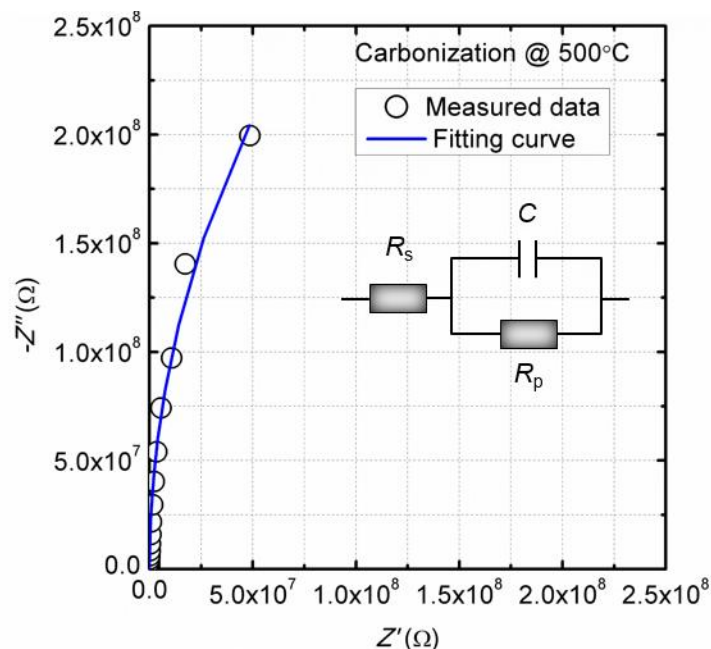


Figure 5.22 Cole-Cole plot of sample CNF-500. The electrical circuit of $R_s(R_p//C)$ generated from the fitting curve is inserted as inset.

As the carbonization temperature increases to 600 °C, the shape of the Cole-Cole plot alters to form a distorted semicircle, which implies that the capacitive element is behaving as a non-ideal capacitor. In this situation, the capacitance within R_pC parallel circuit will be replaced by constant phase element (CPE). Thus, the fitting curve of Cole-Cole plot for sample CNF-600 in **Figure 5.23** follows **Equation 3.2**. In **Equation 3.2**, Q is the pre-factor of CPE, and n is exponent, which can vary from 0 to 1 to represent the electrical circuit element changed from ideal resistor to ideal capacitor. As illustrated for sample CNF-500 in **Figure 5.22**, **Equation 3.1** can be used to best fit the Cole-Cole plot. Indeed, **Equation 3.1** is a simplified version of **Equation 3.12** where $n = 1$ and CPE acts as an ideal capacitor.

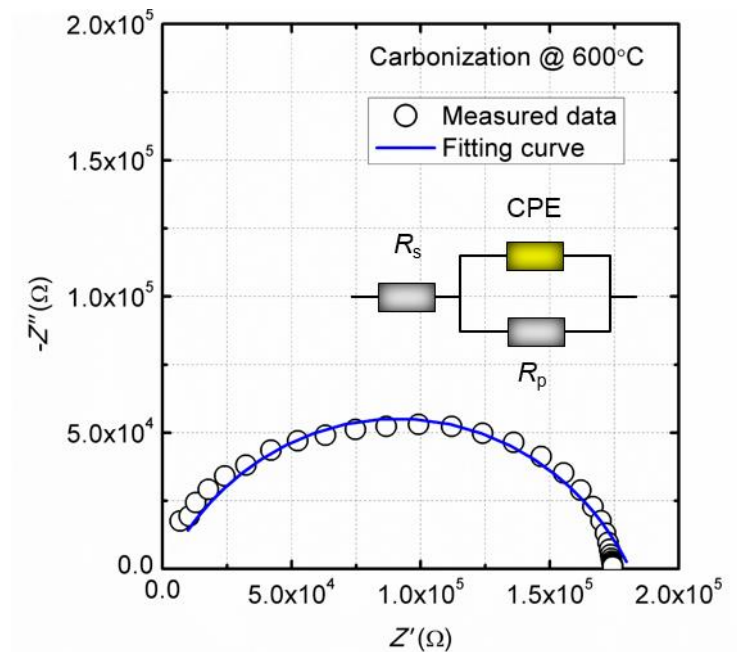


Figure 5.23 Cole-Cole plot of sample CNF-600. The electrical circuit of $R_s(R_p//CPE)$ generated from the fitting curve is inserted as inset.

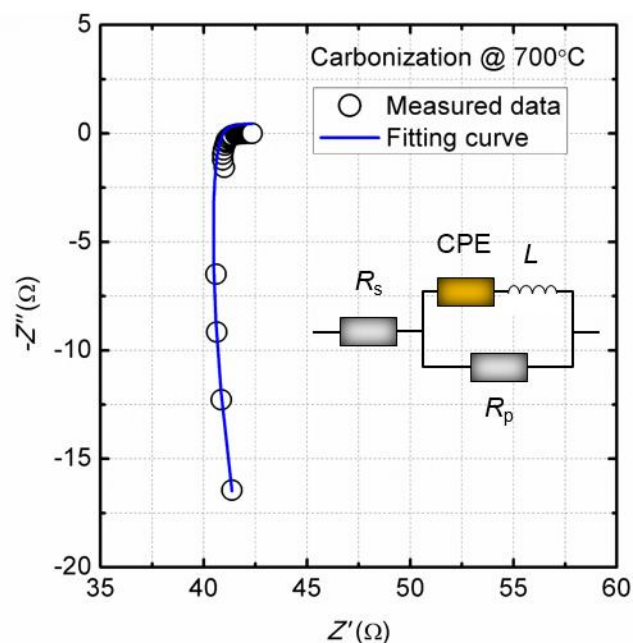


Figure 5.24 Cole-Cole plot of sample CNF-700. The electrical circuit of $R_s(((CPE)(L))//R_p)$ generated from the fitting curve is inserted as inset.

By further increasing the carbonization temperature to 700 °C, the measured impedance data of sample CNF-700 in **Figure 5.24** exhibits a shape similar to candy cane, which is situated at Quadrant IV of the Cole-Cole plot. The appearance of impedance data at this particular position on the Cole-Cole plot indicates the emergence of inductive element and a CPE with residual capacitive effect. The fitting curve thus can be described by using **Equation 3.3**.

When the carbonization temperature reaches 800°C, the ‘handle’ part of the ‘candy cane’ disappears, whereas the ‘stick’ part is slightly tilted on Quadrant IV of the Cole-Cole plot, as presented in **Figure 5.25** for sample CNF-800. As observed from previous three PAN derived CNFs, the capacitive effect of CPE element is deteriorating with increasing carbonization temperature, the fitting curve for sample CNF-800 can be described using **Equation 3.4**.

The fitting curves were optimized to better fit the plot by tuning the numerical values of electrical circuit elements for each mathematical model, as described in **Equation 3.1** to **Equation 3.4**.

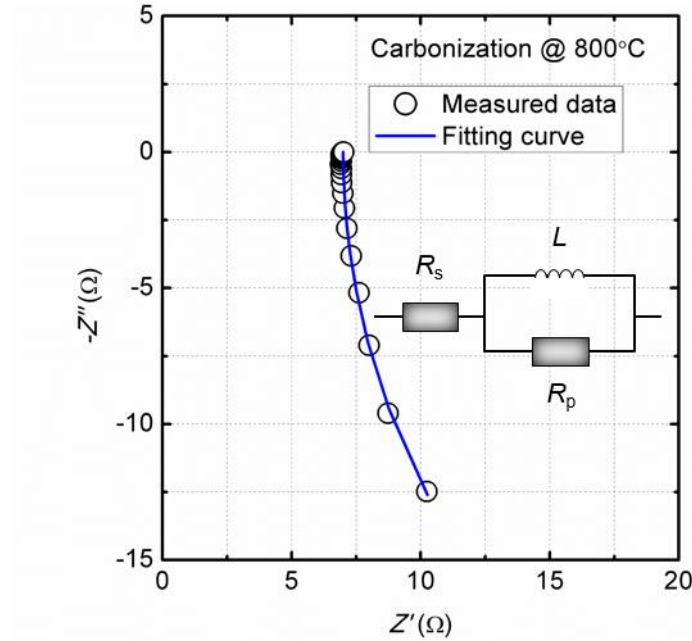


Figure 5.25 Cole-Cole plot of sample CNF-800. The electrical circuit of $R_s(R_p//L)$ generated from the fitting curve is inserted as inset.

The selected numerical values of electrical circuit elements for each electrical circuit and its associated fitting errors are summarized in **Table 5.4**.

Table 5.4 Numerical values of electrical circuit elements extracted from the fitting of Cole-Cole plots by using Matlab.

Sample	R_a	R_p	C	CPE		L	Error (%)
				Q	n		
CNF-500	2.49 k Ω	0.91 G Ω	7.38 pF	-	-	-	5.85
CNF-600	1.1 k Ω	0.18 M Ω	-	1 nMho	0.7	-	5.26
CNF-700	34.9 Ω	249 Ω	-	0.1 Mho	0.04	2.82 μ H	1.32
CNF-800	7 Ω	52 Ω	-	-	-	2.14 μ H	0.81

Error is defined as $\frac{1}{n} \sum_{i=0}^n \left(\sqrt{(x_i^2 - Re_i^2)^2 + (y_i^2 - Im_i^2)^2} / \sqrt{(Re_i^2 + Im_i^2)} \right)$, where x_i and y_i are the fitting data on real and imaginary part of impedance. Re_i and Im_i represent the measured impedance data. i is the total measurement point.

In order to develop a thorough understanding on the dielectric transition of carbonized PAN fibres formed at different carbonization temperatures ranging from 500 to 800 $^{\circ}$ C, a firm grasp of the microstructural evolution of PAN fibres during the carbonization process is critical. Considering two fabrication procedures of PAN derived CNFs before carbonization, quicker solvent evaporation on the fibre surface during the electrospinning and oxygen diffusion-controlled of stabilisation process both encourage the formation of skin-core structure [74]. In recent TEM studies, Rafique *et al* and Hendi *et al*. have confirmed that the PAN derived CNFs possess a skin-core structure, which has better graphitized surface layer, whereas the inner part is composed of both graphitic layers and amorphous area [71, 109]. On the other hand, several pioneering studies have suggested that carbonized PAN fibres can be viewed as a composite material [110], which has matrix phase made of uncarbonized intermediate phases with pores, and a dispersed phase

formed by a chaotic collection of graphitic layers [111]. Indeed, such skin-core structure is gradually developed from sample CNF-500 to CNF-800, as shown in **Figure 5.22-5.25**. By comparing to the reported one [71], the less pronounced graphitic layers observed in the current cases are attributed to the combining effect of lower carbonization temperatures and thicker PAN NFs. Based on these findings, **Figure 5.22** shows a simplified microstructural model of PAN derived CNFs formed at carbonization temperatures from 500 to 800 °C, as proposed for the current investigation. In **Table 5.4**, the contact resistance R_s and parallel resistance R_p of PAN derived CNFs is monotonically decreased from 2.49 k Ω and 0.91G Ω to 7 Ω and 52 Ω , as carbonization temperature increased from 500 to 800 °C. For the fibers carbonized at 500 °C, a parallel R_pC circuit has been fitted from the Cole-Cole plot as shown in **Figure 5.22**. The capacitance extracted from Cole-Cole plot is at picofarad level, which indicates the dielectric nature of sample CNF-500. This is likely due to the formation of low concentration of conducting phases, including isolated graphitic layers and amorphous carbon, as evidenced by the presence of both D peak and G peak of Raman spectra in **Figure 5.11-5.16**. They are randomly dispersed within the uncarbonized intermediate phases, as illustrated in **Figure 5.26**. Considering there is only one R_pC parallel component for sample CNF-500, it is reasonable to conclude that the weak conduction is likely attributed to the limited portion of conductive phases within the junction of entangled PAN derived CNFs. Although the partial carbon conversion unavoidably occurs at the carbonization temperature of 500 °C, the parallel resistance R_p at \sim G Ω level indicates that the electrical conduction is impeded by the uncarbonized intermediate phases, while the low concentration of conducting phases has little effect in improving the electrical conduction. As the carbonization temperature increased to 600 °C, apart from the reduction on both R_s and R_p , the capacitive element is deteriorated to a CPE with n value decreased from 1 to 0.7, calculated from the suppressed semicircle for sample CNF-600 presented in **Figure 5.23**. Similar Cole-Cole plot shape was reported by Wang *et al.* for 19wt% CB filled HDPE composite [98]. The high similarity of current data to the reported one confirms that there are still a substantial amount of uncarbonized phase existed within the PAN derived CNFs at such carbonization temperature. While the decrease in I_D/I_G ratio observed in Raman spectra (shown in from **Figure 5.11** to **Figure**

5.16) indicates that the increasing concentration of graphitic layers. These observations suggest that the carbonization occurs at low carbonization temperatures is a rather complex and dynamic process, which likely involves the conversion between uncarbonized phase to carbonized/conducting phase concurrently associated with the conversion from amorphous carbon to crystalline carbon. With further increasing carbonization temperature to 700 °C more severe deterioration of capacitive element can be observed, as n value of CPE is further decreased to 0.04. The n value here is approaching zero, whose contribution therefore can be approximated to a pure resistance qualitatively. The increasing concentration of conducting phases makes the capacitive element less dominant and the electrical conduction much significant. This is supported by observing newly formed inductive element in the Cole-Cole plot of sample CNF-700, implying the establishment of an electrical conduction network formed by bridging the conducting phases throughout the fibre. Thus, the inductance is a considered to be originated from the interaction/interference of numerous tangled PAN derived CNFs, as witnessed by SEM images. When the carbonization temperature reached to 800 °C, only one parallel R_pL circuit is observed, which is due to the very high concentration of conducting phases, while the uncarbonized intermediate phases are either vanished or reduced to a very small amount that is below the detecting limit of impedance spectroscopy.

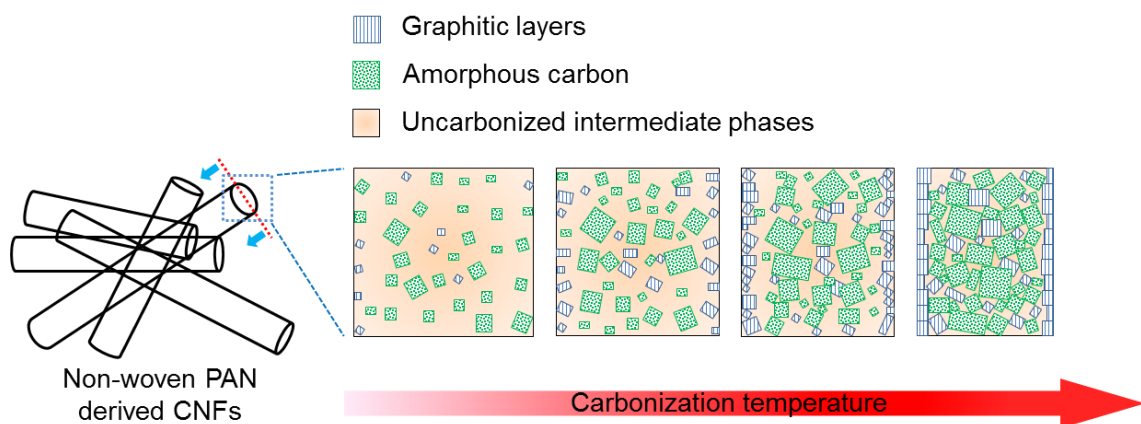


Figure 5.26 Qualitative illustration of showing the microstructural evolution during the carbonization process as a function of carbonization temperature.

5.6 Summary

In summary, with increasing carbonization temperature from 500 to 800 °C, the R_s and R_p have decreased significantly from 2.49 k Ω and 0.91 G Ω to 7 Ω and 52 Ω , respectively. In the meantime, the carbonized PAN NFs have transitioned from being insulating to electrically conducting in nature, and the subsequent equivalent circuit has changed from being R_pC parallel circuit dominant to R_pL parallel circuit dominant. With the assistance of SEM and Raman results, a microstructural evolution model is proposed to understand the progressive dielectric transition of PAN derived CNFs at different carbonization temperatures. The findings of this work have enlightened the possibility for impedance spectroscopy to be employed as a non-destructive technique to monitor the carbonization degree of carbon fibres during the industrial manufacturing process. The main part of the results presented in this chapter has been published in reference [112].

6 Fabrication and Characterisations of CNWs-CNFs Hybrid Material

6.1 Morphology

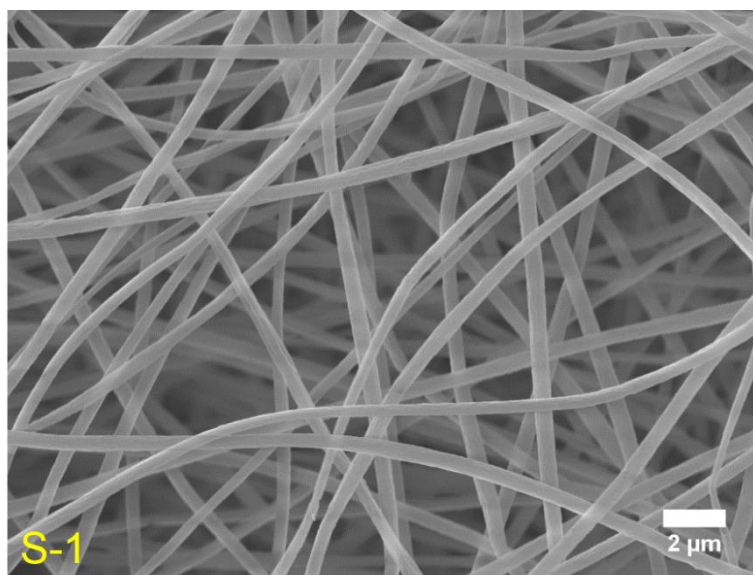


Figure 6.1 SEM image of electrospun PAN NFs.

Figure 6.1 shows the morphology of the electrospun PAN NFs, which showed no sign of beads with average diameter (d_a) of 431 ± 67 nm. As summarized in **Table 6.1**, a gentle reduction on d_a from approximately of 431 to 409 nm after stabilisation process, while no significant change in the terms of the shape of the fibres was observed in in **Figure 6.2**.

Table 6.1 Summary of average diameter of PAN NFs heat treated at various conditions.

Sample	Figure No.	Description	d_a (nm)
S-1	6.1	Electrospun PAN NFs	431 ± 67
S-2	6.2	Stabilized PAN NFs	409 ± 46
S-3	6.3	Furnace carbonized PAN NFs	347 ± 42
S-4	6.4	MPECVD carbonized PAN NFs	362 ± 57
S-5	6.5	MPECVD grown CNWs on the surface layers of the CNFs	1834 ± 228
S-6	6.6	MPECVD grown CNWs on the deeper layers of the CNFs	392 ± 46

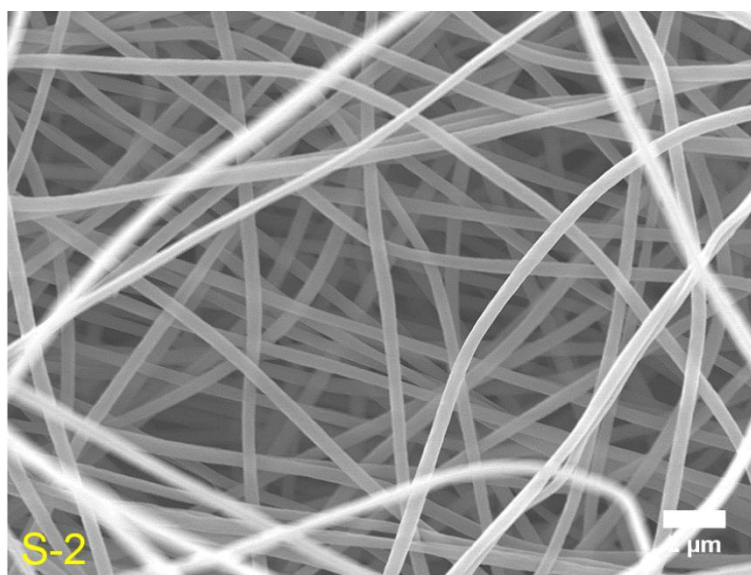


Figure 6.2 SEM image of stabilised PAN NFs.

It was reported by Ko, who stated that the water vapour was evaporated during the stabilisation [78]. This could be the reason that responsible for the reduced d_a observed in sample S-2. Along with the colour change from white to dark brown after stabilisation evidenced in **Figure 3.4**, the infusible ladder like polymer structure was likely established within the stabilised PAN NFs [74, 113-115].

To further confirm this point, no melting was observed in the carbonized PAN NFs fabricated from two different methods: conventional furnace in **Figure 6.3** and microwave plasma enhanced chemical vapour deposition (MPECVD) in **Figure 6.4**.

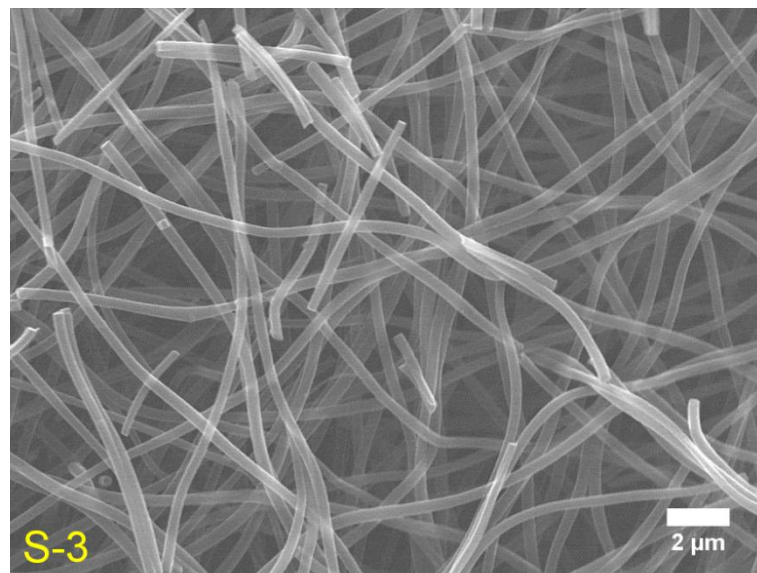


Figure 6.3 SEM image of carbonized PAN NFs by using conventional furnace.

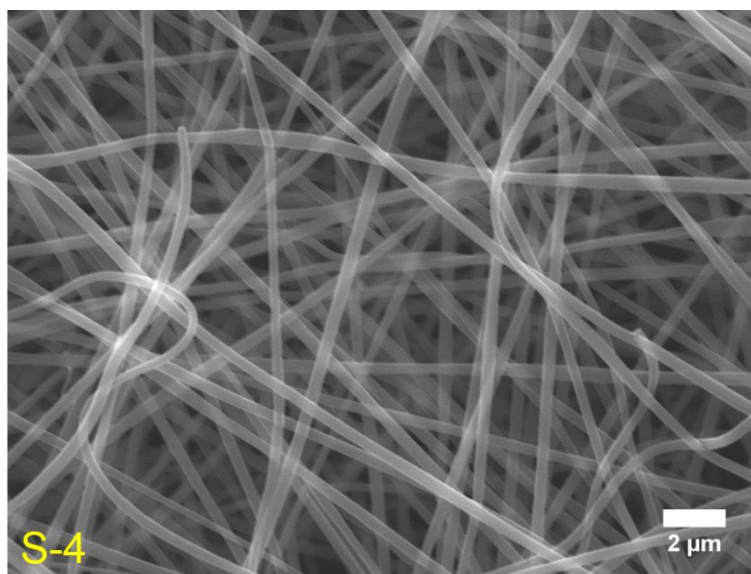


Figure 6.4 SEM image of bottom side of carbonized PAN NFs by using MPECVD.

It can be seen that d_a was decreased from approximately 409 to 347 nm in **Figure 6.3** observed for the furnace carbonized PAN NFs (S-3). In the case with MPECVD carbonized PAN NFs (S-4), fibre diameter was found decreasing from 409 to 362 nm in **Figure 6.4**. It is a general knowledge that during the carbonization process, the non-carbon substances were evolved in the form of various gases, hence leaving the carbon content only within the fibres [55]. More specifically, Donnet and Bahl noticed the amount of the evolved gas during the carbonization process was increased with increasing carbonization temperature [77]. Ko found the concentration of non-carbon elements, H₂, O₂ and N₂ within the carbon fibres were decreased with increasing carbonization temperature, while carbon content was increased [58]. It was noticed that the fibre diameter reduction on S-3 was more serve than S-4. Similar observations were reported by other authors, who stated that the smaller diameter was resulted from higher carbonization temperature [74, 76]. Thus, it is reasonable to speculate that the fibre reduction difference in current study might implies the slight temperature difference between the one used in MPECVD and in conventional furnace. Nevertheless, the temperature difference might not be the only reason responsible for it. The other factors, such as different physical and chemical nature of these two

carbonization processes can also be considered as alternative reason to lead the fibre discrepancy between sample S-3 and S-4.

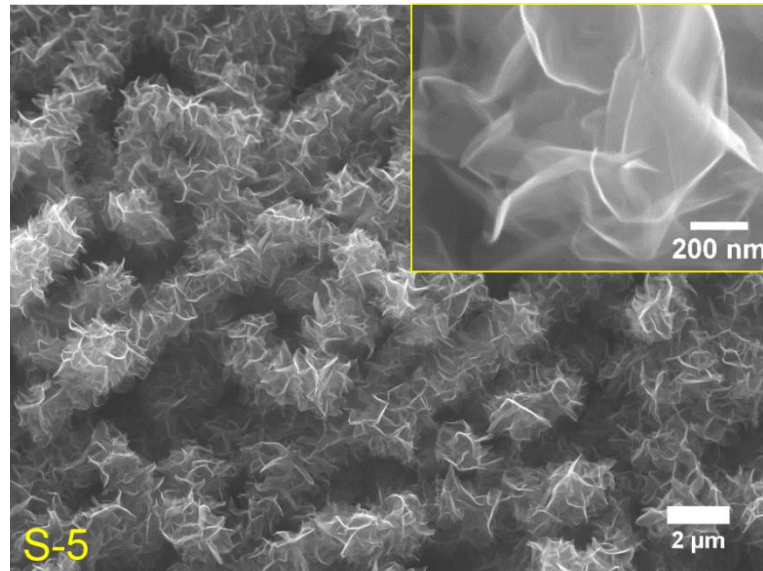


Figure 6.5 SEM image of top side of carbonized PAN NFs with CNWs grown by MPECVD. The closer view of CNWs grown on the top side captured at higher magnification is inserted as an inset.

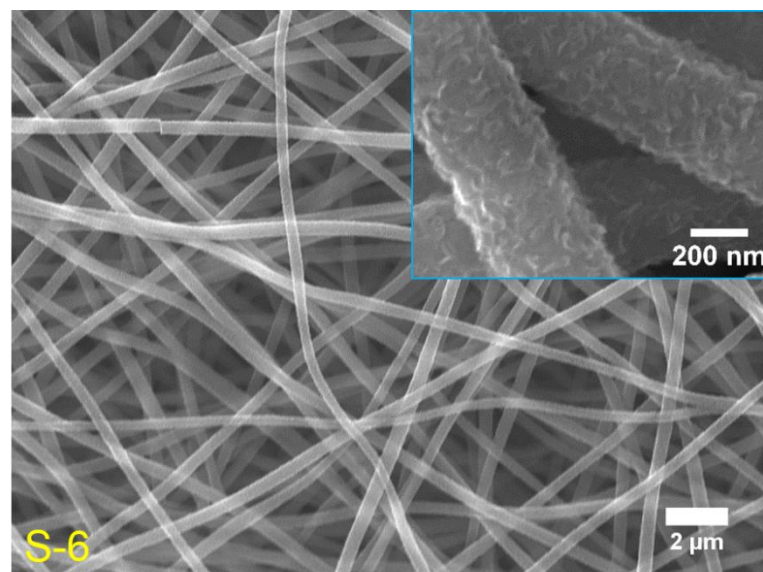


Figure 6.6 SEM image of bottom side of carbonized PAN NFs with CNWs grown by MPECVD. The closer view of CNWs grown on the bottom side captured at higher magnification is inserted as an inset.

As shown in **Figure 6.5** and **Figure 6.6**, by using MPECVD method apart from the carbonization of stabilised PAN NFs in **Figure 6.4**, layers of carbon species were found deposited on the carbonized PAN NFs. The carbon species obtained in this study has been reported elsewhere [104, 116-119], known as carbon nanowalls (CNWs). In **Figure 6.5**, it can be seen that CNWs were radically grown perpendicular to the carbonized PAN NFs. Zhu *et al.* reported that in order for the vertical growth of carbon nanosheet (CNS) to occur, the planar nucleation followed by the growth of base layer parallel to the substrate surface was taken place first within 2-4 min [120]. The thickness of the base layer was reported to be 1-15 nm [120]. Wang *et al.* revealed that the CNS with the thickness of less than 1 nm was consisted of two to three graphene layers, by using TEM [121]. In this regard, the CNWs grown at given condition with rough thickness of 6-10 nm estimated from the inset of **Figure 6.5** contain at least 18-30 layers of graphene. Hiramatsu and Hori pointed out that the thickness of the CNWs increased with increasing deposition time [119]. Thus growing CNWs with lesser graphene layers should be readily obtained by decreasing the deposition time [119]. By carefully varying other processing parameters, such as gas reactant ratio, pressure, substrate conditions, the length and the height of CNWs can also be controlled [83, 122]. As the substrate material, CNFs carbonized from non-woven electrospun PAN NFs mat which possessed porous structure. The CNWs formed in **Figure 6.5** look distinctively different from the one shown in **Figure 6.6**, whereas no grown CNWs observed at the bottom side of the sample which was in contact of sample holder, as shown in **Figure 6.4**. Similar trend was previously reported by Lisi *et al.*, who referred this phenomenon as “infiltration” process [91]. It was found that with increasing the depth in the direction from substrate surface to the bottom, the thickness of CNWs was decreased significantly [91]. As shown in the inset of **Figure 6.6**, the dimension of the CNWs is extremely small, and appeared to be similar to the ones observed at the early stage

growth of CNWs [120]. The difference in the obtained morphology between the CNWs grown on the substrate surface and on the deeper area towards to the bottom shown in **Figure 6.7**. This reflected the ability of plasma to penetrate into the CNFs non-woven mat at the given condition. Growing CNWs on porous materials may offer a new way to harvest CNWs with different dimensions and quality. In addition, the deeper investigation on the transition region may provide more insights regarding to the formation of CNWs on CNFs, which will be carried out in the further work.

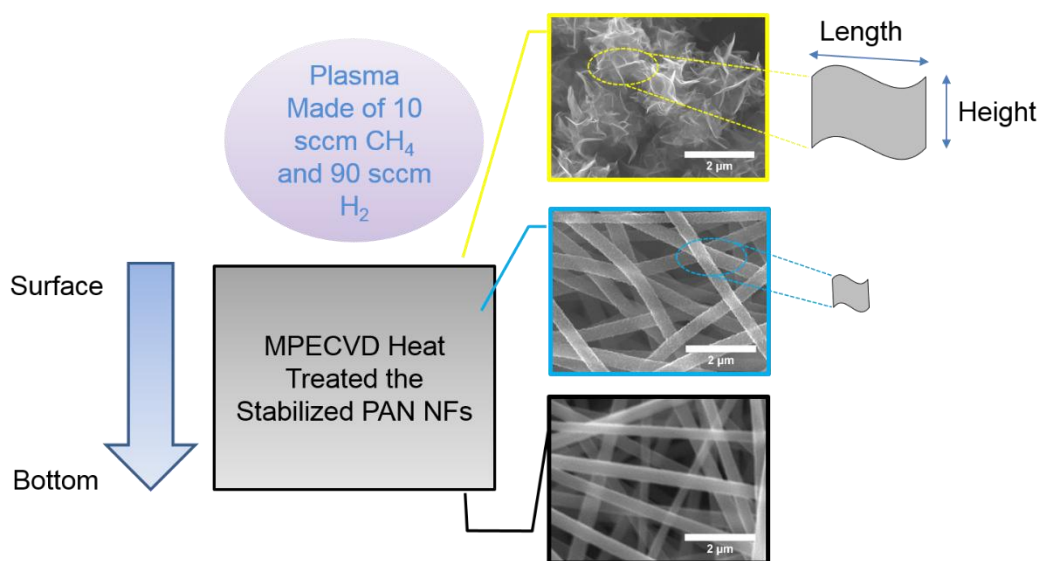


Figure 6.7 Schematic diagram of morphological change of grown CNWs by MPECVD with depth change from the sample surface to the bottom.

6.2 Functional Groups

FTIR spectra of PAN NFs treated with various heat treatments are shown in **Figure 6.8**. Similar functional groups of electrospun PAN NFs observed in **Figure 5.10** were also noticed in the current case.

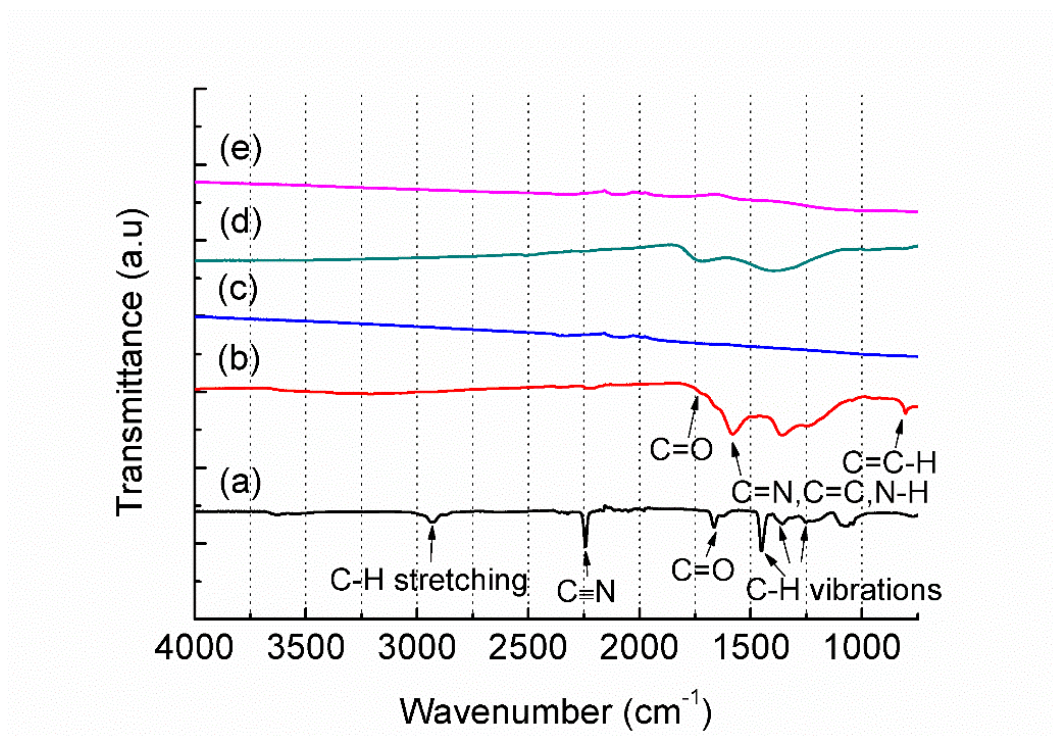


Figure 6.8 FTIR spectra of PAN NFs treated with various treatments: (a) electrospun PAN NFs, (b) stabilised PAN NFs, (c) furnace carbonized PAN NFs, (d) MPECVD carbonized PAN NFs, and (e) MPECVD grown CNWs on CNFs.

As summarized in **Table 6.2**, the characteristic peaks observed in the current electrospun PAN NFs (sample S-1) including nitrile group ($C\equiv N$) located at 2242 cm^{-1} , the aliphatic CH groups (CH , CH_2 and CH_3) appeared at 2937 cm^{-1} , 1453 cm^{-1} , 1359 cm^{-1} , and 1252 cm^{-1} [73, 123, 124], are shown **Figure 6.8(a)**. In addition, a small peak appeared at 1666 cm^{-1} corresponding to $C=O$ bond, is thought to be originated from the residual DMF due to the insufficient solvent evaporation during the electrospinning of PAN NFs [125].

Table 6.2 Assignment of main FTIR peaks of PAN NFs treated with various heat treatments.

Sample	FTIR peak position (cm ⁻¹)					
	C≡N	C-H stretching	C-H vibrations	C=O	C=N, C=C, N-H	C=C-H
S-1	2243	2937	1453, 1359, 1252	1666	-	-
S-2	2227	-	1360, 1247	1710	1582	805
S-3	-	-	-	-	-	-
S-4	-	-	1259	-	1574	-
S-5	-	-	-	-	-	-

After stabilisation, the formation of ladder structure discussed in section 6.1 for **Figure 6.2** was supported by observing following changes in **Figure 6.8(b)**: significant intensity reduction on C≡N and aliphatic CH groups; and the emergence of new peaks at 1710, 1582 and 805 cm⁻¹ assigned to C=O, a mix of C=N, C=C and N-H groups, and C=C-H, respectively [126]. These dramatic changes observed in the stabilised PAN NFs (sample S-2) implied the onset of a series of chemical reactions, cyclization, cross-linking, dehydrogenation, as well as oxidation during the stabilisation process [73, 114].

By subsequently carbonizing the stabilised sample S-2 in the conventional furnace, few functional groups can be resolved in **Figure 6.8(c)**. This implied the formation of turbostratic structure in

the furnace carbonized PAN NFs, sample S-3. In contrast, there are still two broad bands centred at 1574 and 1259 cm^{-1} observed in **Figure 6.8(d)**. Similar appearance of FTIR bands was observed in the furnace carbonized PAN NFs with low carbonization temperature of 600 $^{\circ}\text{C}$ in **Figure 6.10**. The high similarity between these two cases implied that the MPECVD carbonized PAN NFs (sample S-4) is likely possessing the more structural disorders compare with sample S-3. This indirectly supported the speculation made from SEM observations that, the lower temperature was likely involved with the carbonization process taken place in MPECVD chamber in the comparison with the conventional furnace. On the other hand, very few functional groups can be seen on the surface layers where exposed to the plasma (sample S-5) during the carbonization process via MPECVD in **Figure 6.8(e)**, as illustrated in **Figure 3.7**. The difference observed between S-4 and S-5 suggested that the grown CNWs are likely composed of structures with a high ordering level in sample S-5, while S-4 was thought associating with more structural disorders.

6.3 Chemical Structure

The electrospun PAN NFs without any heat treatment exhibited a featureless Raman spectrum, which is observed in **Figure 6.9**. This observation agrees with the reported literatures [104, 106]. The featureless appearance observed in sample S-1 implied that the resulted PAN NFs lacking ordered arrangements of PAN molecules [104, 106]. It was reported that electrospinning technique tend to yield electrospun PAN NFs with low crystallinity, due to following reasons: (i) insufficient crystallization time of PAN molecules before the solvent vaporization; and (ii) the fibre structure frozen-in occurred within a very short in-flight time of the charged jet which is about 1 ms [127].

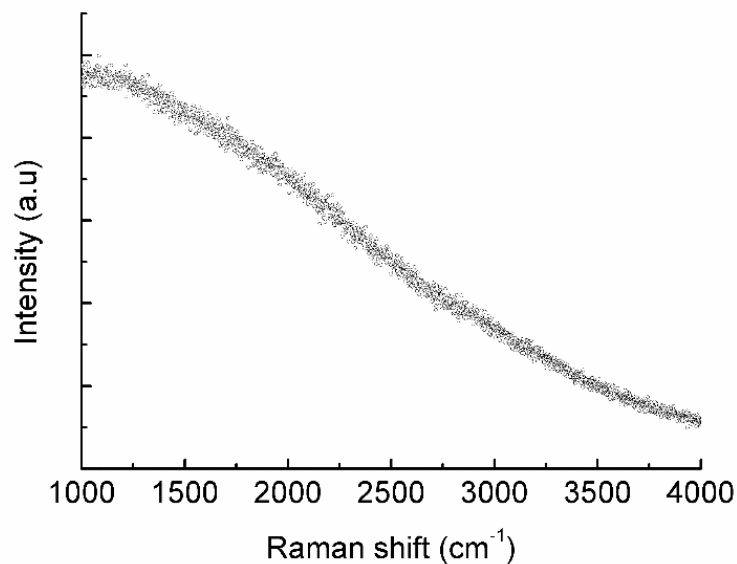


Figure 6.9 Raman spectrum of electrospun PAN NFs (sample S-1).

Figure 6.10 shows the PAN NFs after the stabilisation. It can be seen that there are two main bands observed at 1357 cm^{-1} , and 1571 cm^{-1} , respectively. The former corresponds to *D* peak which is associated with disordered turbostratic structures; whereas the latter corresponds to *G* peak which is attributed to the ordered graphitic structures [74]. The Raman peak position of *D* peak and *G* peak observed sample S-2 was in agreement with the results by Zhang *et al.*, who

reported the *D* peak and *G* peak positioned at 1370 cm^{-1} and 1580 cm^{-1} in the stabilized PAN NFs under the conditions of $300\text{ }^{\circ}\text{C}$ for 30 min [114]. It is commonly known that the intensity ratio of *D* peak (ID) and *G* peak (IG), denoted as *R*-value, can be used to correlate the balance among the disorder and crystalline character within the carbon materials (i.e. higher *R*-value indicates lower crystallinity) [124, 128, 129]. In addition, the crystallite size of graphitic structure, L_a can be obtained by empirical equation shown in **Equation 3.3** [87]. As summarized in **Table 6.3**, the *R*-value calculated for the stabilised PAN NFs (sample S-2) was around 2.40.

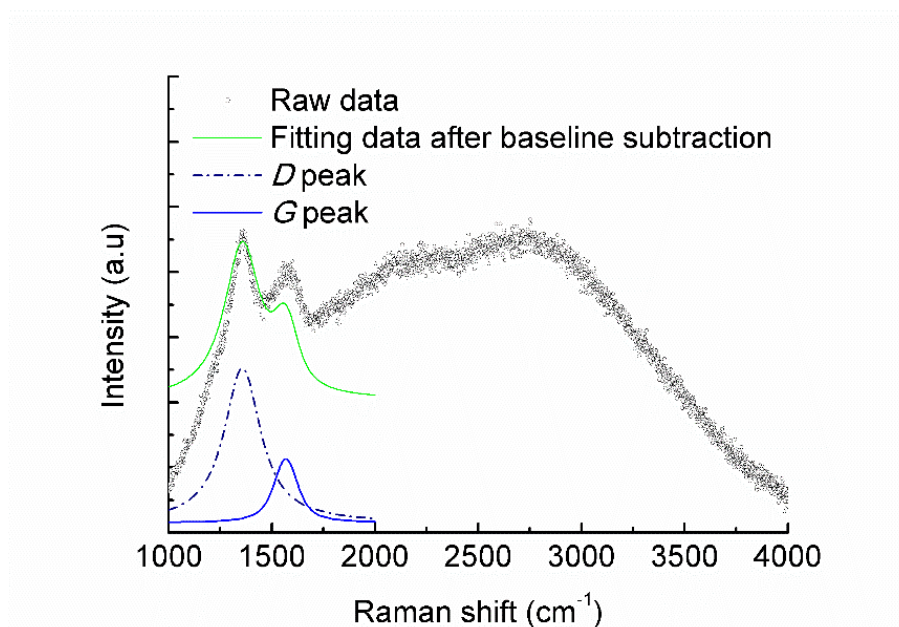


Figure 6.10 Raman spectrum of stabilised PAN NFs (sample S-2).

Figure 6.11 shows the Raman spectrum of the furnace carbonized PAN NFs (sample S-3). It can be seen that both *D* band and *G* band are present with the reduction of *R*-value from approximately 2.40 to 1.29. The decrease in *R*-value suggested that the increased crystallinity of the carbon structures was developed through the carbonization process. The crystallite size of L_a calculated for sample S-3 was $\sim 4.51\text{ nm}$. In addition, there is a broad band centered at 2814 cm^{-1} assigned to *G'* [81].

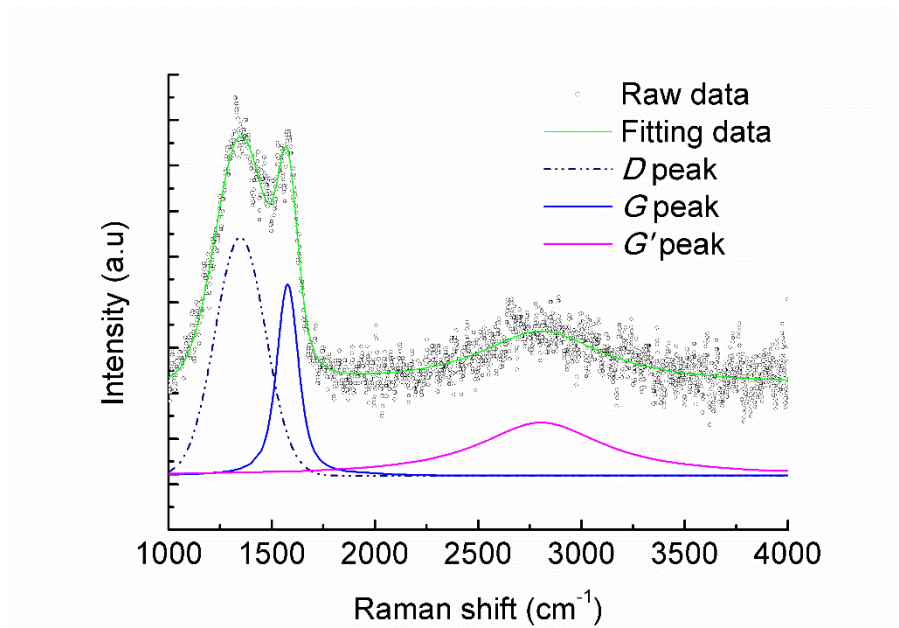


Figure 6.11 Raman spectrum of furnace carbonized PAN NFs (sample S-3).

Figure 6.12 shows the Raman spectrum of the MPECVD carbonized PAN NFs (sample S-4). By comparing the Raman spectra of sample S-3 and sample S-4, it can be observed that the position of *D* peak, *G* peak and *G'* peak were shifted from 1351 cm⁻¹, 1577 cm⁻¹, and 2814 cm⁻¹ to 1338 cm⁻¹, 1584 cm⁻¹, and 2793 cm⁻¹. It was reported that the decrease in the graphitization degree of the resulted carbon materials led to the increase in the wavenumber of *G* peak [130]. In the meantime, the larger *R*-value of ~1.70 was obtained in sample S-4, confirming that resulted CNFs from PAN NFs by using MPECVD at given condition possessed low degree of crystallinity. The calculated *L_a* sample S-4 was 3.42 nm.

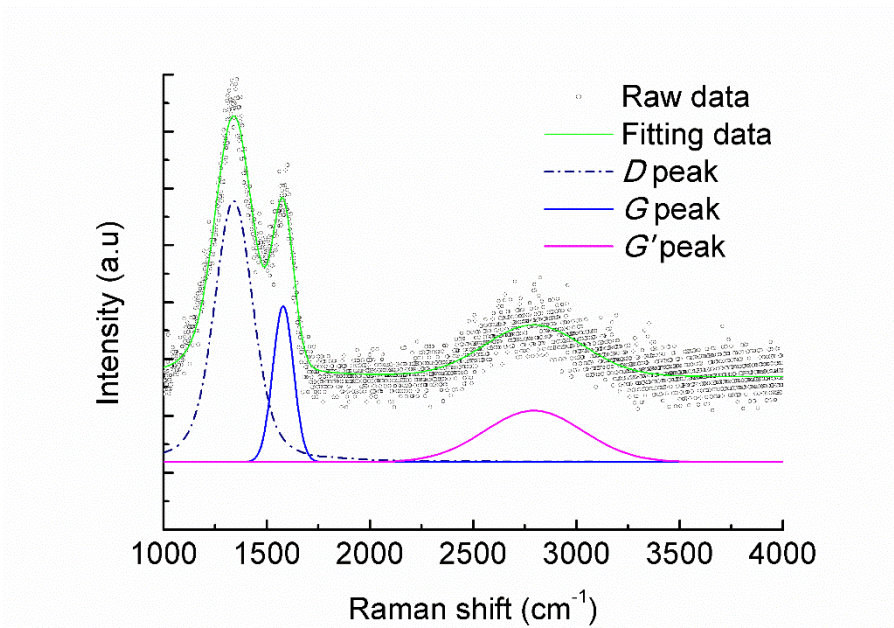


Figure 6.12 Raman spectrum of MPECVD carbonized PAN NFs (sample S-4).

Figure 6.13 shows the Raman spectrum of the CNWs grown on surface layers of CNFs by using MPECVD. It can be seen that with the CNWs grown on the surface layers of CNFs shown in **Figure 6.5**, all three peaks were shifted to the lower wavenumbers at 1328, 1581 and 2664. In addition, the sharpness of all peaks were greatly improved. This is particularly obvious for G' , which transformed from a broad band into a well-defined peak. It was reported that the second-order Raman peak around at 2664 cm^{-1} observed for the highly ordered structure [83]. The highly ordered structure is normally associated with very small R -value [131]. R -value obtained for sample S-5 was 0.66, in turn yielded L_a of 9.30 nm. It should be mentioned that the CNWs normally associated with D' appeared at 1620 cm^{-1} [83, 122]. The very high noise to signal ratio made the determination of such peak impossible in the current study. Although the peak fitting was not performed on D' peak, it is not ruling out the possibility that the presence of D' peak was vague by the high noise to signal ratio. By using the same method in our previous investigation, such peak was resolved along with other second-order Raman features under the Raman spectroscopy which was radiated by using excitation wavelength of 532 nm [104].

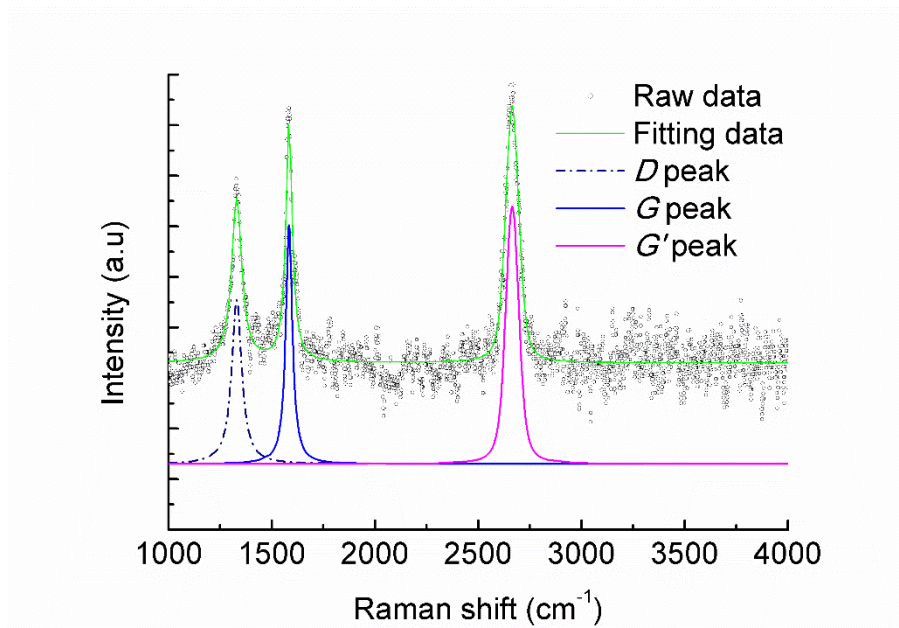


Figure 6.13 Raman spectrum of CNWs grown on surface layers of CNFs by using MPECVD (sample S-5).

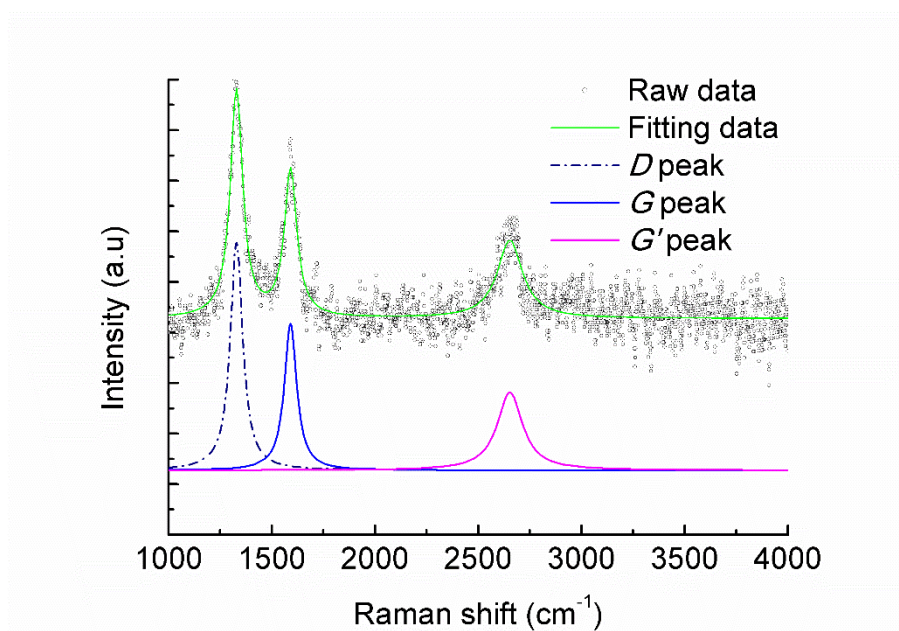


Figure 6.14 Raman spectrum of CNWs grown on deeper layers of CNFs by using MPECVD (sample S-6).

As explained in section 6.1, the plasma penetrated into the deeper layers of non-woven PAN NFs mat during the carbonization in the MPECVD chamber, given by the porous nature of the substrate material. This led to the formation of CNWs with different smaller dimension as shown in **Figure 6.6**. **Figure 6.14** shows the Raman spectrum of deeper layers of CNFs by using MPECVD (sample S-6). By comparing to the Raman spectrum of the grown CNWs on surface layers, no significant change in terms of peak positions was found in S-6. However, the R-value was increased significantly from 0.66 to 1.57, implying that the crystallinity of the material was decreased. The resulted L_a in sample S-6 was estimated to be 3.72 nm. On the other hand, the R-value is in fact smaller than the one obtained for sample S-4, which was also carbonized in MPECVD chamber with no grown CNWs was found. The change on the R-value in such fashion: S-4>S-6>S-5, confirms the “infiltration” process observed by SEM. Also demonstrated at given MPECVD processing conditions, the penetration depth is limited. Furthermore, the CNWs grown on the CNFs by MPECVD method is considered having high ordered structure. Even by growing a small amount of CNWs on the CNFs which had much lower crystallinity, the overall crystallinity of the hybrid materials was greatly improved.

Table 6.3 Assignment of main Raman peaks of PAN NFs treated with various treatments.
 ν_D , ν_G , $\nu_{G'}$ are the Raman peak position of *D* peak, *G* peak, and *G'* peak, respectively. I_D/I_G represents *R*-value, is the intensity ratio of *D* peak to *G* peak. L_a , graphitic crystallite size, is the ratio of 5.8 nm and the *R*-value.

Sample	ν_D (cm ⁻¹)	ν_G (cm ⁻¹)	$\nu_{G'}$ (cm ⁻¹)	I_D/I_G	L_a (nm)
S-1	-	-	-	-	-
S-2	1357 ± 7	1571 ± 5	-	2.40 ± 0.15	2.42 ± 0.16
S-3	1351 ± 8	1577 ± 2	2814 ± 25	1.29 ± 0.05	4.51 ± 0.19
S-4	1338 ± 1	1584 ± 7	2793 ± 2	1.70 ± 0.04	3.42 ± 0.09
S-5	1328 ± 3	1581 ± 2	2664 ± 4	0.66 ± 0.17	9.30 ± 2.88
S-6	1326 ± 3	1590 ± 3	2654 ± 5	1.57 ± 0.12	3.72 ± 0.29

6.4 Electrochemical Characterisations

The capacitive behaviour of both CNFs and CNWs-CNFs was characterised by using cyclic voltammetry (CV). The CV curves of CNFs and CNWs-CNFs in 0.5M H₂SO₄ solution at five various scan rate ranging from 5 to 100 mV are shown in **Figure 6.15** and **Figure 6.16**, respectively.

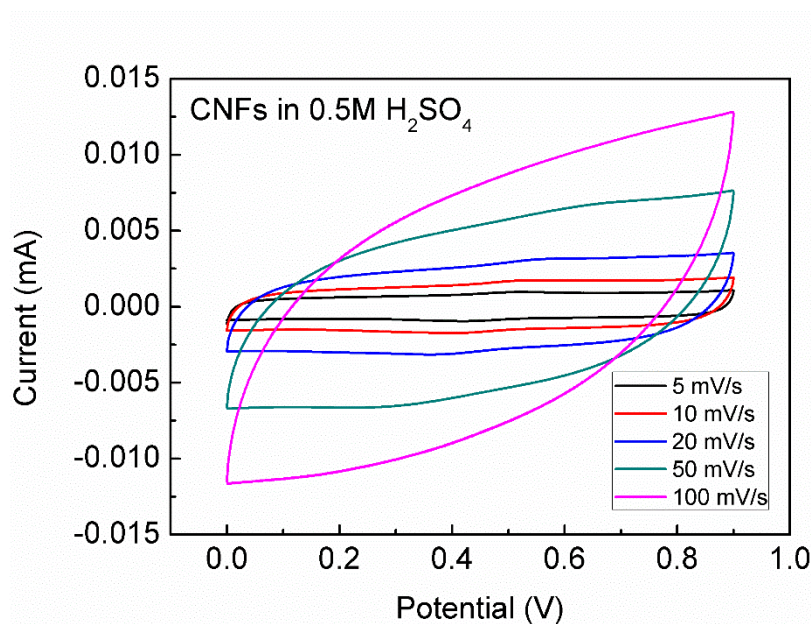


Figure 6.15 C-V curve of furnace fabricated CNFs in 0.5 M H₂SO₄ at different scan rates of 5, 10, 20, 50, and 100 mV at a voltage range from 0 to 0.9 V.

It is known that ideal capacitor electrode material exhibiting CV curve in a rectangular shape [132, 133]. The small deviation from the perfect rectangular shape associated with weak redox peaks around 0.5 V observed in **Figure 6.15** and **Figure 6.16**, indicating that both CNFs and CNWs-CNFs exhibited pseudo-capacitive behaviour in the testing environment. The presence of redox peaks due to oxidation/reduction reaction in carbon materials was previously attributed to the presence of functional groups [134]. As reported by Ra *et al.*, who discovered that the PAN NFs carbonized at 1000 °C still contained a fraction of oxygen and nitrogen contents [135]. It is known that the carbonization temperature used in the current investigation was lower than 1000 °C. In

this case, it is reasonable to think that the pseudo-capacitive behaviour observed in current two cases are functional groups also related. As there is no significant difference between the CV curve of CNFs and CNWs-CNFs at the scan rate in terms of size and shape. It is thus unlikely to be able to conclude the efficiency of the electrode performance solely based on the CV results.

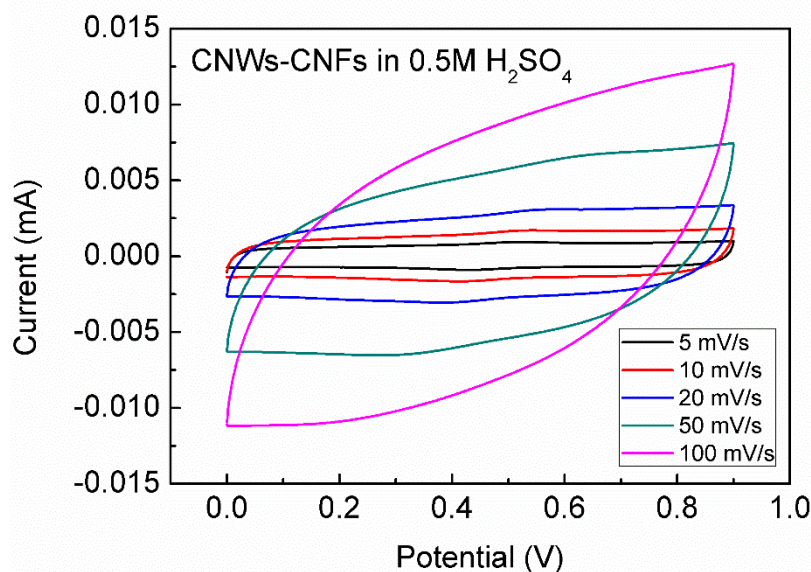


Figure 6.16 C-V curve of MPECVD fabricated CNFs in 0.5 M H₂SO₄ at different scan rates of 5, 10, 20, 50, and 100 mV at a voltage range from 0 to 0.9 V.

To determine the specific capacitance of both carbon materials, the charge-discharge experiment was carried out with current density of 0.4 A g⁻¹ in the voltage range of 0-9V. As indicated in **Figure 6.17**, the specific capacitance at current density of 0.4 A g⁻¹ of CNFs and CNWs-CNFs were measured to be approximately 200 and 250 F g⁻¹. This CNFs with CNWs exhibited higher specific capacitance with approximately of 50 F g⁻¹. It should be mentioned that the CNWs-CNFs that was investigated by electrochemical characterisation was not optimized. The optimization of CNWs-CNFs hybrid materials by MPECVD towards to the electrochemical performance will be carried out in the future work.

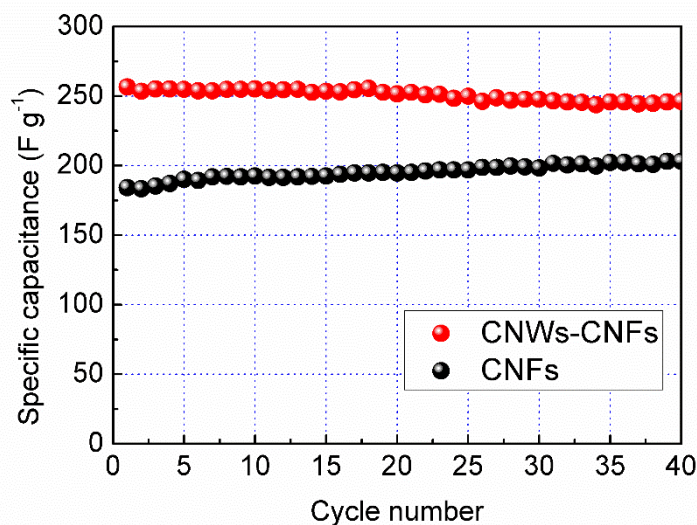


Figure 6.17 Cycle life of CNFs and CNWs-CNFs in the voltage range from 0 to 0.9V.

6.5 Summary

In summary, MPECVD can be applied as an alternative method to carbonized PAN NFs in order to fabricate CNFs. SEM, FTIR, Raman, CV and charge-discharge measurements were employed to study the PAN NFs at different stages of evolution. It was found that the furnace carbonized PAN NFs exhibited larger diameter shrinkage compared with the MPECVD-carbonized PAN NFs. The fibre diameter discrepancy was attributed to the temperature, the chemical and physical nature of two different methods. FTIR spectra indicate that the furnace carbonized PAN NFs show few functional groups, whereas weak broad bands refer to C-H vibrations and a mix of C=N, C=C, N-H were noticed in MPECVD-carbonized PAN NFs. An additional coating of CNWs was formed on the surface layers of MPECVD-carbonized PAN NFs without the application of metallic catalyst. In addition, it was noticed that dimension of the grown CNWs were varied with the depth of the sample. The Raman spectra of CNWs-CNFs were discussed in details. Electrochemical characterisation indicated that CNWs-CNFs possessed higher specific capacitance in comparison to the furnace carbonized PAN NFs. The work presented here developed a novel, economical and straightforward approach towards mass production of carbon

fibrous materials containing CNWs, which potentially can be applied in the supercapacitor applications. Similar work has been published in reference [104].

7 Conclusions and Future Work

7.1 Conclusions

Three main topics of the project were discussed in the thesis, they were electrospinning of PAN NFs, fabrication and characterisation of CNFs, and fabrication and characterisation of CNWs-CNFs hybrid materials.

In the first main topic, the detailed investigation of four parameters, including voltage, TCD, Q and C were studied. It was found that with fixed C of PAN solution at 12 wt%, the optimized processing parameters were established to be 16 kV, 14 cm, and 1.5 mL/h. At given condition, the resulted fibres were bead free with fibre diameter ranging from approximately 236 to 255 nm, which were obtained from five individual experiment and carried out in the different days with different deposition duration. The good reproducibility and long stability of the optimized processing parameters were confirmed by the small fibre diameter variation. In the process of searching optimized processing parameters, no regular pattern was found between fibre diameter with voltage, or with Q . While with different TCD, it was found that at TCD of 5 cm while voltage and Q were maintained at 16 kV and 1.5 mL/h, the fused and beaded fibres were formed. With increasing TCD to 30 cm, the resulted fibre with relatively good uniformity. The diameter was generally decreased while fraction of deposition area per SEM image was also decreased. These changes were attributed to the longer stretching distance and weaker attractive electrostatic force, respectively. On the other hand, it seemed that the voltage and Q have very direct impact on the formation of beads within the electrospun fibres. By increasing voltage with magnitude larger than 16 kV while maintained voltage of 15 cm and 1.5 mL/h constant, only beaded fibre formed. It is also found that minimum Q was required in order to generate smooth fibres, and this minimum value was varied with other parameter. For instance, the minimum Q with TCD of 14 cm (1.5 mL/h) was smaller than the one with 10 cm (2.5 mL/h). The formation of beads observed

in the current investigation can be generally attributed to the mass imbalance between the solution consumption from solution drop at the needle tip in order for the ejected jet to collector and delivered solution from the polymer solution supply from the syringe pump. To avoid the formation of the beads if only processing parameter was tuned, the consistency between the rates of these two processes need to maintain. It was witnessed that the electrospray was shifted to electrospinning with increasing C from 2 to 16 wt%, while the processing parameters were fixed on the optimized values. The break up of the fluid jet at low C region from 2 to 6% with the formation of beads only was attributed to the poor polymer chain entanglement. By increasing C to 16 wt%, either beaded fibres or smooth fibres with increasing diameters were observed. The morphological transition indicated that the strong viscoelastic force generated by the enhanced polymer chain entanglement to resist the fibre jet breakage. In the investigation of C , smallest bead-free fibres was approximately 248 nm obtained at 12 wt% PAN concentration whereas 16 wt% PAN concentration led to the thickest diameter with diameter of approximately 480 nm. However, the solution quickly dried out at the needle tip for solution concentration at 16 wt% was observed.

In the second main topic, the fabrication of CNFs by using the electrospun PAN fibres with various carbonization temperatures, ranging from 500 to 1000 °C was conducted by using conventional tubular furnace. It was found that by increasing carbonization temperature, SEM revealed that fibre diameter was decreased progressively from 260 to 187 nm, while the graphitic crystallite size was increased from 2.62 to 5.24 nm indicated by Raman. In addition, the functional groups were also progressively disappeared on the FTIR spectra. Furthermore, evolution of extracted electrical circuit from impedance results for CNF_s with increasing carbonization temperature, which was correlated to the proposed microstructural evolution. The findings of this work has demonstrated the possibility for impedance spectroscopy to be applied as a non-destructive technique to monitor the carbonization degree of CNF_s during the industrial manufacturing process [112].

The work involved in the third main topic of the project was to develop a novel, economical, and straightforward approach to mass production of CNWs-CNFs hybrid materials. The direct growth of CNWs while the carbonization of PAN NFs with da of 431 ± 67 nm by MPECVD using 800W, 40 Torr in the CH₄/H₂ (10:90) plasma for 30 min led to the formation of CNWs-CNFs hybrid materials. It was noticed that the size of the grown CNWs on surfaces of PAN derived CNFs was decreased with increasing depth towards to the bottom of the hybrid material. The size change of the grown CNWs on the CNFs was attributed to the plasma penetration depth into the non-woven PAN NFs mat. The thickness of the CNWs was estimated to be 6-10 nm. By consulting literature, the thickness of the CNWs was consisted of 13-30 graphene layers. The method for the fabrication of CNWs-CNFs developed in this project associated with less fabrication procedures compared with published literature. In addition, by comparing the conventional furnace produced CNFs with CNWs-CNFs fabricated by using MPECVD, the later sample exhibited better supercapacitor property by showing higher specific capacitance in the charge-discharge measurement.

7.2 Future Work

There will be three directions can be further pursued as the continuation of the current project. As inspired by the one of the publications regarding to the using femtosecond laser on single crystalline diamond [136], the fabrication of micropatterns from PAN derived CNFs can be pursued to fabricate carbon MEMS devices, as an extension of first two topics of the project. The second direction can use MPECVD technique to fabricate CNFs hybrid material with other carbon species, such as diamond, CNTs, and etc. In addition, to explore the application of newly developed carbon hybrid materials in wide variety of applications, particularly, in biomedical applications. The third direction is to investigate the supercapacitor performance of various carbon nanomaterials. The correlation between the fabrication parameters and the properties will be subsequently studied.

8 Reference

- [1] A. Formalas, US, 1934.
- [2] H.R. Darrell, C. Iksoo, *Nanotechnology*, 7 (1996) 216.
- [3] A. Frenot, I.S. Chronakis, *Current Opinion in Colloid & Interface Science*, 8 (2003) 64-75.
- [4] Z.M. Huang, Y.Z. Zhang, M. Kotaki, S. Ramakrishna, *Composites Science and Technology*, 63 (2003) 2223-2253.
- [5] A. Greiner, J.H. Wendorff, *Angewandte Chemie International Edition*, 46 (2007) 5670-5703.
- [6] S. Ramakrishna, *An introduction to electrospinning and nanofibers*, World Scientific Publishing Company Incorporated, 2005.
- [7] S. Ramakrishna, K. Fujihara, W.-E. Teo, T.-C. Lim, Z. Ma, *Potential Applications, An Introduction to Electrospinning and Nanofibers*, 2005, pp. 275-340.
- [8] G. Taylor, *Electrically Driven Jets*, 1969.
- [9] A.L. Yarin, S. Koombhongse, D.H. Reneker, *Journal of Applied Physics*, 90 (2001) 4836-4846.
- [10] L. Larrondo, R. St. John Manley, *Journal of Polymer Science: Polymer Physics Edition*, 19 (1981) 909-920.
- [11] L. Larrondo, R. St. John Manley, *Journal of Polymer Science: Polymer Physics Edition*, 19 (1981) 921-932.
- [12] L. Larrondo, R. St. John Manley, *Journal of Polymer Science: Polymer Physics Edition*, 19 (1981) 933-940.
- [13] D. Li, Y. Xia, *Advanced Materials*, 16 (2004) 1151-1170.
- [14] D.H. Reneker, A.L. Yarin, *Polymer*, 49 (2008) 2387-2425.
- [15] K. Garg, G.L. Bowlin, *Biomicrofluidics*, 5 (2011) 013403.
- [16] Y.M. Shin, M.M. Hohman, M.P. Brenner, G.C. Rutledge, *Polymer*, 42 (2001) 09955-09967.
- [17] D.H. Reneker, H. Fong, *American Chemical Society Meeting, American Chemical Society, Washington, DC 2006*.
- [18] H. Fong, I. Chun, D.H. Reneker, *Polymer*, 40 (1999) 4585-4592.
- [19] C. Wang, Y.W. Cheng, C.H. Hsu, H.S. Chien, S.Y. Tsou, *J Polym Res*, 18 (2011) 111-123.
- [20] N. Bhardwaj, S.C. Kundu, *Biotechnology Advances*, 28 (2010) 325-347.
- [21] Q.P. Pham, U. Sharma, A.G. Mikos, *Tissue engineering*, 12 (2006) 1197-1211.
- [22] V. Pillay, C. Dott, Y.E. Choonara, C. Tyagi, L. Tomar, P. Kumar, L.C. du Toit, V.M.K. Ndesendo, *Journal of Nanomaterials*, 2013 (2013) 22.
- [23] R. Jalili, S.A. Hosseini, M. Morshed, *Iranian Polymer Journal*, 14 (2005) 1074-1081.
- [24] M.M. Demir, I. Yilgor, E. Yilgor, B. Erman, *Polymer*, 43 (2002) 3303-3309.
- [25] K.H. Lee, H.Y. Kim, H.J. Bang, Y.H. Jung, S.G. Lee, *Polymer*, 44 (2003) 4029-4034.
- [26] W. Liu, S. Adanur, *Textile Research Journal*, 80 (2010) 124-134.
- [27] P.K. Baumgarten, *Journal of Colloid and Interface Science*, 36 (1971) 71-79.
- [28] T. Subbiah, G. Bhat, R. Tock, S. Parameswaran, S. Ramkumar, *Journal of Applied Polymer Science*, 96 (2005) 557-569.
- [29] J.M. Deitzel, J. Kleinmeyer, D. Harris, N.C. Beck Tan, *Polymer*, 42 (2001) 261-272.

- [30] J. Fang, H. Wang, H. Niu, T. Lin, X. Wang, *Journal of Applied Polymer Science*, 118 (2010) 2553-2561.
- [31] T. Wang, S. Kumar, *Journal of Applied Polymer Science*, 102 (2006) 1023-1029.
- [32] K.D. Behler, A. Stravato, V. Mochalin, G. Korneva, G. Yushin, Y. Gogotsi, *ACS Nano*, 3 (2009) 363-369.
- [33] F. Ko, Y. Gogotsi, A. Ali, N. Naguib, H. Ye, G.L. Yang, C. Li, P. Willis, *Advanced Materials*, 15 (2003) 1161-1165.
- [34] C.S. Sharma, R. Vasita, D.K. Upadhyay, A. Sharma, D.S. Katti, R. Venkataraghavan, *Industrial & Engineering Chemistry Research*, 49 (2010) 2731-2739.
- [35] J.H. He, Y.Q. Wan, J.Y. Yu, *Fibers Polym*, 9 (2008) 140-142.
- [36] M. Bognitzki, W. Czado, T. Frese, A. Schaper, M. Hellwig, M. Steinhart, A. Greiner, J.H. Wendorff, *Advanced Materials*, 13 (2001) 70-72.
- [37] C.L. Casper, J.S. Stephens, N.G. Tassi, D.B. Chase, J.F. Rabolt, *Macromolecules*, 37 (2003) 573-578.
- [38] C. Wang, H.S. Chien, C.H. Hsu, Y.C. Wang, C.T. Wang, H.A. Lu, *Macromolecules*, 40 (2007) 7973-7983.
- [39] N. Kizildag, Y. Beceren, M. Kazanci, D. Cukul.
- [40] R. Khajavi, M. Abbasipour, *Scientia Iranica*, 19 (2012) 2029-2034.
- [41] A. Saraf, G. Lozier, A. Haesslein, F.K. Kasper, R.M. Raphael, L.S. Baggett, A.G. Mikos, *Tissue Engineering. Part C, Methods*, 15 (2009) 333-344.
- [42] H. Liu, Y.L. Hsieh, *Journal of Polymer Science Part B: Polymer Physics*, 40 (2002) 2119-2129.
- [43] W.E. Teo, S. Ramakrishna, *Nanotechnology*, 17 (2006) R89.
- [44] H. Yuan, S. Zhao, H. Tu, B. Li, Q. Li, B. Feng, H. Peng, Y. Zhang, *Journal of Materials Chemistry*, 22 (2012) 19634-19638.
- [45] A. Theron, E. Zussman, A.L. Yarin, *Nanotechnology*, 12 (2001) 384.
- [46] D. Li, Y. Wang, Y. Xia, *Nano Letters*, 3 (2003) 1167-1171.
- [47] D. Li, Y. Xia, *Nano Letters*, 4 (2004) 933-938.
- [48] T.A. Edison, U.S., 1880.
- [49] H.O. Pierson, 8 - Carbon Fibers, in: H.O. Pierson (Ed.) *Handbook of Carbon, Graphite, Diamonds and Fullerenes*, William Andrew Publishing, Oxford, 1993, pp. 166-197.
- [50] J.B. Donnet, *Carbon fibers*, Thrid Edition Revised and Expanded ed., 1998.
- [51] Edison Innovation Foundation, 2014.
- [52] X. Huang, *Materials*, 2 (2009) 2369-2403.
- [53] M. Inagaki, Y. Yang, F. Kang, *Advanced Materials*, 24 (2012) 2547-2566.
- [54] S. Chand, *J Mater Sci*, 35 (2000) 1303-1313.
- [55] M.S.A. Rahaman, A.F. Ismail, A. Mustafa, *Polymer Degradation & Stability*, 92 (2007) 1421-1432.
- [56] L. Zhang, A. Aboagye, A. Kelkar, C. Lai, H. Fong, *J Mater Sci*, 49 (2014) 463-480.
- [57] R. Prescott, I.W. Orr, *Google Patents*, 1970.
- [58] T.-H. Ko, *Journal of Applied Polymer Science*, 43 (1991) 589-600.
- [59] Z. Bashir, *Carbon*, 29 (1991) 1081-1090.
- [60] E. Fitzer, M. Heine, *Compos. Mater. Ser.*, (1988) 73-148.

- [61] E. Fitzer, D.J. Müller, *Carbon*, 13 (1975) 63-69.
- [62] P. Rangarajan, V.A. Bhanu, D. Godshall, G.L. Wilkes, J.E. McGrath, D.G. Baird, *Polymer*, 43 (2002) 2699-2709.
- [63] R.C. Houtz, *Textile Research Journal*, 20 (1950) 786-801.
- [64] L.H. Peebles Jr, P. Peyser, A.W. Snow, W.C. Peters, *Carbon*, 28 (1990) 707-715.
- [65] N. Grassie, R. McGuchan, *European Polymer Journal*, 7 (1971) 1357-1371.
- [66] P. Goodhew, A. Clarke, J. Bailey, *Materials Science and Engineering*, 17 (1975) 3-30.
- [67] R. Perret, W. Ruland, *Journal of Applied Crystallography*, 3 (1970) 525-532.
- [68] M. Endo, *Chemtech*, 18 (1988) 568-576.
- [69] Y. Kim, T. Hayashi, M. Endo, M. Dresselhaus, *Carbon Nanofibers*, in: R. Vajtai (Ed.) *Springer Handbook of Nanomaterials*, Springer Berlin Heidelberg, 2013, pp. 233-262.
- [70] N.M. Rodriguez, M.-S. Kim, R.T.K. Baker, *The journal of physical chemistry*, 98 (1994) 13108-13111.
- [71] J. Rafique, J. Yu, X. Zha, K. Rafique, *Bull Mater Sci*, 33 (2010) 553-559.
- [72] M. Endo, Y.A. Kim, T. Hayashi, K. Nishimura, T. Matusita, K. Miyashita, M.S. Dresselhaus, *Carbon*, 39 (2001) 1287-1297.
- [73] S.N. Arshad, M. Naraghi, I. Chasiotis, *Carbon*, 49 (2011) 1710-1719.
- [74] Z. Zhou, C. Lai, L. Zhang, Y. Qian, H. Hou, D.H. Reneker, H. Fong, *Polymer*, 50 (2009) 2999-3006.
- [75] E. Fitzer, W. Frohs, M. Heine, *Carbon*, 24 (1986) 387-395.
- [76] A.D. Maop Panapy, Bussarin Ksapabutr, *Thammasat Int. J.Sc.Tech.*, 13 (2008).
- [77] J.B. Donnet, O.P. Bahl, *Encyclopedia of physical science and technology*, Acedamic Press Inc, New York, 1987.
- [78] T.-H. Ko, *Journal of Applied Polymer Science*, 42 (1991) 1949-1957.
- [79] T.H. Ko, H.Y. Ting, C.H. Lin, *Journal of Applied Polymer Science*, 35 (1988) 631-640.
- [80] D. Riggs, R. Shuford, R. Lewis, *Graphite Fibers and Composites*, in: G. Lubin (Ed.) *Handbook of Composites*, Springer US, 1982, pp. 196-271.
- [81] N. Melanitis, P.L. Tetlow, C. Galiotis, *J Mater Sci*, 31 (1996) 851-860.
- [82] J. Wang, M. Zhu, R.A. Outlaw, X. Zhao, D.M. Manos, B.C. Holloway, *Carbon*, 42 (2004) 2867-2872.
- [83] S. Vizireanu, B. Mitu, C.R. Luculescu, L.C. Nistor, G. Dinescu, *Surface and Coatings Technology*, 211 (2012) 2-8.
- [84] S. Vizireanu, L. Nistor, M. Haupt, V. Katzenmaier, C. Oehr, G. Dinescu, *Plasma Processes and Polymers*, 5 (2008) 263-268.
- [85] D.S. Knight, W.B. White, *Journal of Materials Research*, 4 (1989) 385-393.
- [86] Y. Wang, S. Serrano, J.J. Santiago-Avilés, *Synthetic Metals*, 138 (2003) 423-427.
- [87] H. Niu, J. Zhang, Z. Xie, X. Wang, T. Lin, *Carbon*, 49 (2011) 2380-2388.
- [88] E. Fitzer, *Carbon*, 27 (1989) 621-645.
- [89] H. Hou, D.H. Reneker, *Advanced Materials*, 16 (2004) 69-73.
- [90] L. Zhao, Y. Li, Y. Zhao, Y. Feng, W. Feng, X. Yuan, *Appl. Phys. A*, 106 (2012) 863-869.
- [91] N. Lisi, R. Giorgi, M. Re, T. Dikonimos, L. Giorgi, E. Salernitano, S. Gagliardi, F. Tatti, *Carbon*, 49 (2011) 2134-2140.

- [92] H.C. Hsu, C.H. Wang, S.K. Nataraj, H.C. Huang, H.Y. Du, S.T. Chang, L.C. Chen, K.H. Chen, *Diamond and Related Materials*, 25 (2012) 176-179.
- [93] J. Ting, M.L. Lake, *Journal of Materials Research*, 9 (1994) 636-642.
- [94] M. Wu, Q. Wang, X. Liu, H. Liu, *Carbon*, 51 (2013) 335-345.
- [95] S. Su, J. Li, V. Kunderát, A.M. Abbot, H. Ye, *Diamond and Related Materials*, 24 (2012) 49-53.
- [96] S. Shi, J. Li, K. Vojtěch, M.A. Andrew, Y. Haitao, *Journal of Applied Physics*, 113 (2013) 023707.
- [97] H. Ye, P. Hing, *International Journal of Thermophysics*, 22 (2001) 1285-1294.
- [98] Y.J. Wang, Y. Pan, X.W. Zhang, K. Tan, *Journal of Applied Polymer Science*, 98 (2005) 1344-1350.
- [99] http://sekidiamond.com/pdf/AX5010-INT_Brochure_R1.pdf
- [100] P.J. Goodhew, J. Humphreys, R. Beanland, *Electron microscopy and analysis*, Third ed., Taylor & Francis, 2001.
- [101] K.L. Elias, R.L. Price, T.J. Webster, *Biomaterials*, 23 (2002) 3279-3287.
- [102] C. Zhang, X. Yuan, L. Wu, Y. Han, J. Sheng, *European Polymer Journal*, 41 (2005) 423-432.
- [103] Y. Wang, J. Liu, J. Y. Liang, *Advanced Materials Research*, 11-12 (2006) 73-76.
- [104] J. Li, S. Su, L. Zhou, V. Kunderat, A.M. Abbot, F. Mushtaq, D. Ouyang, D. James, D. Roberts, H. Ye, *Journal of Applied Physics*, 113 (2013) 024313.
- [105] H. Kakida, K. Tashiro, *Polymer Journal*, 29 (1997) 557-562.
- [106] W.X. Zhang, Y.Z. Wang, C.F. Sun, *J Polym Res*, 14 (2007) 467-474.
- [107] S. Su, J. Li, V. Kunderat, A.M. Abbot, H. Ye, *J. Appl. Phys.*, 113 (2013) 023707-023708.
- [108] H. Ye, C. Sun, H. Huang, P. Hing, *Appl. Phys. Lett.*, 78 (2001) 1826-1828.
- [109] N. Hedin, V. Sobolev, L. Zhang, Z. Zhu, H. Fong, *J Mater Sci*, 46 (2011) 6453-6456.
- [110] R.J. Diefendorf, E. Tokarsky, *Polymer Engineering & Science*, 15 (1975) 150-159.
- [111] Y. Wang, J.J.S. Aviles, R. Furlan, I. Ramos, *IEEE Trans. Nanotechnol.*, 2 (2003) 39-43.
- [112] J. Li, S. Shi, Z. Lei, M.A. Andrew, Y. Haitao, *Materials Research Express*, 1 (2014) 035604.
- [113] M.S.A. Rahaman, A.F. Ismail, A. Mustafa, *Polym. Degrad. Stabil.*, 92 (2007) 1421.
- [114] W. Zhang, Y. Wang, C. Sun, *J. Polym. Res.*, 14 (2007) 467.
- [115] W.J. Burlant, J.L. Parsons, *Journal of Polymer Science*, 22 (1956) 249-256.
- [116] L. Giorgi, T.D. Makris, R. Giorgi, N. Lisi, E. Salernitano, *Sensors and Actuators B: Chemical*, 126 (2007) 144-152.
- [117] A. Malesevic, S. Vizireanu, R. Kemps, A. Vanhulsel, C.V. Haesendonck, G. Dinescu, *Carbon*, 45 (2007) 2932-2937.
- [118] Y. Wu, P. Qiao, T. Chong, Z. Shen, *Advanced Materials*, 14 (2002) 64-67.
- [119] M. Hiramatsu, K. Shiji, H. Amano, M. Hori, *Applied Physics Letters*, 84 (2004) 4708-4710.
- [120] M. Zhu, J. Wang, B.C. Holloway, R.A. Outlaw, X. Zhao, K. Hou, V. Shutthanandan, D.M. Manos, *Carbon*, 45 (2007) 2229-2234.
- [121] J.J. Wang, M.Y. Zhu, R.A. Outlaw, X. Zhao, D.M. Manos, B.C. Holloway, V.P. Mammana, *Appl. Phys. Lett.*, 85 (2004) 1265.
- [122] S. Kurita, A. Yoshimura, H. Kawamoto, T. Uchida, K. Kojima, M. Tachibana, P. Molina Morales, H. Nakai, *Journal of Applied Physics*, 97 (2005).

- [123] S. Dalton, F. Heatley, P.M. Budd, *Polymer*, 40 (1999) 5531.
- [124] J. Rafique, J. Yu, X. Zha, K. Rafique, *Bull. Mater. Sci.*, 33 (2010) 553.
- [125] Y. Wang, J. Liu, J.Y. Liang, *Adv. Mater. Res.*, 11-12 (2006) 73.
- [126] H. Kakida, K. Tashiro, *Polym. J.*, 29 (1997) 557.
- [127] J. Sutasinpromprae, S. Jitjaicham, M. Nithitanakul, C. Meechaisue, P. Supaphol, *Polymer International*, 55 (2006) 825-833.
- [128] M. Panapoy, A. Dankeaw, B. Ksapabutr, *Thammasat Int. J. Sc. Tech.*, 13 (2008) 11.
- [129] C. Kim, S.H. Park, J.I. Cho, D.Y. Lee, T.J. Park, W.J. Lee, K.S. Yang, *J. Raman. Spectrosc.*, 35 (2004) 928.
- [130] G. Zou, D. Zhang, C. Dong, H. Li, K. Xiong, L. Fei, Y. Qian, *Carbon*, 44 (2006) 828-832.
- [131] J. Kastner, T. Pichler, H. Kuzmany, S. Curran, W. Blau, D.N. Weldon, M. Delamesiere, S. Draper, H. Zandbergen, *Chemical Physics Letters*, 221 (1994) 53-58.
- [132] J.S. Ye, X. Liu, H.F. Cui, W.D. Zhang, F.S. Sheu, T.M. Lim, *Electrochemistry Communications*, 7 (2005) 249-255.
- [133] E. Frackowiak, F. Béguin, *Carbon*, 39 (2001) 937-950.
- [134] E.C. Almeida, M.R. Baldan, J.M. Rosolen, N.G. Ferreira, *Diamond and Related Materials*, 17 (2008) 1529-1533.
- [135] E.J. Ra, E. Raymundo Piñero, Y.H. Lee, F. Béguin, *Carbon*, 47 (2009) 2984-2992.
- [136] G.C.B. Lee, S. Su, J. Li, K. Sugden, N. Roohpour, H. Yan, H. Ye, *Journal of Experimental Nanoscience*, 7 (2012) 662-672.